STRESS CORROSION CRACKING AND HYDROGEN EMBRITTLEMENT OF THICK SECTION HIGH STRENGTH LOW ALLOY STEEL

by

WILLIAM DONALD NEEDHAM

B.S. Mech. Eng., Duke University (1972)
M.A. Central Michigan University (1983)

SUBMITTED TO THE DEPARTMENT OF
OCEAN ENGINEERING
IN PARTIAL FULFILLMENT OF THE REQUIREMENTS
FOR THE DEGREES OF

OCEAN ENGINEER

and

MASTER OF SCIENCE IN MATERIALS SCIENCE AND ENGINEERING

at the

MASSACHUSETTS INSTITUTE OF TECHNOLOGY
June, 1986

Signature of Author............ ......
Department of Ocean Engineering
May, 1986

Certified by............ ....
Assistant Professor Ronald G. Ballinger
Thesis Supervisor

Certified by.............. ....
Professor Koichi Masubuchi
Thesis Reader

Accepted by..
Professor A. Douglas Carmichael, Chairman
Departmental Graduate Committee
Department of Ocean Engineering

Accepted by.................. ....
Professor Bernhardt J. Wuensch, Chairman
Departmental Committee on Graduate Students
Department of Materials Science and Engineering

STRESS CORROSION CRACKING AND HYDROGEN EMBRITTLEMENT OF THICK SECTION HIGH STRENGTH LOW ALLOY STEEL

by

WILLIAM DONALD NEEDHAM

Submitted to the Department of Ocean Engineering
on May 7, 1986 in partial fulfillment of the
requirements for Degrees of Ocean Engineer and
Master of Science in Materials Science and Engineering

ABSTRACT

An experimental study was conducted to evaluate the corrosion performance of weldments of a high strength low alloy (HSLA) steel in a simulated seawater environment. This steel, designated HSLA 80, was developed by the United States Navy for use in ship structural applications. Stress corrosion cracking (SCC) and hydrogen embrittlement (HEM) were investigated by conducting 42 Wedge-Opening Load (WOL) tests as a function of stress intensity and corrosion potential and 33 Slow Strain Rate (SSR) tests as a function of strain rate and corrosion potential. The corrosion potentials were chosen to simulate the environmental conditions of free corrosion, cathodic protection and hydrogen generation.

The results from this investigation indicated that HSLA 80 base metal and weldments were susceptible to hydrogen assisted cracking (HAC) in a seawater environment under conditions of continuous plastic deformation and triaxial stress in the presence of hydrogen. The heat-affected zone of the weldment was found to be the most susceptible portion of the weld joint. A lower bound was established for the critical stress intensity for stress corrosion cracking for HSLA 80 base metal and weldments.

Thesis Supervisor: Dr. Ronald George Ballinger

Title: Assistant Professor of Materials Science
and Engineering

ACKNOWLEDGEMENTS

Professor Ballinger has provided invaluable guidance and assistance in the inception and execution of this thesis. His personal involvement in the identification of funding for a meaningful research project resulted not only in the completion of this research but laid the groundwork for future thesis efforts by other naval officers. His encouragement, foresight and direction were instrumental in completing all research objectives.

John Gudas, Paul Holsberg and Joe Blackburn of the David Taylor Naval Ship Research and Development Center at Annapolis, Maryland deserve special credit for providing funds for this thesis and for their assistance in material procurement and weld fabrication. These outstanding engineers have both my respect and gratitude, for without them this thesis could never have been accomplished.

John Prybylowski, Glenn Romanoski, Pete Searson and Il-Soon Huang deserve my special thanks as friends, consultants and assistants. Their interest and enthusiasm in helping to find solutions to difficult experimental problems were the key to the success of this thesis. I am humbled by their intellectual capacity, practical good sense and engineering know-how.

Finally, I would like to express my gratitude to the United States Navy for allowing me to further my education at MIT. I pledge to repay that debt of gratitude in the coming years to the best of my ability.

The author acknowledges the right of the United States Government and its agencies to reproduce and to distribute copies of this thesis document in whole or in part.

TABLE OF CONTENTS

LIST OF FIGURES

LIST OF TABLES

PAGE

1.0 INTRODUCTION:

Stress corrosion cracking (SCC) is an extremely complex phenomenon since it involves not only environmental and metallurgical factors acting in synergism but interfacial and continuum considerations as well. In that any one individual may at best be considered a specialist in only one of these fields, it is not surprising that there is no reliable fundamental theory that applies to any and all alloy/environment systems [1]. In fact, it is becoming increasingly apparent that there is no one single mechanism that is responsible for cracking but that a variety of processes are operative for a specific alloy/environment system.

In spite of its intractability, stress corrosion cracking is of crucial importance to materials engineering. The unassailable facts that a few parts per million (ppm) of chloride can result in cracking of stainless steel, that a few ppm of ammonia can crack brass and that high strength steels are embrittled by hydrogen must be recognized in any material design specification. The crux of the theoretical issue is that no cause and effect relationship can be established between a given material and a given environment based on the behavior of a different system. In other words, theory cannot predict stress corrosion cracking susceptibility. The only acceptable and reliable measure must then be to test the proposed system macroscopically and extrapolate to the microscopic level of crack behavior.

The specific test procedure to be followed in evaluating SCC susceptibility is in and of itself a thorny issue. Generally, the full component cannot be selected as the test specimen due to size and economic constraints. Clearly, in assessing a material for possible ship applications, one cannot build ships to test in various environments. Although numerous specimen geometries have been proposed and used, they may generally be separated into three fundamental groups [2]:

(1) Smooth specimens under static load.

(2) Precracked specimens under static and dynamic load.

(3) Smooth specimens under dynamic load with a constant strain rate.

Smooth specimen testing (both static and dynamic) results in the measurement of an index such as time to failure or reduction of area which may then be compared to baseline data when the same specimen is tested in a control or inert environment. Fractographic analysis may additionally be employed to assess the nature of the failure. Precracked specimen testing differs in that the response of a material in the presence of a sharp crack must be treated using fracture mechanics techniques so as to characterize the stress concentration inherent to the notch geometry. The index of material susceptibility in the precracked case is the threshold stress intensity factor K_{ISCC} below which the crack will not grow.

Service environments can be determinant or indeterminant depending on the products intended end use. Unfortunately, most actual engineering applications are either air or water which, though perceived as locally homogeneous are in actuality globally diverse. A recent series of experiments [3] intended to evaluate the susceptibility of HY 130 to SCC employed flowing natural seawater, constant temperature seawater, transported seawater, synthetic seawater, brine, brackish water and polluted harbor water. The choice of environment is thus one of some complexity with an implied tradeoff of severity for reproducibility. (It should be noted that in the particular experimental program cited it was concluded that the modified seawater test environments were in fact no more severe than actual seawater).

The evaluation of a given alloy/environment system for susceptibility to stress corrosion cracking is thus fraught with experimental uncertainty, a panoply of theoretical postulations and a lack of clarity in the interpretation and reporting of historical results. This research study will evaluate the stress corrosion cracking and hydrogen embrittlement behavior of a relatively new steel adopted for use by the U. S. Navy for hull structural applications. This steel is a member of the High Strength Low Alloy (HSLA) Group which has high ductility due to low carbon levels and a relatively high yield strength (80 ksi) derived primarily from copper precipitation. In that it is intended as a replacement for the currently used HY 80 steel, it has been designated

HSLA 80. The focus of this thesis is to determine whether or not HSLA 80 is susceptible to stress corrosion cracking or hydrogen embrittlement.

2. BACKGROUND:

2.1 SUSTAINED LOAD ENVIRONMENT CRACKING:

Continuing fundamental research in the field of Materials Engineering has led to the identification and codification of at least nineteen processes which can reduce the life expectancy of a metallic structure or component. These processes may be broken down into three subgroups as follows [2]:

A. Mechanical
    (1) Yielding
    (2) Brittle fracture
    (3) Overload or ductile fracture
    (4) High temperature creep
    (5) Fatigue
    (6) Wear

B. Chemical
    (1) Uniform or general corrosion
    (2) Crevice corrosion
    (3) Pitting
    (4) Galvanic or dissimilar metal corrosion
    (5) Intergranular corrosion
    (6) Selective dissolution (e.g. dezincification)
    (7) Filiform corrosion
    (8) High temperature oxidation

C. Chemical and Mechanical (Mixed Effects)
    (1) Corrosion fatigue
    (2) Erosion corrosion
    (3) Hydrogen cracking or embrittlement
    (4) Liquid metal assisted cracking
    (5) Stress corrosion cracking

Material development programs must consider most if not all of the above potential failure modes depending on the specific end use application. In critical design applications, such as naval ship construction, all material failure modes must be rigorously analyzed and certified before the first plate is bent. HSLA 80 was developed from the International Nickel Company's linepipe steel manufactured to the ASTM specification A710. The original steel product was formulated to maintain its toughness at the extremely low temperatures of arctic pipeline applications. The U. S. Navy embarked on a program [4] to certify HSLA 80 for surface ship applications in 1981 as a replacement for HY 80 due to the expense in both production and fabrication of the latter. This experimental program was limited to relatively thin plate (less than 1 1/4 inches) due to the intended end use application. Further applications require the evaluation of thick section plate (2 inches) in a separate development program of which this research study is a part.

Of the identified failure modes, some (such as yielding) are readily evaluated by time-honored methods standardized under the aegis of the ASTM. Others are somewhat less readily quantified, particularly those in the third subgroup which result from "mixed" effects. Within this subgroup, one may further identify three processes that share a number of common features. These three processes; hydrogen embrittlement (HEM), liquid metal assisted cracking (LMAC) and stress corrosion cracking (SCC) have been called "sustained load environmental cracking" [2] (to distinguish them from the cyclic loading corrosion fatigue and the no load erosion corrosion). In that this study is directed to HSLA steel evaluation for ship applications, the LMAC failure mechanism shall hereafter be excluded from consideration.

Hydrogen embrittlement and stress corrosion cracking are remarkably similar insofar as their effects and requirements are concerned [5,2]:

(1) Both produce macroscopically brittle fracture even in metals that exhibit ductile failure in a tension test.

(2) There is a general increased susceptibility to failure for both processes as the yield strength of an alloy is increased.

(3) Cracks propagate discontinuously in both processes.

(4) Both require a tensile stress.

(5) Both processes can occur at stresses far below that required for general yielding but will often not occur below a threshold stress.

(6) Both processes are believed to involve localized plastic flow.

(7) Both processes have similar grain size dependencies, similar response to other metallurgical variables, and similar strain rate and temperature dependencies.

(8) Specificity of the alloy/environment combination which leads to the most severe cracking problems are required in both cases.

(9) The minimum concentration of the chemical species in the environment necessary to cause cracking is often very low (PPB levels) for both cases.

These similarities suggest a unifying underlying principle which serves as the theoretical basis for the occurrence of both or either cracking mode.

Clearly, there are alloy/environment systems that fail by SCC alone such as alpha brass in ammonia and those that fail by HEM alone such as high strength steels in moist air. Less evident are those systems which exhibit accelerated cracking that cannot be unequivocably identified as SCC or HEM. In such cases, hydrogen induced brittleness leading to crack initiation and propogation is called hydrogen assisted cracking (HAC) to distinguish it from the independent HEM failure mode. The distinction is largely semantic as both HEM and HAC refer to the same basic phenomenon, i.e. cracking induced by brittleness due to the presence of hydrogen . In that the mechanism of "true" SCC is then one of anodic dissolution along a preexisting susceptible path in the metal, it is frequently referred to as active path corrosion (APC). In order to clarify the distinction between the two processes, Figure 1 provides a pictorial representation [5]. In APC, the metal at the crack tip is the anode and hence oxidizes, hydrogen (or oxygen) then providing the concomitant cathodic reaction on the metal surface.

$$M = M^{+} + e^{-} \quad \text{(anode)}$$

$$e^{-} + H^{+} = H^{o} \quad \text{(cathode)}$$

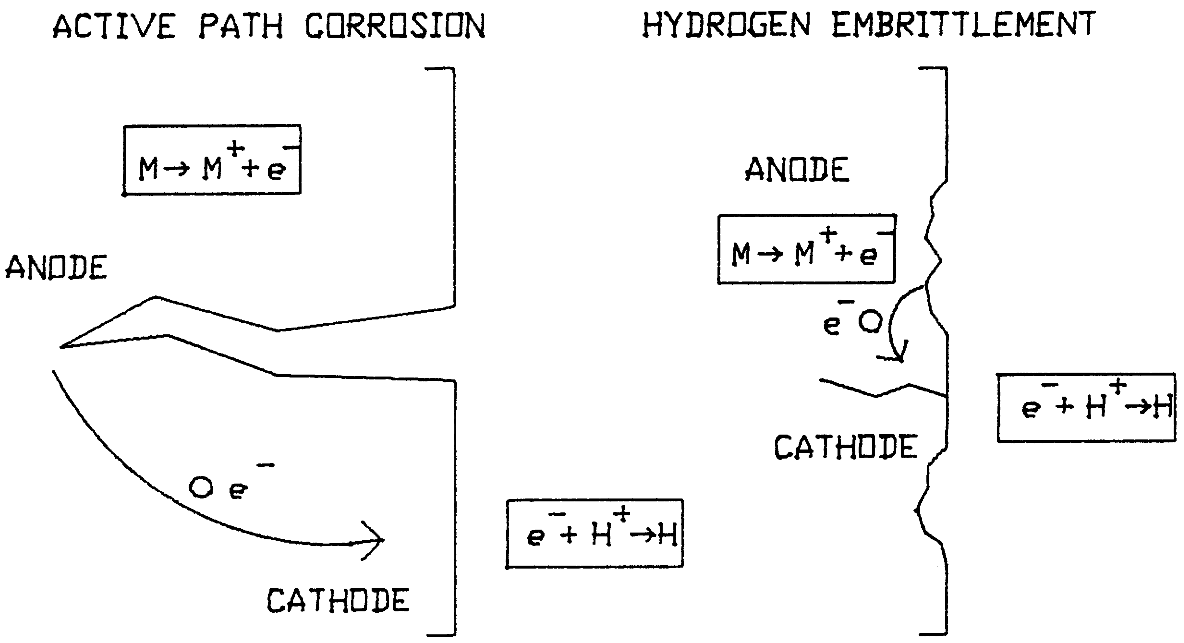

FIGURE 1 - Schematic of Cracking by Active Path Corrosion (APC) and Hydrogen Embrittlement (HEM).

In HAC, the same anodic and cathodic processes occur except that the anodic metal dissolution reaction occurs on the surface of the metal (vice in a crack) and the cathodic reduction reaction results in hydrogen embrittlement and ultimate cracking.

The lack of unequivocal distinction between SCC (or APC) and HEM (or HAC) leads one to consider both in any investigation of a material's susceptibility to either one. Classically (which in the corrosion field is as late as 1969), the distinction between SCC and HEM was experimentally discernable by varying the applied potential in a given test and observing the effect on the specimen's time to failure [6]. If the operative mode was APC, then making the potential more cathodic (less noble or more negative) would reduce the corrosion current and hence reduce the cracking and increase the time to failure (see Figure 2). On the other hand, if the operative mode was HEM, making the potential more cathodic would increase the hydrogen reduction reaction resulting in more embrittlement and decreasing the time to failure. Although this technique is valid in cases of SCC only or HEM only failure modes, it is invalid in cases where changing the corrosion potential in either direction reduces the time to failure. In other words, if raising the potential (i.e. more cathodic) results in a decreased time to failure and lowering the potential (i.e. more anodic) results in a similar effect, one cannot conclusively determine the operative failure mode (APC or HEM)> This has been observed

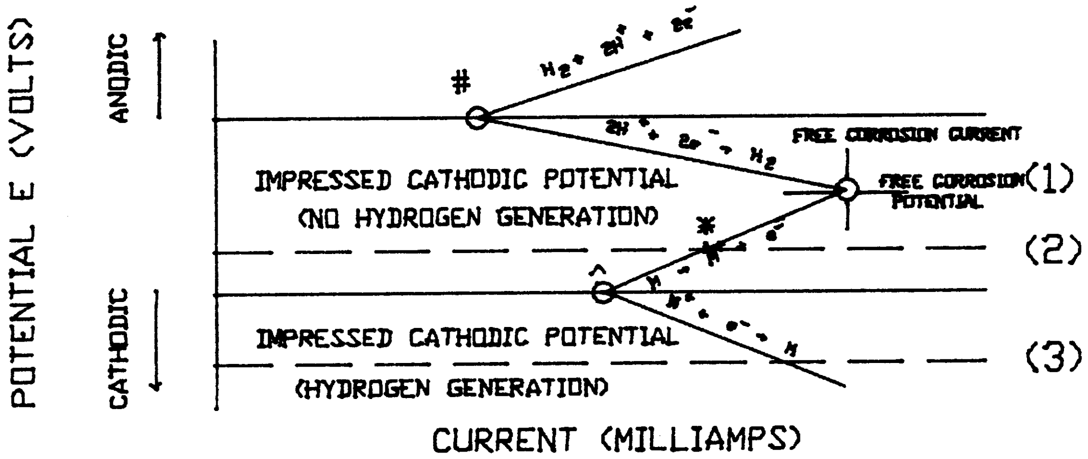

HYDROGEN CURRENT ON BASE METAL
* REDUCED CORROSION CURRENT
^ METAL ION CURRENT ON BASE METAL

(1) FREE CORROSION

(2) REDUCED CORROSION POTENTIAL RESULTS IN REDUCED ACTIVE PATH CORROSION (APC)

(3) FURTHER REDUCTION IN POTENTIAL RESULTS IN HYDROGEN GENERATION AND POSSIBLE EMBRITTLEMENT

FIGURE 2 - Effect of Variation in Potential on Corrosion Current.

with 12 percent Cr-martensitic stainless steel in aerated NaCl solutions [7]. One could perhaps simply infer from the observed failure behavior that increasing potential in the active or cathodic direction accentuated HAC and that increasing potential in the noble or anodic direction accentuated APC. This need not be (and probably isn't) the case [5].

The chemical conditions in a localized geometry such as at the tip of a growing crack may be radically different from those of the bulk electrolyte at the surface of the material. This should come as no surprise since the salinity and the temperature of sea water in a narrow inlet are often quite different from those of the adjacent ocean. The rationale for the divergence in measured property values is the same in both cases, that there is limited exchange between the crack or inlet and the bulk electrolyte or sea. As a consequence, the PH at the tip of a crack is acidic typically in the range of 3-4 regardless of the PH of the bulk electrolyte [8]. The acidity is of course dictated by the concentration of hydrogen ions which become plentiful at the crack tip. The mechanism for the production of the ions is theorized to be the hydrolysis of the anodic dissolution products at the crack tip:

$$M = M^{+} + e^{-}$$

$$M^{+} + H_{2} = MOH + H^{+}$$

Since the ions are restricted in their movement their concentration increases as the PH drops.

The potential at the crack tip can also be radically different from that at the surface of the metal. The constriction of the crack geometry provides a high resistance path through the essentially immobile electrolyte causing a potential drop from the surface to the tip [9]. When the surface is maintained at a noble potential, the crack tip is less noble whereas when the surface is maintained at an active potential the crack tip is more noble. This potential drop can be of substantial magnitude, often more than 1.0 volt.

The crux of the issue is that a propogating crack is an occluded cell [10] with a PH, potential and ionic species concentration that may differ substantially from the values of these parameters as measured at the surface. This means that both the metal dissolution of APC and the hydrogen evolution of HAC may occur at the crack tip regardless of bulk conditions. Thus, although the HEM and SCC phenomena are commonly distinguished (and in the more extreme cases distinguishable), there seems to be little justification for this [11]. If hydrogen promotes brittleness which ultimately results in cracking in a specific environment, one could just as easily call this SCC as HEM or HAC. Consequently, if one wishes to evaluate a material for SCC, one must investigate the effects of hydrogen with equal alacrity.

2.2 STRESS CORROSION CRACKING:

Stress corrosion cracking is cracking caused by the simultaneous presence of a tensile stress and an environment comprised of a specific corrosive medium [12]. Implicit in this definition is the fact that three major disciplines all play a role in assessing the overall problem:

(1) The electrochemistry of the alloy/environment system.

(2) The physical metallurgy of the material system insofar as grain boundaries, dislocations, inclusions and precipitates play a role.

(3) The fracture mechanics of the dynamic interaction of the crack tip stress field with the local geometry.

The complexity of the problem has defied explanation through a single unified theory. In fact, the search for one theory for all systems has largely given way to any theory that explains any single system. In order to achieve this elusive goal, one must address each of the three areas above in terms of [11]:

(1) The chemical reaction(s) which govern the formation and propogation of stress corrosion cracks.

(2) The microstructural features that impede or assist in cracking behavior.

(3) The nature of the stress/geometry dependence.

Thus, the nature of the realistic goal is to characterize a given material in a given environment in terms of its cracking susceptibility. Figure 3 schematically summarizes the many processes involved in SCC, graphically illustrating the conundrum of the research engineer.

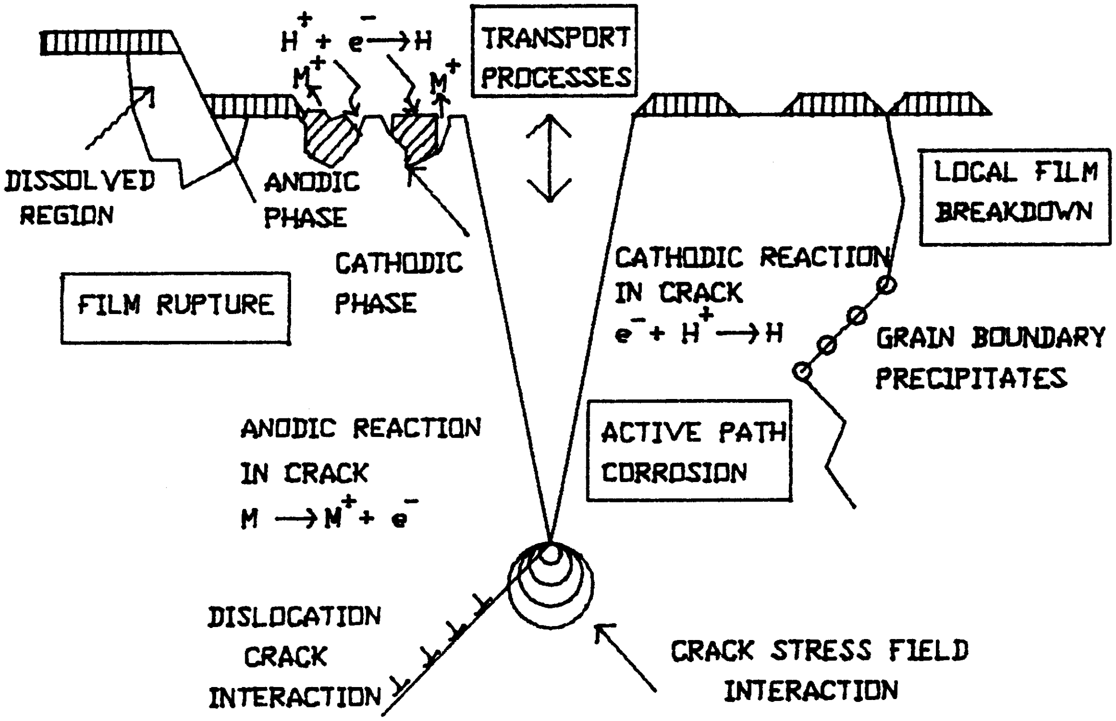

FIGURE 3 - Schematic of Microfeatures and Microprocesses Possibly Involved in Stress Corrosion Cracking (SCC).

The characteristics of SCC have been reviewed vis-a-vis their commonality with HEM characteristics. For the sake of completeness, however, a summary of shared, in addition to unique, characteristics would be appropriate as a starting point for an evaluation of current theoretical doctrine. Brown summarizes the characteristics of SCC as follows [13]:

(1) A tensile stress must be present which may be provided by loading, residual stress due to welding, etc.

(2) Generally, pure metals are immune.

(3) Chemical species causing SCC in an alloy are limited in number (specificity).

(4) A low concentration of the specific damaging chemical species is required to initiate SCC in an alloy.

(5) In some systems, SCC activation occurs only at elevated temperatures (e.g. austenitic stainless steel and chloride).

(6) Generally, the alloy susceptible to SCC in a specific environment is virtually inert with respect to that environment (i.e. in the absence of stress no appreciable reaction occurs).

(7) Cracks are brittle in appearance on a macroscopic scale even in demonstably tough materials.

(8) The microscopic SCC fracture mode is generally different from that of plane strain fracture (thick sections).

(9) In some systems, there is a threshold stress below which SCC does not occur.

It must be emphasized again that many of the above "characteristics" are general in the sense that exceptions do exist, further exacerbating the search for a unified theory.

From an electrochemical standpoint, Pourbaix [14] stresses the overriding importance of the difference in composition between the bulk solution and a restricted access region. The sequence of events from the electrochemist's point of view begins with the formation of a corrosion pit on the surface of the alloy at the electrolyte interface. Pit formation depends on either the existence of a defect on the surface (preexisting flaw) or on the establishment of a local anode due to the metallurgical inhomogeneities which cause localized potential differences. Thus, oxidation occurs at the anode according to:

$$Fe = Fe+2 + 2e-$$

and reduction occurs at the cathode:

$$2e^{-} + 2H^{+} = H_2$$

As shown on Figure 4, a porous cap of corrosion products then forms from ferrous-ferric compounds to impede electrolyte interchange and thus form the occluded cell. Within the cell, ferric and ferrous ions hydrolyze according to:

$$Fe^{+2} + 2Fe^{+3} + 4H_2O = Fe_3O_4 + 8H^{+}$$

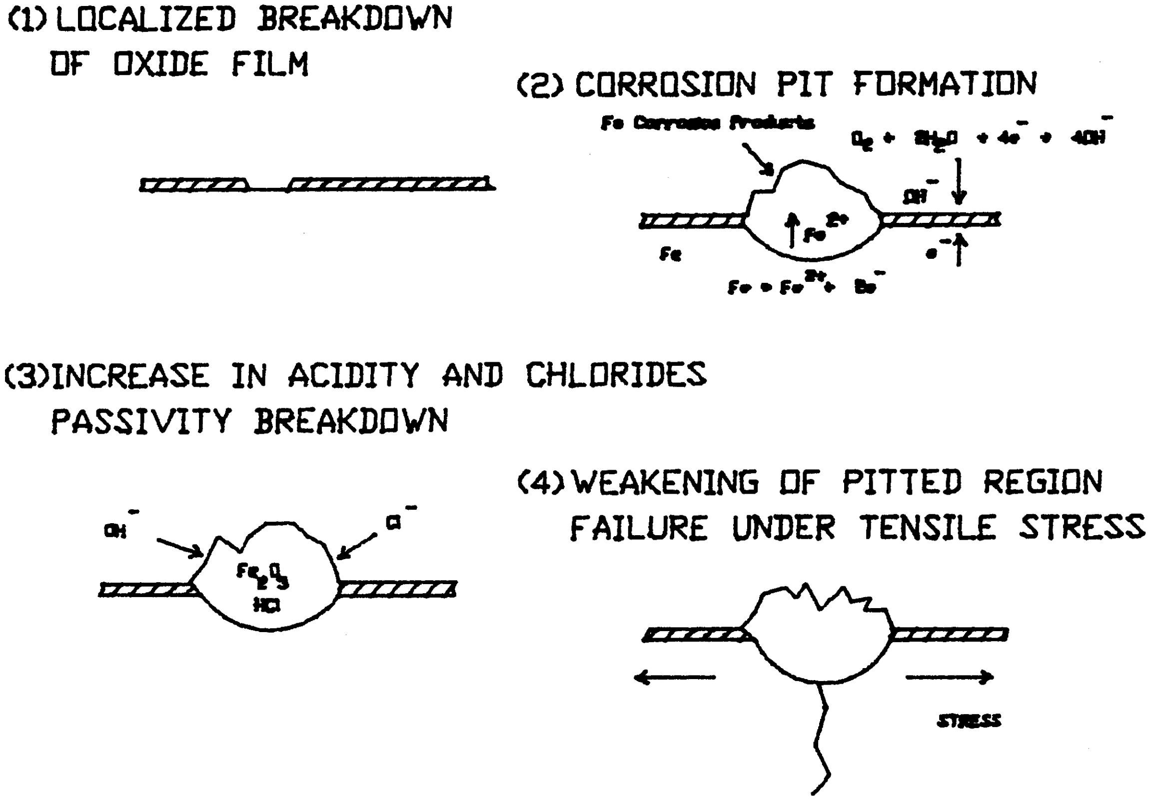

FIGURE 4 - Mechano-Electrochemical Model of Stress Corrosion Cracking.

which lowers the PH due to the hydrogen ion concentration increase and attracts anions (such as chlorides) due to the positive electrical charge and the requirement of electroneutrality. If a tensile stress is then applied to the system, a crack emanates from the pit, further restricting electrolyte replenishment and concentrating the damaging chemical species. As the crack propogates, new metal is exposed to the electrolyte to be attacked in turn until the component ultimately fails.

From the physical metallurgy standpoint, composition, structure/grain size, grain orientation and dislocations are generally considered to play a role in stress corrosion cracking [15]. The importance of composition rests with the experimental assertion that pure metals are (essentially) immune to SCC whereas alloys are not. Early research on the effects of alloy additions revealed that noble metal additions to a less noble base metal (e.g. gold added to copper) resulted in an increased susceptibility to SCC while less noble additions to noble metals had no effect [16]. The reason for this behavior would logically relate to the necessity of localized electrochemical discontinuities for the formation and propogation of corrosion cracks. Similarly, carbon and nitrogen additions to iron enhance susceptibility to SCC while aluminum and titanium additions purportedly reduce the susceptibility [15]. The only other two alloying additions with any reported effects are copper with a deleterious influence and chromium with a benificient one.

Structural effects are important as they relate to the grain size and the grain boundary composition. It is universally accepted that a smaller grain size reduces the susceptibility to SCC but there is certainly no consensus as to the reason. One explanation is that smaller grains increase the overall grain boundary length and therefore mitigate the weakening effects of grain boundary precipitates for a given volume fraction of precipitates. A second (and perhaps more plausible) explanation is that smaller grain size improves yield strength according to the Hall-Petch relationship (i.e. that the yield strength is inversely proportional to the square root of the grain size) and hence more stress is needed to initiate the stress corrosion crack [15]. The grain boundary composition is primarily responsible for the potential of transgranular or intergranular fracture. In ferritic steels, research has been predominantly limited to nitrate solutions as this is the environment to which these alloys are susceptible to SCC [17]. The intergranular cracking which characterizes the carbon steel-nitrate system has been attributed generally to the segregation of carbon compounds to the grain boundaries. This theory is experimentally justified by the observation that sub-critical annealing which spherodizes the pearlite and disperses carbide in globular form on the grain boundaries increases the susceptibility to SCC. In more general terms, Graf [16] asserts that the following rules can be established for transgranular and intergranular cracking:

(1) Intergranular cracks occur when the corrosive environment reacts with the less noble component of an alloy system.

(2) Transgranular cracks occur when the corrosive environment reacts with both the components of the alloy system.

The fact that both transgranular and intergranular cracks can occur in the same alloy/environment system would suggest, however, that there is no simple rule by which a specific fracture can be predicted.

Grain orientation refers to the angular difference between the adjacent grains boundaries of a microstructure. A large difference in grain boundary angle retains high grain boundary energy and increases susceptibility to SCC. The energy difference associated with high angle boundaries is small, however, when compared to the potential differences associated with other structural features such as phases and precipitates [17,18]. Hence, the effects of grain orientation should be negligible with respect to the more fundamental effects of grain composition and structure. Similarly, dislocations represent an analagous energy differential when compared to other electrochemical parameters and hence are believed to have marginal effect.

Finally, from the fracture mechanics standpoint, the effects of stress and strain on the susceptibility of a material to SCC are considered. Although it is clear that a tensile stress is required in order that SCC occur, it is by no means certain as to the actual role of the stress in a mechanistic sense. Among the more plausible explanations are [19]:

(1) The tensile stress allows the electrochemical process to occur by opening the crack, thereby allowing the passage of electrolyte and impeding corrosion product induced crack arrest.

(2) The stress induces plastic deformation at the crack tip to enhance localized electrochemical dissolution processes.

(3) The stress induces elastic deformation which provides the energy necessary for the electrochemical corrosion induced crack to propogate as a brittle fracture.

It has been suggested that the role of stress in crack initiation may differ from that of propogation to further complicate the process. A fourth mechanism that could explain the stress effect is that passivating oxide films that protect the metal surface are fractured sequentially to allow corrosion of the bare crack tip [20]. As the role of film formation and subsequent destruction under the action of a stress field is one of the main theoretical propositions, this subject will be discussed in some detail.

The field of linear elastic fracture mechanics (LEFM) has been successfully applied to characterize fracture behavior of high strength materials. The extension of the theory to the study of slow crack growth under static and dynamic loading, known as subcritical crack growth, has met with considerable experimental success [21]. Of fundamental importance to LEFM is the concept of the stress intensity factor K, which provides a single parameter characterization of the stress and displacement fields near the crack tip. The subscripts I,II, and III are applied to the cases of opening mode, edge-sliding mode and tearing mode respectively, K_I being the most important for typical load and geometry configurations. For the case of an isotropic elastic body loaded in mode I, the stress fields are given by [22]:

$$\sigma_x = (K_I /\sqrt{6.28\ r})*(\cos\{.5\theta\})*(1-\sin\{.5\theta\}\sin\{1.5\theta\})$$

$$\sigma_y = (K_I /\sqrt{6.28\ r})*(\cos\{.5\theta\})*(1+\sin\{.5\theta\}\sin\{1.5\theta\})$$

$$\sigma_{xy} = (K_I /\sqrt{6.28\ r})*(\sin\{.5\theta\}\cos\{.5\theta\}\cos\{1.5\theta\})$$

where the radial (r) and angular (θ) dependence are as shown in Figure 5. Clearly for a given position ahead of the crack, the stress is uniquely determined by K_I according to the theory. From the practical side, these equations do not apply as r approaches zero for this would require infinite stress and the material would yield to prevent the mathematical singularity. Secondly, they provide only approximate solutions for large values of r, i.e. at relatively great distance from the crack tip. Thirdly, and most importantly from an experimental standpoint, the dimensions of the material (i.e. crack length, specimen width, specimen uncracked ligament, etc.) must be large in comparison to the

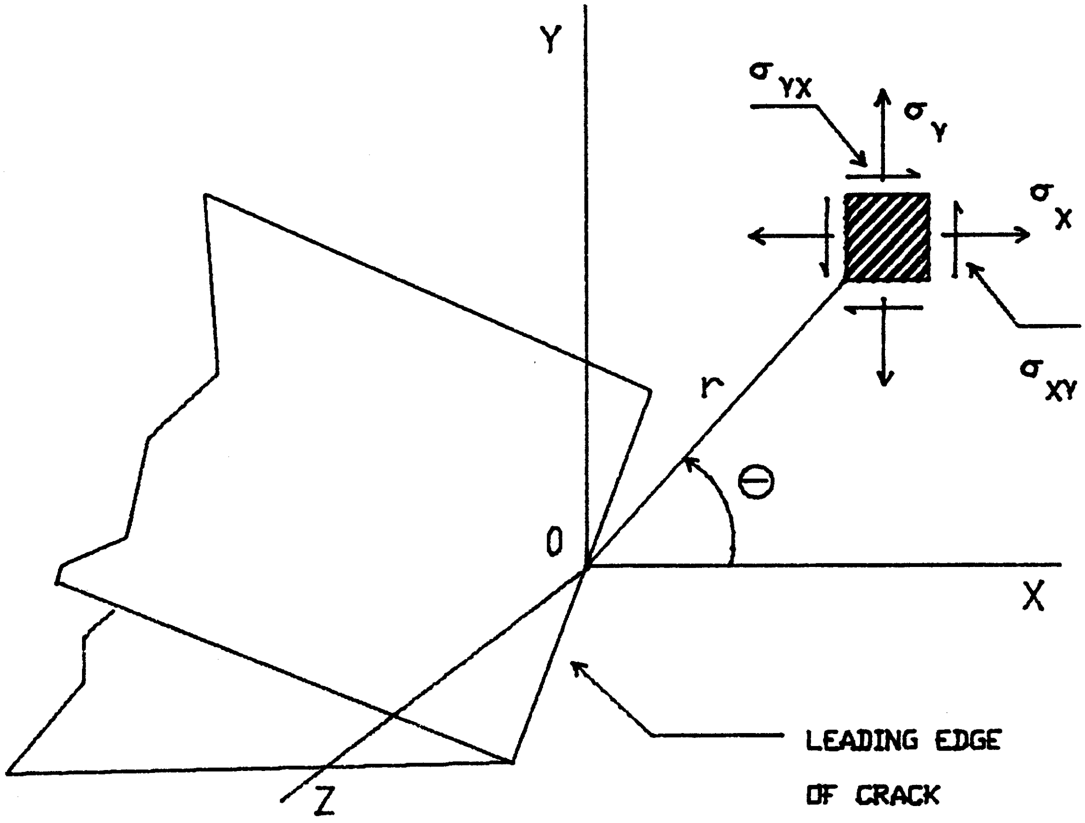

FIGURE 5 - Coordinates and Stress Components in the Crack Tip Stress Field.

plastic zone size of the crack tip so that errors introduced by plastic flow are minor or adequately corrected. This last requirement can be particularly difficult to meet, particularly in tough materials as is HSLA-80.

The stress intensity at which the limiting condition of fracture is reached is called the critical stress intensity factor or fracture toughness K_{IC}. It is a material parameter in the sense that it has a finite value for a given material and a given crack geometry. Analytical expressions for K_I in terms of various dimensional parameters have been worked out for a wide variety of geometric configurations. For example, that for a semi-infinite plate subjected to uniaxial tensile stress with an internal crack of length 2a is given by [23]:

$$K_{IC} = \sigma_f (\sqrt{6.28a})$$

with the units of either MPa times the square root of meters or ksi times the square root of inches. In SCC testing, this concept is extended to that of threshold stress intensity. By successive reductions in loading on a precracked specimen, the level of stress intensity K_I below which no failures are observed to occur can be determined experimentally. This threshold stress intensity, K_{ISCC} is of significant import in that it provides a measure of stress corrosion cracking susceptibility when compared to the critical stress intensity factor K_{IC}.

The application of LEFM to materials with a high toughness presents a practical insurmountable problem due to the presence of a significant amount of plasticity. Based on the characteristic dimension of the size of the crack tip plastic zone, ASTM Procedure E399 [24] requires that the specimen thickness and the crack length be greater than:

$$2.5(K_{IC}/\sigma_{YS})^2$$

where σ_{YS} is the yield strength (.2% offset) and K_{IC} is the plane strain fracture toughness. Hence, the specimen must be large compared to this characteristic dimension. For steels with high toughness (such as HSLA-80 and HY-80), this dimension is on the order of ten centimeters, making testing impractical. This practical limitation will be further addressed in the testing section.

The theories proposed to explain the stress corrosion cracking phenomenon reflect the mechanistic and electrochemical dichotomy of the operative environmental and material properties discussed above. The theories are generally broken down into four basic categories although this is far from universal. The specificity of the particular alloy environment combination has led researchers to explore the intricacies of each particular theory grouping leading to further breakdown of theoretical explanation into the nuances of relative contributions of one effect over another. Nevertheless, the four basic theory grouping retains some validity in terms of organizing the efforts of experimentation [5]:

(1) <u>MECHANO-ELECTROCHEMICAL</u>: This model emphasizes the importance of the mechanical processes of stress and/or strain at the tip of a growing crack. These mechanical effects may be caused by applied or residual stresses which result from fabrication processes such as welding or by metallurgical configurations such as grain size or the extent of grain boundary precipitation. In any case, the mechanical effects serve to promote electrochemical dissolution at the crack tip by making these areas more anodic or active than the surrounding material. Cracking then proceeds by the combination of the mechanical and electrochemical mechanisms operating sequentially through the material.

(2) <u>FILM RUPTURE</u>: This model stresses the importance of the formation of passivating films on the exposed surfaces of susceptible materials. As these films are broken, small regions of bare metal are exposed which then become anodes to the relatively large passivated cathodic surface. The film breakage is mechanically induced, possibly by the emergence of dislocations at the crack tip. The small anodes are rapidly corroded with a mechanism similar to that subscribed for pitting or crevice corrosion leading to crack extension.

(3) **EMBRITTLEMENT:** This model postulates the creation of a brittle film which grows into the metal immediately behind the corroding surface. The brittleness of the film then allows for cracking under the action of stress.

(4) **STRESS SORPTION:** This model deviates from classical theories in that it emphasizes the importance of surface energy in the SCC process. In this sense, it is the "modern" theory and attempts to explain a variety of embrittlement phenomena (including the hydrogen embrittlement of the next section) on the basis of energy. Fundamentally, the model predicts the reduction of the energy required to form a new surface by the adsorption of surface active species in the vicinity of the crack.

Each of the above theories has its adherents and detractors with the requisite experimental evidence to defend their individual positions. The complexity and specificity of the SCC process suggest, however, that all have some validity in one or more material environment systems but that none are universally true. Following a more detailed review of the theories, an overall assessment of current doctrine will be formulated.

The Mechano-Electrochemical Theory was the natural end result of the history of the discovery of SCC as a potentially severe material problem. It reflects the piecemeal understanding of the fundamental process. "Season cracking" is the earliest widespread instance of SCC [12]. It occurred initially in brass cartridge cases that were cold drawn so as to hold the bullet in place; The season modifier referring to its appearance only during certain months of the year (later attributed to the environmental presence of ammonia). Professor W. Chandler Roberts-Austen [19] provided the first insight into the occurrence of season cracking by demonstrating that it was not restricted to just brass and by postulating the necessary role of tensile stress. "Caustic cracking" of riveted boiler steel in an environment of free alkali observed in the late nineteenth century provided another indication that SCC was not limited to any one metal or alloy and further suggested the importance of the specificity of the environment [12]. As further examples of specific instances of cracking in material/environment systems were recognized in the process of technological development in the early twentieth century, the three discernible elements of SCC became manifest: mechanics, metallurgy and the chemistry of the environment. Aluminum alloys cracked in atmospheric moisture, mild steel failed when subjected to the nitrate environments of the chemical industry and stainless steel was subject to cracking in both chloride and caustic environments at elevated temperatures. Then, as now, the problem of SCC was solved on the practical level by changing one or all of the three required ingredients.

With the advent of microscopy to probe the inner workings of the cracking process and linear elastic fracture mechanics to characterize the crack tip stress field in the 1960's came the inception of the mechano-electrochemical body of theoretical research. The theory in its most fundamental sense is that the stress at the tip of the crack causes it to become anodic with respect to the crack sides and thus stimulate dissolution. The inception of the theory is generally attributed to Dix [25] who proposed that the function of the stress was to "pull the metal apart along more or less continuous localized paths." This newly exposed metal, anodic to the surface, would hence accelerate corrosion and "result in further tearing of the metal." From this somewhat simplistic point of departure have come the myriad claims and counterclaims of subsequent researchers, the debate centering predominantly on the role of stress as a corrosion enhancer. Harwood [26], for example, agrees that "...the nature and propogation of stress corrosion cracks indicate strongly that crack propogation is primarily mechanical." His overall explanation of the model is much more complex, however, reflecting an increased role of stress, above and beyond that of merely holding the crack open:

(1) Trench-like fissures are created by corrosion at local sites.

(2) Stress concentration develops as the fissure grows deeper and sharper causing localized plastic deformation.

(3) A brittle crack is initiated which propogates some distance through the material until stopped by a grain boundary, an inclusion or by stress relaxation.

(4) The exposed surface is rapidly corroded with little or no crack extension until the new surface is passivated by a protective film.

(5) The process repeats as stresses again build up.

The synergistic effect of stress and corrosion are thus emphasized in this version of the theory.

Refinement of the role of stress in the Mechano-Electrochemical Theory has been the focus of succeeding experiments. Parkins [27], in studying SCC of mild steels in nitrate solutions noted that the intergranular nature of the cracking was due to distortion induced stress along the grain boundary caused by precipitation of carbide particles. These microstructures in the area of distortion then create the anodic site necessary for corrosive attack. This corollary to the basic theorem has been subsequently upheld by follow-on researchers (regardless of their theoretical persuasion) but it should be noted that it applies only to those systems which form grain boundary precipitates and is hence somewhat limited in application.

On a somewhat different tack, Hoar [28] evaluated SCC of austenitic stainless steels in 42 percent aqueous magnesium chloride and of alpha brass in ammonia. He concluded that the local rapid ductile yielding at the crack tip, i. e. the strain, caused by the raised local stress accounted for the stimulation of anodic dissolution. As further evidence of this strain assisted dissolution, he pointed to indications from previous experiments of a threshold strain at about .1

percent of proof stress below which SCC did not occur. The physical crack extension was postulated to occur when dislocation pile-ups emerge at the crack tip to initiate slip bands. This was supported by arguing that materials with restricted slip (low stacking fault energy) were generally "cracking" types whereas those with extensive cross slip high stacking fault energy) were not; the slip restriction contributing to the necessary pile-up of dislocations in sufficient magnitude to cause cracking. Once the new metal is exposed by cracking, it then becomes subject to anodic dissolution. The crux of the distinction is then that where stress assisted cracking emphasizes the "energizing" of the material at the crack tip, strain assisted cracking emphasizes the deformation along slip bands. In that both then allow for anodic dissolution, the essential mechano-electrochemical model remains substantially the same.

The final major modification to the Mechano-Electrochemical Model which will be considered is the localized pitting or tubular form of attack proposed by Pickering and Swann [29]. Following detailed observation of the microstructures of copper-gold, copper-aluminum, copper-zinc, and magnesium-aluminum alloys after exposure to both cracking and non-cracking environments, they ultimately concluded that "compostitional rather than physical disturbances initiate preferential chemical attack on the surface of the alloys studied." The stress assisted and strain assisted cracking mechanisms are thus discounted as inconsequential or, at best, of secondary importance. Their observations indicated that tubular corrosion pits were initiated at surface sites which contained a compositional fluctuation of the alloy rather than at static dislocation sites. The mechanism postulated was that:

(1) A protective film forms over a major portion of the surface. The sites of compositional fluctuation change the composition and structure of the film over them, rendering it less protective.

(2) Pitting corrosion ensues at these sites as a local electrochemical cell is established which prevents film formation and passivation and enhances anodic dissolution.

(3) The pitted region becomes mechanically weakened, allowing for ductile failure through the corroded material along active slip planes.

(4) The process is autocatalytic as new surface with the requisite compositional fluctuations is exposed.

Thus, the Mechano-Electrochemical Theories all attempt to explain SCC on the basis of the synergism of a mechanical process with the electrochemical dissolution of a corrosion cell. It is in the characterization of the mechanical process that the distinctions arise. A schematic of the process is shown in Figure 4.

The Film Rupture Theory, although originally postulated by Mears, Brown and Dix [25], has been largely attributed to Logan [30] who first proposed it as part of a generalized theory in 1952. Recognizing the dearth of experimental measurements of the electrochemical potential at the root of a crack with freshly exposed metal, and further noting that the limited testing that had been done indicated a tendency toward electonegativity (anodic) in this area, he devised an experiment to measure the potential. Using six notched tensile specimens in corroding electrolytic solutions, he measured the potential changes during the course of a slow strain rate tensile test. The resultant changes in electrochemical potentials are as shown in Table 2.1 below:

TABLE 2.1

ELECTROCHEMICAL POTENTIAL CHANGES

MATERIAL	ELECTROLYTE	POTENTIAL
245-T4 Al Alloy	Saturated KCl	0.610
70%Cu-30%Zn Brass	5% Ammonium Hydroxide 5% Ammonium Carbonate	0.700
61%Cu-36%Zn-3%Pb Brass	Same as above	0.510
AZ31 Magnesium Alloy	3.5% NaCl 2% Potassium Chromate	0.240
Low Carbon Steel	5% Ammonium Nitrate	0.160
302 Stainless Steel	Saturated KCl	0.315

These values were obtained at their maximum point when the specimen failed and reflect large amounts of exposed material. In general, the transient behavior of the potential was such that rapid increases accompanied the plastic deformation of the specimen (i. e. beyond the yield point). From this data, it was postulated that, as the specimens were stressed in tension, minute areas of the specimens were broken without substantive plastic deformation of the underlying material which then became electronegative with respect to the filmed surface. Since the area of these exposed points was small, corrosion would proceed at a rapid rate until a change in electrochemical conditions supported a reformation of protective film cover. If no changes occurred, the cracking would be continuous whereas if the film reformed, cracking would be discontinuous. The film rupture theory was thus considered as requiring a stress only insofar as the protective film ruptured, the corrosion alone being responsible for the subsequent cracking.

The fundamental tenets of the Film Rupture Theory have changed very little over the decades since its inception. McEvily and Bond [31] studied stress corrosion cracking of alpha brass in ammoniacal copper sulfate and concluded that the experimental results were best supported by the film rupture theory of Logan. Their observations indicated a three step process of (1) crack initiation, (2) crack advance along the surface (in the film) and (3) crack penetration through the film into the base metal. Crack initiation was attributed to a decrease in the resistance to fracture of the film as it thickened rather than to the action of substrate dislocations. Cracks growing along the film surface were attributed to the low stacking fault energy (restricted slip) of the tarnish layer. Crack penetration was postulated as a continuation of the crack initiation process (i.e. the repeated formation and rupture of the film on thickening). The overall effect in support of SCC was that film rupture localized the effects of stress and environment to cause anodic dissolution at the crack tip without the need for massive plastic stress induced deformation of the substrate. Cracks were found to grow at a rate proportional to the square of the applied stress.

As a final note on the Film Rupture Theory, Scully [11] identified the rate of film formation as a critical step in the SCC process. The "repassivation rate" of the metal surface following film rupture is critical to the extent that an excessively high rate will cause either no attack or pitting (vice cracking) and a low rate will allow for general corrosion attack over a larger surface and hence prevent the localization necessary for SCC. The general argument is based on the creation of an area of fresh metal by the occurrence of a wide slip step (or some other stress induced deformation). The expanse of fresh metal is then such that repassivation cannot occur within the time available over the whole area. Figure 6 depicts the Film Rupture Model from the repassivation standpoint. Along the sides of the crack, passivation occurs as shown by the points 1. As the crack tip is approached (points 2 and 3), increasing halide ion concentration, diminished oxygen and falling PH inhibit film formation. If the current density at the crack tip (point 4) is high enough in relation to the current density near the crack tip, then a crack will propogate. If it is not high enough, the fissure will develop into a pit and blunt the crack. The specificity

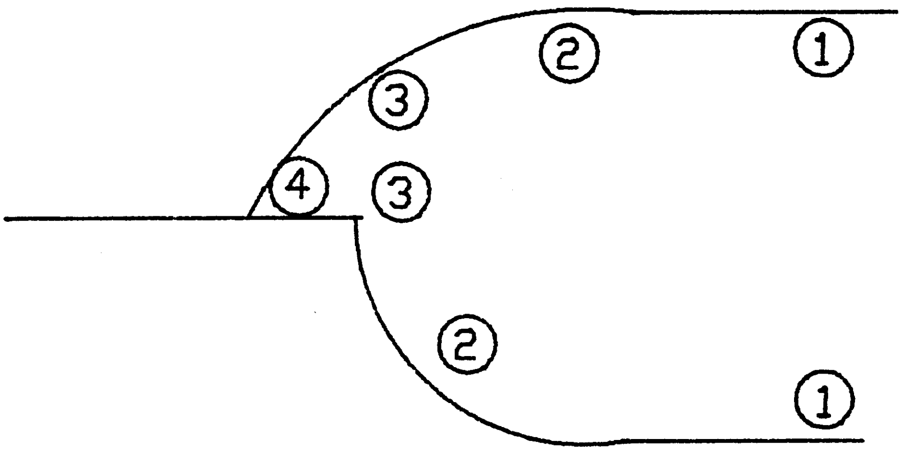

① PASSIVATION ALONG THE SIDES OF THE CRACK

② ③ INCREASING HALIDE CONCENTRATION, DIMINISHED OXYGEN AND FALLING PH INHIBIT FILM FORMATION AS THE CRACK TIP IS APPROACHED

④ CRACK PROPOGATES IF CURRENT DENSITY HIGH ENOUGH

FIGURE 6 - Schematic Representation of the Film Rupture Theory of SCC.

of the environment becomes important with regard to the relative concentration of aggressive ionic species (i.e. those which cause cracking or corrosion) and the concentration of passivating species. The metallurgical variables of the material become important with regard to the deformation and fracture mode which accompany an application of stress. The repassivation explanation of the Film Rupture Theory is more a refinement than a revision. The essence remains unchanged; that a small localized area becomes anodic with respect to a much larger filmed surface so as to promote corrosion induced crack growth.

The Embrittlement Theory is also a film theory to the extent that it addresses the role of a surface layer of a material adjacent to the environment. Although originally proposed by Edeleaner, it is widely attributed to Forty [32], who codified it and coupled it to experimental evidence. It is perhaps the least popular of the SCC theories since it is almost wholly phenomenological in its arguments and since the embrittlement of a material has been more recently attributed to hydrogen effects (to be discussed in the next section). The theory is based on the observation that the rate of cracking in SCC is intermediate between the rates for cleavage fracture and simple corrosive attack, suggesting a two-stage process. The first stage is the environmentally induced embrittlement of a surface zone deep enough to allow a crack to form. The embrittlement mechanism is one of selective dissolution wherein the least noble component of an alloy is preferentially attacked (e.g. dezincification of brass) leaving a sponge-like brittle surface layer. The second stage is then the formation of a crack due to the restriction in plastic deformation caused by embrittlement. The crack then propogates through the brittle surface layer, and, if it acquires a sufficient velocity, into the underlying ductile substrate. The crack continues until it is stopped within the metal due to a preexisting slip band or some other region where deformation can occur and absorb the stress. The process then begins anew with the first stage of selective leaching embrittlement. The uniqueness of the Embrittlement Theory lies within its assumption that there is no interdependence between applied stress and chemical attack, which would appear to be contrary to experimental evidence in many alloy/environment systems [32].

The Stress Sorption Theory of SCC is the most "modern" of the major theories and hence has limited experimental support. The general notion of stress sorption of surface active species causing a reduction of surface energy and hence a reduced fracture stress is generally attributed to Petch [33]. The application of stress sorption to SCC as a potential general theory is due primarily to the theories of Uhlig [6]. The basic argument proceeds from the notion that the Mechano-Electrochemical, Film Rupture and Embrittlement Theories do not take into account the required specificity of the environment and the inhibiting effects of extraneous ions. The Stress Sorption Theory, on the other hand, focuses on the environment in the sense that the adsorption of its constituent ions onto the surface of a stressed region controls the cracking behavior. The specificity of the environment is thus that only specific adsorbed species are effective in reducing the attraction of surface atoms for each other so that the bonds between them are weakened leading to crack initiation. The inhibiting effect of extaneous ions is explained by their displacement of the damaging species by "mass action" or by their effects on the corrosion potential to the extent that conditions are no longer favorable for the adsorption of damaging species. The potential shift argument applies equally to the effects of cathodic protection on SCC. As a metal is cathodically polarized, it is made more negative with respect to the environment and thus repels the negatively charged ions to prevent their adsorption. In support, it is generally true that cathodic polarization of metals impedes or prevents SCC whereas anodic polarization frequently enhances it. The virtual immunity of pure metals to SCC may be explained if one assumes that the chemisorption of surface active species can only occur on mobile dislocations or some other type of active imperfection that remains on the surface for an adequate time period. Since the microstructures of alloys impede dislocations more than do those of pure metals, the "surface time" of dislocations would be longer and hence chemisorption more likely. The influence of microstructure may be explained analagously (i.e. in terms of dislocation motion control). The Stress Sorption Theory thus represents a radical break from the classical notions in that the material is either totally irrelevant or relevant only from the standpoint of producing the damaging ionic species by electrochemical means.

The conclusion that must be reached in an evaluation of the above theories is that either a general unified theory has yet to be found or that SCC is in actuality a group of different mechanistic processes that share the common attributes of tensile stress, corrosive environment and susceptible material. The Mechano-Electrochemical Theory does not adequately explain the specificity of the electrolyte in causing cracking, for if the mere action of corrosion were necessary, then any electrolyte of comparable electrical conductivity would work as well as any other. This is clearly not the case. The Film Rupture Theory cannot be a general theory since SCC occurs in the absence of visible or suspected films (e.g. alpha brass in alkaline ammonium hydroxide). Further, SCC does not occur in pure metals which form brittle or cathodic corrosion films quite readily. Finally, chloride ions which break down oxide films and nitrate ions which favor oxide films act as SCC inhibitors in mild steel and austenitic stainless steels respectively. The Stress Sorption Theory requires that surface tension be reduced from about 1000 to 2000 $ergs/cm^2$ to about 100 $ergs/cm^2$ for the materials for which data are available. This reduction would in turn require extremely large adsorption energies (on the order of 100 kcal/mole) which have not been reported for metal-aqueous solution interfaces [34]. Further measurements of surface energy changes with ion adsorption and with reaction film formation are required to resolve this particular issue.

The failure of the theory in predicting the susceptibility of a specific alloy/environment system to SCC necessitates an experimental approach for design decisions. This has in general been the accepted engineering practice and has led to the development of "susceptibility" tables for specific alloys and environments. Tables 2.2 [12] and 2.3 [35] are examples of a general and a more specific SCC susceptibility assessment.

TABLE 2.2

ENVIRONMENTS THAT MAY CAUSE STRESS CORROSION CRACKING FOR SOME REPRESENTATIVE METALS AND ALLOYS

MATERIAL	ENVIRONMENT
ALUMINUM ALLOYS	$NaCl-H_2O_2$
	NaCl solutions
	Seawater
	Water vapor
COPPER ALLOYS	Ammonia vapors
	Amines
	Water vapor
ORDINARY STEELS	NaOH solutions
	$NaOH-Na_2SiO_2$
	Calcium, ammonium, sodium nitrate
	Mixed acids
	HCN solutions
	Acidic H_2S
	Seawater
STAINLESS STEELS	Acid chloride ($MgCl_2$, $BaCl_2$)
	$NaCl-H_2O_2$
	Seawater
	H_2S
	$NaOH-H_2S$

TABLE 2.3

ENVIRONMENTS VERSUS LOW ALLOY STEELS

1 RESISTANT
2 RESISTANT UNLESS HARDENED ABOVE RC=22
3 RESISTANT UNLESS HARDENED ABOVE RC=33
4 RESISTANT EXCEPT IN CERTAIN RANGES
5 NON-RESISTANT
X RAPID GENERAL ATTACK OR PITTING
A RESISTANT UNLESS ANODICALLY POLARIZED

	A516 (C-Mn)	A242 (HSLA)	A517 (HSLA)	AISI 4140
Cl^{-1} acid	X	X	X	X
Cl^{-1} neut	1	1	1	3
Cl^{-1} oxid	1	1	1	3
Seawater	1	1	1	3
Pure water	A			3
OH^{-1}	5	5	5	5
HCN	2	2	5	5
S^{-2}	2	2	5	5
Carbonates	4	4	4	4
SO_3	1	1	1	4
SO4	A	A	A	A
CrO_4	1	1	1	1
NO_3	5		5	5
NH_3	4	4	4	4
$CO.CO_2$	4	4	4	4
Amines	4	4	4	4

2.3 HYDROGEN CRACKING

Hydrogen, the most elemental of the identified chemical varieties, is also one of the most ubiquitous. As a key ingredient in both water and organic materials, it permeates the environment. Hydrogen has a very large mobility in metals, many orders of magnitude higher than that of other interstitially dissolved atoms [36]. It is thus able to penetrate to a greater depth and generally achieve a greater concentration so as to significantly alter the properties of the base metal matrix. From a strictly qualitative standpoint, the small size of the hydrogen atom relative to the interatomic spacing of metal atoms in a crystal lattice lends logical appeal to this observed phenomenon. For example, the hydrogen atom is only about .48 Angstroms in diameter whereas the spacing between adjacent atoms in a body-centered cubic iron structure is about 2.86 Angstroms. It is this high diffusivity that causes the permeation of the metal matrix and the subsequent alteration of its basic properties.

Once dissolved, the interaction of the atomic hydrogen with the metal results in what may generally be called hydrogen damage. This damage may take one of various forms which comprise four distinct types: the low temperature phenomena of blistering and embrittlement and the high temperature phenomena of decarburization or carbon removal and hydrogen attack [12]. In that the initiation and propogation of cracks in steels (particularly those that are high in strength) has been attributed at least in part to their embrittlement by the adsorption of monatomic hydrogen from the environment, this form of damage is of particular and wide-ranging interest. The fracture of metals when subjected to a hydrogenated environment has been further specified as hydrogen stress cracking or simply hydrogen cracking [37]. Its similarity in both apparent cause and effect to SCC has been previously addressed and will not be reviewed at this juncture [5]. Suffice it to say that the two mechanisms are unique enough to allow for individual consideration even though their ultimate engineering impact is the same: potentially catastrophic failure under the right conditions.

The evidence supporting the existence of hydrogen cracking is well substantiated. Alloy/environment systems which do not favor crack formation on the application of stress can be made to do so by cathodically polarizing the metal [37]. The cathodic polarization results in the release of hydrogen from the metal surface which can then diffuse as discussed previously so as to permeate the metal matrix. Although embrittlement may occur without other harmful side effects, subsequent cracking so as to cause degraded material performance requires the application of sufficient stress. In general, cracking is transgranular like SCC. An important exception to this behavior is found in the case of martensite, a high strength microstructure formed by rapid quench and the primary component of the HY series steels used in ship hull construction. Martensitic steels generally fail intergranularly along prior austenitic grain boundaries.

Hydrogen cracking, like SCC is a complex phenomenon and as such has eluded unequivocal scientific explanation. Numerous theories have been proposed and specific experimental results published in an attempt to fully characterize the process. The theories that have been proposed generally favor electrochemistry, fracture mechanics or surface chemistry, depending primarily on the qualifications of their proponents. The primary theories (to which their are numerous modifications) are:

(1) Pressure Theory.

(2) Lattice Decohesion Theory.

(3) Surface Adsorption Theory.

(4) Plastic Deformation Theory.

(5) Dislocation Mobility Theory.

The Pressure Theory is a logical starting point in any discussion of hydrogen embrittlement, as it is the oldest and simplest. The basic premise is that hydrogen enters the steel microstructure and collects in pockets until the pressure is so great that the elastic strength of the metal is exceeded. The metal then reacts by springing apart, causing cracking. Fundamental to the process is the variation of hydrogen solubility in iron with variation in temperature as shown in Figure 7. As steel cools, it is increasingly amenable to supersaturation with hydrogen and hence to accumulations of hydrogen under pressure. Since this stress is aerostatic, it is triaxial and the material can respond only by rupturing, for flow is not possible under these conditions. The fracture

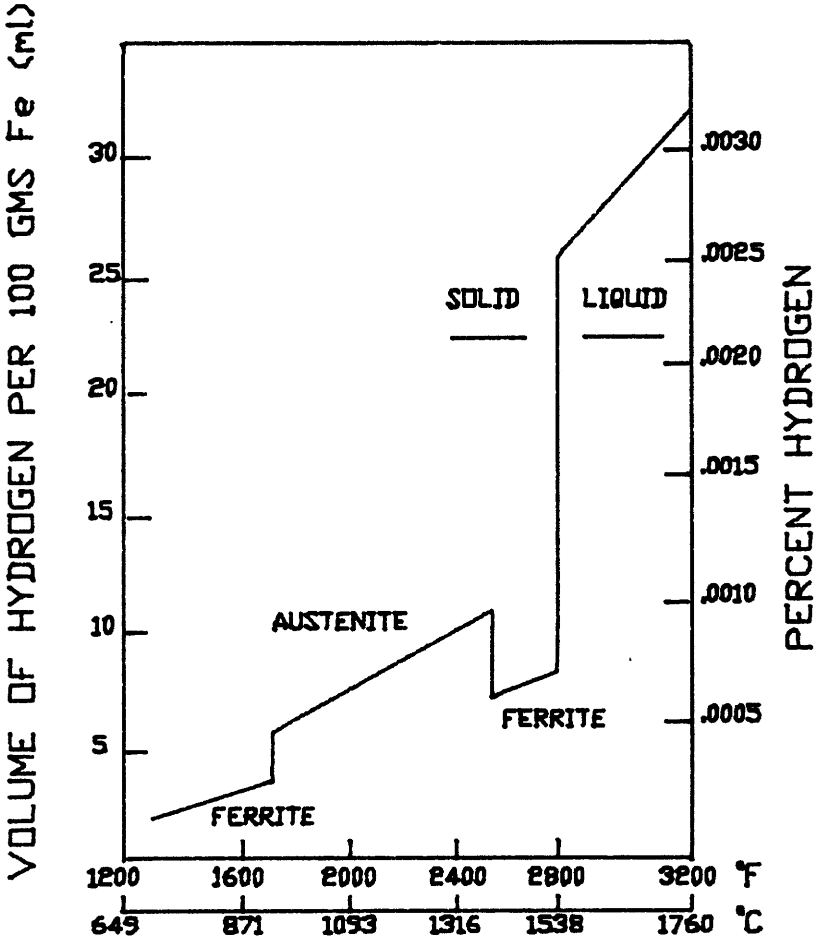

FIGURE 7 - Variation of Hydrogen Solubility in Iron with Variation in Temperature.

will proceed across the slip planes that are most favorably oriented to the imposed stress, exposing flat facets characteristic of the bright and shiny brittle fracture surface observed. Hydrogen accumulation within the metal will be exacerbated by the high concentrations of hydrogen on the metal surface. The accumulation of hydrogen pockets is a reversible process to the extent that aging the hydrogenated metal lattice at room temperature restores its ductility, the restoration rate depending on the aging temperature (i.e. higher temperatures result in higher diffusivity of hydrogen and hence allow it to migrate out of the metal lattice more rapidly). Hydrogen escape is afforded by either passage of molecular hydrogen to the surface or by re-solution of the hydrogen in the metal lattice due to the pressure buildup in the gas pockets. Figure 8 shows the effect of baking to remove hydrogen on the time to failure.

The inception of the Pressure Theory may be attributed to Zapffe and Sims [38], who postulated that various steel processing defects were directly attributable to hydrogen embrittlement. It has been refined since its initial inception and continues to provide a viable explanation for the observed material behavior. In a recent study [39], Beck et al measured the effects of stress and temperature on the permeation rate of hydrogen in several commercial grades of iron. The permeation rate was found to increase with increasing stress whereas the diffusion coefficient was constant (i.e. the fractional increase in permeation rate was

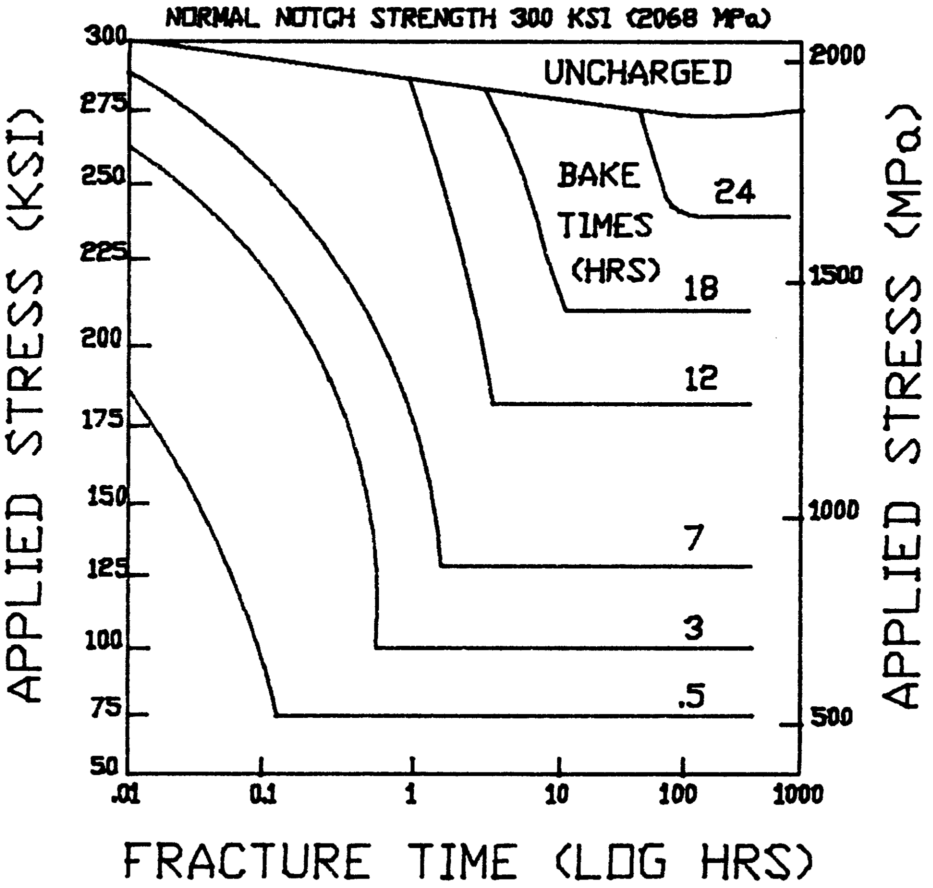

FIGURE 8 – Static Fatigue Curves for Various Hydrogen Concentrations Obtained by Baking Different Times at 300 degrees F.

the same regardless of the stress level). This was viewed as significant in that an increase in the permeation rate coupled with constant diffusion meant that the hydrogen must be accumulating within the metal lattice. Further permeation experiments revealed the existence of a critical hydrogen concentration above which the permeation transient displayed an anomalous peak value uncharacteristic of normal Fickian behavior [39]. The critical hydrogen concentration, though dependent on temperature, was found to be independent of the cathode side solution composition (numerous electrolytes were tried). It was hypothesized that the peak in the permeation rate marked the onset of embrittlement as follows:

(1) Low hydrogen concentrations do not "overload" the metal lattice and can pass through it without distortion.

(2) On reaching the critical concentration, the hydrogen can no longer readily diffuse and must then collect in pockets or combine with the metal atoms as hydrides (structural investigations gave no evidence of hydride formation, however).

(3) As the hydrogen collects at a void in the metal, pressure builds up resulting in a blister or crack.

(4) As cracks and blisters are formed, the ability of hydrogen to permeate the material is impeded, resulting in the observed reduction in the permeation rate.

(5) The growth rate of the crack then becomes dependent on the recombination of the hydrogen atoms at the metal surface (assuming anodic dissolution), on the elastic properties of the metal and on the hydrogen pressure.

The Lattice Decohesion Theory has its underpinnings in the "slow strain embrittlement" behavior of hydrogen induced cracking. Proposed originally by Troiano [40], the fundamental mechanism is dependent on two factors:

(1) The diffusion of hydrogen to a highly stressed region which is localized and segregated within the metal lattice.

(2) The embrittlement of the material at this localized point by the presence of hydrogen resulting in crack nucleation.

The proposition followed observation of the behavior of hydrogenated metals under the action of a statically applied stress. On varying the hydrogen concentration, it was found that all delayed failure parameters, i.e. notch toughness, rupture time and the static fatigue limit increased with decreasing hydrogen concentration (Figure 8). The increase in the lower critical stress (i.e. that stress level below which failure will will not occur) with decreasing hydrogen concentration intimates that cracking behavior is governed by a combination of hydrogen and stress.

Further experiments using the resistance of statically loaded hydrogenated metals to mark the onset of cracking revealed that a delay time or incubation period occurred that was strongly dependent on the hydrogen concentration but virtually independent of applied stress. As the hydrogen concentration increased, the incubation period decreased. This phenomenon was explained by considering that prior to the application of stress, a given amount of hydrogen is distributed uniformly in the metal. A certain amount of time is required on application of the stress by the test apparatus for the hydrogen to diffuse to the region of high triaxial stress induced by the action of the bulk of the metal on the crack tip. Once a sufficient "critical" concentration of hydrogen is reached in the highly stressed region, a crack forms and propogates.

If the initial crack formation depends on the accumulation of hydrogen to a critical level, then it stands to reason that once crack growth starts, it must be periodically arrested by the metal lattice until the hydrogen concentration can again build up to a critical value ahead of the crack tip. In other words, the crack grows out of the hydrogenated region and the highly stressed zone at the crack tip moves to a region of lower concentration. Hence, the growth of a crack due to hydrogen embrittlement must be a discontinuous process according to the theory. The macroscopic nature of crack growth measurement prevents observation of discontinuous extensions unless the temperature of the specimen is lowered sufficiently to retard hydrogen diffusion. If this is done, resistance measurements indicate the stepwise crack extension predicted.

Thus the Lattice Decohesion Theory proposes a mechanism wherein a normal fracture process is operative upon which is superimposed the effect of hydrogen embrittlement. Notches due to material or metallurgical defects act as stress concentrators which generate the sites for fracture in the form of blocked dislocation arrays which are stable. As hydrogen is attracted to the stressed region, the effects of hydrogen embrittlement are gradually manifested and the material cracks.

The Surface Adsorption or "Stress Sorption" Theory is less widely accepted than the two preceding theories. As originally proposed by Petch and Stables [33], it is identical to that proposed for the phenomenologically similar stress corrosion cracking. The adsorption of a surface active species such as hydrogen on a surface (which may be of the bulk metal adjacent to the environment or on the face of a notch or fracture) results in a reduction of the surface energy of the material. Thus crack formation is enhanced by a reduction in the fracture stress.

Support for the theory was originally somewhat limited due to the lack of direct measurements of the embrittlement kinetics of materials in gaseous hydrogen environments. In a recent study by Williams and Nelson [41], gaseous hydrogen embrittlement experiments were conducted on stress relieved 4130 steel in order to evaluate the validity of the theory. Fracture toughness and crack propogation tests were conducted and electron fractography used to evaluate the fracture surfaces. The investigation revealed that the apparent activation energy of gaseous hydrogen induced slow crack growth was 3900 cal/mole, much less than the 9000 cal/mole energy associated with the bulk transport of hydrogen to the crack initiation site. Further, no evidence of an incubation period such as had been observed with hydrogen charged steels was evident. The evidence suggests that since the transport of hydrogen is not the rate controlling step in the embrittlement process then the next most logical choice would be the adsorption of hydrogen on the metal surface. This choice is based on the fact that hydrogen adsorption behavior for varying temperatures is similar to that observed for the crack growth temperature variation. Based on the close agreement between the observed crack growth rate and that predicted theoretically by considering the adsorption rate of hydrogen, the latter is determined as the rate controlling step. This argument is extended by considering that measured crack growth rates are two to five orders of magnitude faster than the maximum expected diffusion rate. Thus bulk diffusion transport cannot be significant in its effect on crack growth, and the embrittlement of steels by gaseous hydrogen must be due to some type of surface reaction.

The argument is further extended to hydrogen charged steels by considering that the fracture behavior in both cases is similar. In hydrogen charged steel, hydrogen must first migrate to the void regions which form due to the application of stress (explaining the incubation time found in this case). The authors acknowledge the validity of the Pressure Theory in contributing to the stresses of the voids, maintaining that the surface adsorption energy effect must be superimposed to provide a truly valid embrittlement theory.

The Plastic Deformation Theory of Beachem [42] suggests that the presence of sufficiently concentrated hydrogen dissolved in the highly stressed region at the crack tip assists in the deformation process that is already operative. The mechanism for the assistance in the cracking process is proposed to be an unlocking of dislocations such that they can move at reduced stresses. Thus a rather significant break with previous theory is postulated in that reduced ductility inherent to embrittlement (which involves the locking of dislocations) is ruled out in favor of deformation enhancement.

In the development of the theory, four fundamental interactions between hydrogen and steel are asserted:

(1) Hydrogen is evolved and enters the metal lattice at growing crack tips.

(2) Pure molecular hydrogen gas dissociates at clean deforming surfaces and enters the metal matrix.

(3) Hydrogen migrates to regions of high triaxial stress at the crack tip.

(4) The presence of hydrogen aids in the deformation of the metal matrix.

The first three processes merely affect the supply of hydrogen to the fracture site whereas the fourth is proposed as the operative mechanism which increases the susceptibility to cracking.

In order to evaluate the four fundamental interactions in light of the proposed theory (i.e. that the processes of intergranular, quasicleavage or microvoid coalescence fracture are aided by hydrogen) three experimental procedures were devised using three types of steel. A comparison of a steel subjected to stress corrosion cracking conditions and subsequently to hydrogen assisted cracking (HAC) conditions revealed that the crack propogated in the same fracture mode in both cases, suggesting that HAC was the operative mechanism. Further evaluation of the HAC failure revealed that the crack had propogated by microvoid coalescence (MVC), clearly a ductile vice a brittle mode of failure. The most significant findings were that the HAC crack tips advanced by microscopic plastic deformation processes (the rate of advancement depending on the stress intensity factor) and that there were changes in the fracture mode associated with the decrease in plasticity. Figure 9 depicts the various fracture modes observed as a function of decreasing stress intensity.

The observations made of the fracture surfaces directly refuted the theories of Troiano and Petch [33,40]. The existence of extreme microscopic plasticity in the MVC fracture mode and the existence of tear ridges in the intergranular and quasicleavage modes directly refuted the Lattice Embrittlement Model of Troiano since the failure was ductile. The voids and the nucleii for quasicleavage and intergranular cracking were observed to initiate and grow well ahead of the crack tip, indicating that the Stress Sorption Model of Petch could not be operative since these areas were not exposed to the environment. Further, if stress sorption

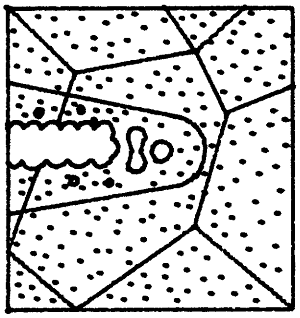

HIGH STRESS INTENSITY
MICROVOID COALESCENCE

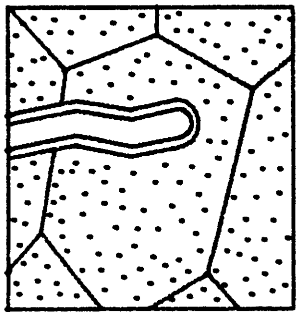

MEDIUM STRESS INTENSITY
QUASI-CLEAVAGE

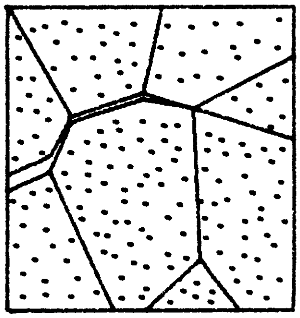

LOW STRESS INTENSITY
INTERGRANULAR FRACTURE

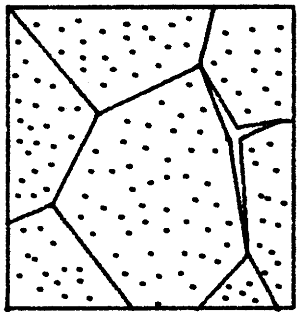

INTERGRANULAR FRACTURE
HYDROGEN ASSISTED

FIGURE 9 - Microscopic Fracture Modes as a Function of Decreasing Stress Intensity Factor and Decreasing Cracking Rate.

cracking were operative, one would expect to find either brittle cleavage facets due to the lowering of the cohesive bonds across cleavage planes or elongated tear dimples due to the lowering of the resistance of the surface atoms. Cracking was found to be discontinuous at high stresses supporting the Pressure Theory but no discontinuity in growth was noted at lower stress levels indicating that pressure buildup was not a factor.

The Plastic Deformation Theory fits well with most laboratory observations: The Planar Pressure Model at low stresses (where pressure then serves as the sole source of stress); The theory that hydrogen concentrates in high stressed regions; The theory that deformation "locks" hydrogen in place; The theory that hydrogen lowers the true fracture strength of the lattice. In attributing HAC to the effect of hydrogen on the plasticity of the metal lattice, Beachem's theory falls short in failing to identify the mechanism of this effect. A more recent study by Clum [43] suggested that this mechanism was the ability of hydrogen to catalyze the nucleation of dislocations and thus induce the plasticity identified by Beachem.

The final and most recent theory of hydrogen behavior in metals provides an explanation for the transport of hydrogen as one of the pivotal elements of Hydrogen Embrittlement Theory. This theory, called the Dislocation Mobility Theory, is not an omnibus proposal such as those previously discussed but rather an explanation for the specific mechanism of hydrogen movement in metals. The central tenet is that hydrogen does not permeate the metal by the process of lattice diffusion but rather by rapid dislocation sweeping, the dislocations effectively dragging a hydrogen cloud with them. The importance of the transport theory to hydrogen embrittlement is in the explanation of the ductile failure process wherein hydrogen can change the rate of microvoid nucleation and growth. Further, the theory provides an explanation for deep hydrogen penetration necessary for hydrogen to accelerate fatigue crack growth rates and for hydrogen participation in stress corrosion cracking (in which cracking rates exceed lattice diffusion rates).

The basic mechanism proposed by Tien et al [44] is that hydrogen atoms are bound to dislocations as they penetrate the metal lattice and are subsequently "stripped off" by microstructural discontinuities such as grain boudaries, inclusions and microvoids. The process is viewed as a three phase evolution; the adsorption of hydrogen gas on the surface and dissociation into H atoms, the transfer of hydrogen from dislocation to dislocation at the grain boundary, and the transport of hydrogen into the metal matrix.

As the hydrogen is carried into the metal, it may be given up at a lattice site (resulting in localized hydrogen enrichment) due to an increase in the speed of the dislocation, by the annihilation of the dislocation or by transfer of the hydrogen to a stationary sink such as an inclusion. The transfer of hydrogen to a sink is of special importance for it is through this mechanism that hydrogen contributes to local fracture processes. If the rate at which hydrogen arrives at a given sink is greater than the rate at which it diffuses into the surrounding matrix, then the accumulation of hydrogen must result in the rise of pressure in a void. An analysis of the mechanics of the two processes confirms that this is in fact the case except when the strain rate is very low (when hydrogen will permeate the entire matrix).

As recently as 1980 at the Third International Conference on the Effect of Hydrogen on the Behavior of Materials, it was concluded that although an understanding of the interaction of hydrogen with atomic structure, microstructure and defects was emerging, the mechanisms underlying this behavior had not yet been adequately identified. The failure to formulate a viable theory that explains the hydrogen embrittlement phenomenon is a direct result of the diversity of the susceptible alloy systems and the failure modes observed [45]. A consensus of opinion, however, supports the view that hydrogen plays a major role in the modification of the response to plastic flow in ferrous alloys. The failure process is then closely connected to these hydrogen modified plasticity effects (such as strain localization).

Although many questions remain unanswered, a basic outline of hydrogen interaction may be formulated:

(1) Monatomic hydrogen is generated at the surface of the metal by either direct charging or by cathodic electrolytic action according to:

$$H^{+} + e^{-} = H_{adsorbed}$$

where the recombination of the adsorbed monatomic hydrogen may or may not be impeded by the formation of metal oxides in regions of high metal ion concentration (such as would be the case in a crevice, crack or pit) according to:

$$M^{+} + H_2O = MOH + H^{+}$$

(2) The hydrogen is transported into the metal matrix primarily by dislocation sweeping and secondarily by direct diffusion, this being conclusively demonstrated by Tien et al as previously discussed [44].

(3) The deposition of the hydrogen within the metal lattice is a function of the microstructure of the metal:

(a) Grain boundary precipitates will result in hydrogen accumulation at grain boundaries.

(b) Finely dispersed precipitates will result in hydrogen accumulation and void formation in the vicinity of the precipitates.

(c) Internal voids or pores will likewise result in hydrogen accumulation and void growth.

(d) Dislocation tangles (as would be present in heavily cold worked material) will result in hydrogen accumulation at adjacent sites which link up to form voids.

(4) The failure mode depends on the mode of hydrogen accumulation; grain boundary precipitates causing cleavage or intergranular fracture, dispersed precipitates causing transgranular or microvoid coalescence depending on the degree of dispersion, and voids, pores and dislocation tangles causing ductile failure due to void growth and adjacency (again microvoid coalescence).

(5) The failure process proceeds discontinuously as the hydrogen permeates further into the metal, pausing as necessary to build up sufficient pressure.

The understanding of the mechanisms of hydrogen damage in metals is thus far from complete and the prevention of such damage in susceptible metals is not possible. The techniques employed to minimize hydrogen damage are largely empirical in nature and use a combination of proper material selection and hydrogen exclusion as preventive measures. This is particularly true in the case of weldments as discussed in the next section.

2.4 WELD CRACKING

Cracks in weldments are classified according to two general groupings which characterize their appearance, location and the conditions under which they are formed [46]. In terms of location, cracks are classified as transverse if they are perpendicular to the weld axis, longitudinal if they are parallel to the weld axis, and crater if they occur as a result of a cessation of welding on the open face of the weldment. Cracks in the base metal are likewise categorized as transverse and longitudinal as above with a further specification of toe and root cracks according to their position relative to the weld. In terms of conditions of formation, cracks which form near the bulk solidus temperature are called hot cracks and are characterized by intergranular fracture as a result of differences in the freezing temperatures of the various alloys comprising the weldment. Cracks which form at lower temperatures (below 400 degrees F) are called cold cracks and are characterized by transgranular fracture and bright oxide-free surfaces. Cold cracks are further classified as short-time cracks or delayed cracks depending on the time period required for their appearance. In that hot cracking is induced by metallurgical factors and cold cracking by environmental factors, further discussion will be restricted to the latter.

The environmental conditions needed for cold cracking are inherently present in the region of a weldment unless specific measures are taken to modify them. These conditions are [47]:

(1) A critical concentration of hydrogen exists at the crack tip.

(2) Stress is applied at a level above a certain critical magnitude.

(3) A microstructure is produced that is susceptible to cracking.

(4) Temperature is in the range of -150 to 400 degrees F (-101 to 204 degrees C), depending on the specific alloy.

Hydrogen introduction into the weldment occurs as a direct result of the welding process since the welding arc is capable of dissociating diatomic hydrogen into the inimical monatomic variety. Sources of hydrogen include atmospheric water vapor, moisture absorbed in the welding electrode flux, hydrocarbon flux compounds, and various contaminants containing hydrogen present due to the lack of adequate cleanliness control at the worksite. Tensile stresses are inherently present due to the thermal effects of cooling and may be further exacerbated by poor weld fitup. The heat affected zone microstructure becomes susceptible to cracking if the thermal transient is such that the steel is forced to attempt to transform rapidly from austenite (face centered cubic) to ferrite (body centered cubic). Rapid quenching of austenite does not allow time for atomic reorganization into the BCC lattice structure, and the FCC structure essentially collapses into a high strength (and hence hydrogen cracking susceptible) microstructure called martensite. It is in this portion of the weldment that cracks are inevitably found. Finally, the low temperature requirement is directly related to the solubility of hydrogen in steel. As the temperature drops, hydrogen solubility drops and hence the hydrogen becomes trapped within the metal matrix providing the catalyst for cracking as discussed in the previous section.

The prevention of hydrogen induced cold cracking is thus dependent on the control of any one of the four prerequisites. In that the operative mechanism of hydrogen induced cracking is itself a subject for conjecture, its prevention is dependent on empirical measurement and field experience. Controlling the requirements for cracking is no simple matter, as hydrogen is ubiquitous and highly mobile, high residual stresses and a hardened microstructure are inherent to the thermally transient nature of the weld process and the temperature of virtually all operational systems falls within the susceptibility range. Nevertheless, it can be prevented if proper procedures and rigorous controls are methodically adhered to. The only available alternatives are to restrict welding to noncritical applications or to accept a periodic (and unpredictable) catastrophic failure of a weldment, neither of which is acceptable.

Perhaps the most obvious preventive measure is to limit the amount of hydrogen present in the weld metal, thereby minimizing the source of the problem. This can be done in two ways; by restricting initial absorption or by facilitating the diffusion of that which is absorbed. As previously mentioned, sources of hydrogen include flux moisture, flux compound constituents, and atmospheric or work area contaminants. Therefore, hydrogen cannot be totally excluded but its concentration can be minimized so that no damage will occur (since we know from the theory of hydrogen embrittlement that there is a critical concentration).

When welding high strength steels, low hydrogen processes are used to prevent cracking. The sensitivity of a particular steel may first be determined by reference to the Carbon Equivalence (CE), which is a simple mathematical relationship which expresses the effects of various alloying elements in terms of the carbon effect (on hardness). One of the numerous formulas developed is [46]:

$$CE = C + \frac{Mn}{6} + \frac{Ni}{20} + \frac{Cr}{10} + \frac{Cu}{40} - \frac{Mo}{50} - \frac{V}{10}$$

which indicates susceptibility to cracking if the value exceeds 40. When a particular steel meets the criterion, a low hydrogen electrode is chosen to make the weld. These electrodes are produced under careful quality control so that the amount of moisture in the electrode is kept to a minimum. The higher the yield strength of the metal for which the electrode is intended, the lower the allowable moisture percent (for example E110XX electrodes which are rated at 110 ksi (758 MPa) must be maintained at a moisture content below .2 percent). In order to retain the low moisture content, these electrodes must be transported and stored in hermetically sealed containers and removed just prior to welding. It is possible to bake the electrodes if high moisture content is suspected or if the time limit for exposure to the atmosphere has been exceeded (also a function of the electrode type).

In order to further reduce the hydrogen level in the weld, it is possible to use a different welding process, such as Gas metal Arc (GMA) or Gas Tungsten Arc (GTA) welding. These processes employ inert gas to completely shield the weld area and do not employ flux. Similarly, the Submerged Arc Weld (SAW) process restricts atmospheric contamination by completely covering the work area with flux. The moisture problem is hence largely eliminated in welds employing these techniques. Figure 10 [48] compares the various welding processes in terms of potential hydrogen levels, a measure of the ability of the individual processes to exclude hydrogen.

A final technique which may be employed to reduce the hydrogen level in the weldment is to heat treat the weld area subsequent to welding (called post heat treating). Since the solubility of hydrogen in the metal increases with increasing temperature, the effect of post heating is to allow time for the hydrogen to diffuse out of the weldment and into the atmosphere as hydrogen gas. The obvious drawback is the expense of providing and running electric heaters in addition to the incorporation of yet another thermal transient that must be controlled and accounted for.

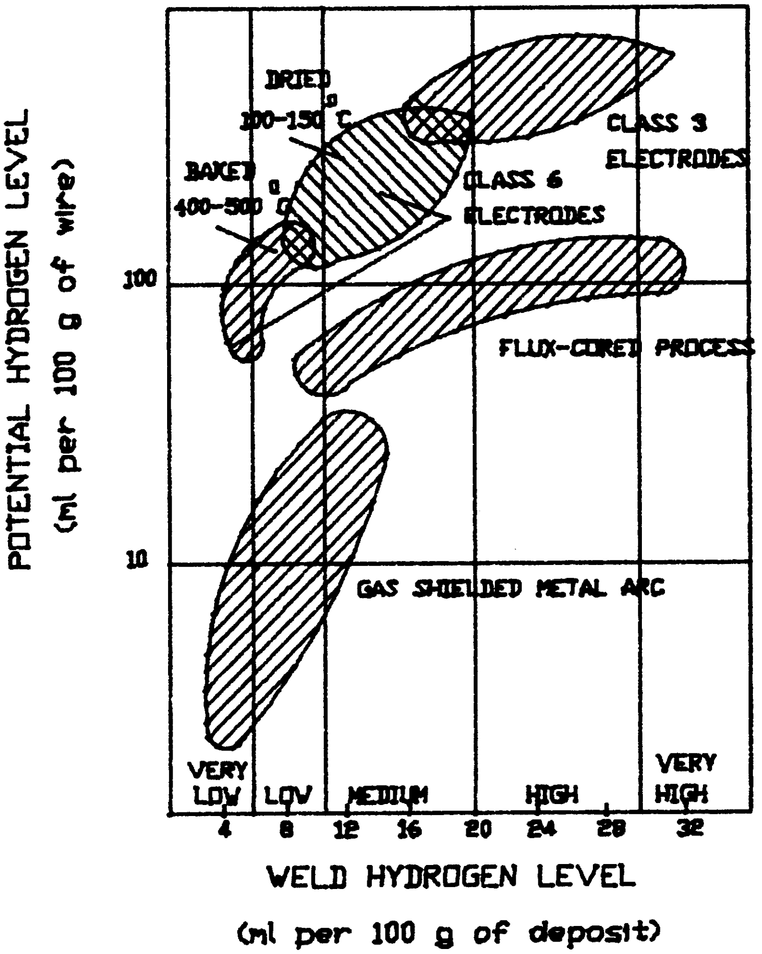

FIGURE 10 - Relationship between Potential Hydrogen and Weld Hydrogen.

The stress acting on a weld is a function of the weld size, fitup, geometry of the joint, and the yield strengths of the base and filler metals. Once a particular weld is specified, the only variable which can then be controlled is the fitup, which is quantified as the joint restraint. It has been found in practice that joint gaps in excess of 0.4 mm greatly increase the risk of cold cracking [48]. Thus, the control of the stress level in the weldment depends on good engineering practices, i.e. using the minimum strength weld metal allowable for the application, designing low stress weld geometries, and machining and cold working as necessary to achieve a close tolerance unstressed joint prior to welding.

The microstructure in the vicinity of the weldment is dependent on the type of material being welded, the weld metal and on the thermal transient to which the region is subjected. As previously discussed, carbon steels are particularly susceptible due to the formation of martensite. The problem of susceptible microstructure can be corrected by choosing a different material for the specific component or by heat treating the weld after completion of welding to restore the microstructure in the HAZ to a more ductile configuration. The use of alternative materials is currently of major interest due to the recent development of HSLA Steels. However, given a specific material, the only solution to the microstructure problem is the application of heat to restore the properties of the weld region or to limit the cooling rate such that hard microstructures are not formed.

The last variable is of course the temperature level since hydrogen cracking can only occur at near ambient conditions. Thus maintaining the temperature above about 400 degrees Fahrenheit until the hydrogen has diffused away and/or until the microstructure has been tempered will serve to prevent cracking.

In a pragmatic sense the solution to the hydrogen problem is to know which material/environment combinations are susceptible and to remove one of the requisite conditions. This is certainly not the best answer in that process requirements such as pre and post heating and electrode moisture control are expensive and unreliable since they depend on procedures that must be strictly adhered to. In the far term, the codification of hydrogen damage into a reliable and accurate mechanistic process may provide the answer for its prevention without resort to extravagant procedures. In the near term, the best answer is in the development of materials with adequate strength properties that are not as susceptible to damage, such as HSLA steel. Controls on the size, shape and quantity of inclusions, minimizing the grain size, and optimizing the type and distribution of precipitates all serve to minimize the aggregate effects of hydrogen.

3. MATERIAL

3.1 HSLA STEELS

High strength low alloy (HSLA) steels represent the results of over half a century of research and development with alloying additions and heat treatment variations to optimize mechanical properties. HSLA steels combine high strength with high toughness that is not significantly degraded by the thermal transients inherent to welding process during fabrication. At the current state of the art, HSLA 80 is being mass produced to a modification to ASTM specification A710 Grade A Class 3 with a minimum yield strength of 80 to 99.5 ksi (552 to 686 MPa) and a fracture toughness of 60 ft lbs at 0 degrees F (81.4 joules at -17.7 degrees C), 35 ft lbs at -120 degrees F (47.5 joules at -84.4 degrees C) [49] in order that it conform to HY-80 specifications (ASTM A 710 Grade A Class 3 requires 85 ksi {586 MPa} yield strength with a fracture tougness of 50 ft lb at -80 degrees F {67.8 joules at -62.2 degrees C} [50]).

The motivation for conformance to and proven parity with HY 80 requirements and specifications is one of economy. HY 80 is a quenched and tempered steel product that derives its yield strength from a tempered martensitic microstructure. The complicated heat treatment needed to manufacture the steel plate requires extensive controls in welding and fabrication in order that adequate strength and toughness are retained. HSLA 80, in deriving its mechanical properties from microalloying and a less exotic heat treatment process, is less difficult and hence less expensive to fabricate.

The developmental histories of HY 80 and HSLA 80 are distinct in spite of their apparent similarity in mechanical properties. HY 80 and its HY 100 derivative are based on a German Krupp steel of the 1890's employing the C-Mn system with a pearlitic microstructure [51]. This steel, as forged, could be produced with a yield strength of up to about 40 ksi (275.8 MPa). Further strength improvements required quenching and tempering to produce the harder martensitic microstructure. With the increased use of welding in the fabrication process, the need arose for a high strength steel product with relatively low carbon content so that toughness could be retained. In addition, thick sections were required for desired structural applications. These requirements led to the development of the HY series of steels with relatively low carbon content (.18% maximum), a tempered martensitic structure, and alloy additions of Ni, Cr, Mn and Mo to attain the requisite through thickness properties [52].

The development of HSLA steels was the result of an entirely different metallurgical process, the development of which was chronologically later than the quenching and tempering of the C-Mn HY steels. The evolution of HSLA type steels dates from about the turn of the century when the design engineers of the Queensboro Bridge which was to span New York's East River requested a stronger steel to minimize structural dimensions and weight [53]. In response to this request, the Carnegie Steel Company developed what may be called the first "high strength low alloy" steel which contained 3.25 percent nickel. Subsequent experimentation with additions of various elements to achieve higher strengths resulted in the identification of silicon and manganese as strength additives. The earliest "modern" HSLA steel was produced by US Steel in 1933 and marketed under the brand name COR-TEN. This steel was a modern HSLA steel in that it combined the economically appealing attributes of high strength, high ductility, formability and weldability with adequate corrosion resistance. The unique combination of both high strength and high ductility was achieved by the addition of small amounts of various elements (including the everpresent carbon and the silicon and manganese mentioned previously) to create the "high strength low alloy" product.

In their initial developmental stages, HSLA steels were called "weathering" steels with 4 to 8 times the corrosion resistance of carbon steel and yield strengths of about 50 ksi (344.7 MPa) [54]. A typical chemical composition of this type of HSLA steel is [55]:

TABLE 3.1

HSLA WEATHERING STEEL COMPOSITION

CARBON	0.10
MANGANESE	0.35
SILICON	0.50
COPPER	0.40
PHOSPHOROUS	0.10
NICKEL	0.40
CHROMIUM	0.80

Carbon was added to increase strength since it was inexpensive and produced a yield strength increase of about .5 ksi (3.5MPa) per .01 percent. The problem with simply adding carbon is that the strength increase is at the expense of lower ductility, notch toughness and weldability (later HSLA steels limit carbon to low levels to improve toughness, gaining strength from other alloy additions). Phosphorous, silicon, copper and manganese were added to increase yield strength by solid solution strengthening. Manganese provided the additional benefit of combining with sulfur, a common contaminant in the ingot melt due to its natural occurrence in iron ore. Sulfur has been blamed for the "hot shortness" of steel which manifests itself during hot working in the form of cracks or extremely roughened surfaces [53]. Manganese reduces the solubility of sulfur by forming the insoluble FeS compound. Copper also has a secondary beneficial effect in that it is by far the most potent of all common alloying elements in improving atmospheric corrosion resistance. Finally, chromium and nickel were added primarily to improve hardenability. The effects of these additions on yield strength are depicted in Figure 11.

The "second phase" of HSLA development was a direct result of the discovery that additions of small amounts of certain elements further improved yield strength by reducing the ferritic grain size. In the current lexicon, this process is known as microalloying. The first microalloying element to be used extensively in production mills was vanadium,

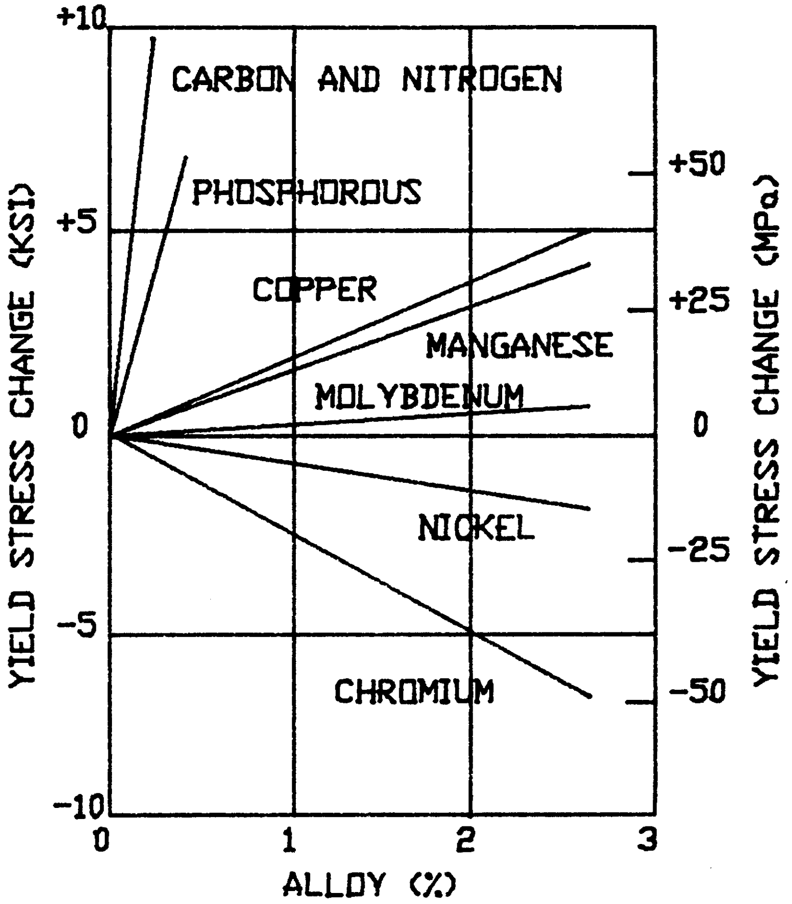

FIGURE 11 - Effect of Substitutional Alloys on the Yield Strength of Mild Steel.

imparting a 2 ksi (13.8 MPa) increase in yield strength for every .01 weight percent addition. These steels were called "controlled-rolled" steels since they were produced by rolling at lower than normal temperatures, taking advantage of the suppression of austenitic grain growth by the vanadium additive [51].

Niobium largely supplanted vanadium as the primary microalloying element as it became more readily available in the late 1950's. Extensive research has been undertaken in order to understand the mechanism of niobium interaction so as to provide a basis for optimum alloy composition. In essence, this research [56] has revealed that niobium in supersaturated solution prior to hot deformation retards austenitic recrystallization by precipitation of very fine (about 20 nm) particles of niobium carbonitride. The mechanism is postulated as a pinning of the grain boundaries of the austenite so as to prevent grain growth, and is supported by theoretical energy balance considerations. The net result is an increase in yield strength of about 6 ksi (41.4 MPa) per .01 weight percent or about 3 times the effect of vanadium. Since nature is rarely unilaterally benign, the quid pro quo for improved strength is reduced notch toughness. Restoration of adequate notch toughness requires lower temperature rolling to produce ultrafine grain ferrite, an expense that must be considered as an offset to using less niobium than vanadium. A comparison of the grain size effects of niobium and vanadium is shown in Figure 12 [57].

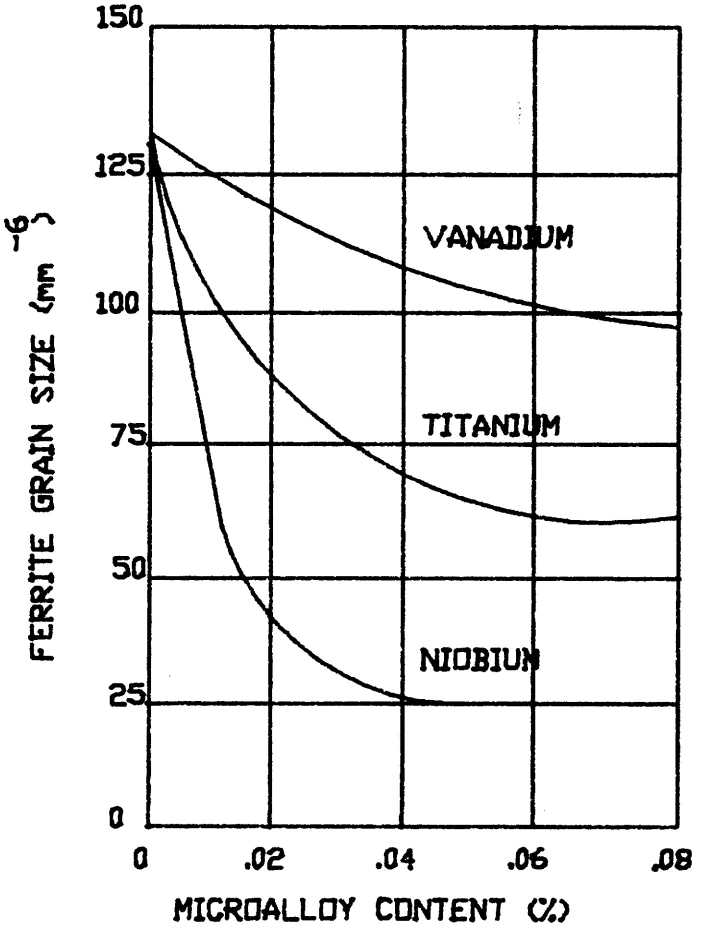

FIGURE 12 - Effect of Microalloy Content on Ferritic Grain Size.

In addition to the weathering and controlled-rolled HSLA steels, specific material engineering requirements have led to the development of a number of other varieties including pearlite reduced, dual phase, acicular ferrite and bainitic HSLA steels [54,58]. Pearlite reduced steels are simply those in which the carbon level has been decreased so that a reduced amount of cementite is available for pearlite formation. Adequate strength is attained through judicious addition of chromium, copper and especially molybdenum. Dual phase HSLA steels are comprised of islands of martensite or bainite in a ferrite matrix. The two phase microstructure is created by annealing an HSLA plate (after hot and cold rolling) in the austenite plus ferrite temperature range (about 1400 degrees F {760 degrees C}) to create islands of austenite. Subsequent cooling transforms the austenite to either bainite (slower cooling) or martensite (quenching), creating a dispersion of hard particles in the ferrite matrix [59]. Acicular ferrite HSLA steels derive their strength from the highly irregular ferrite grains that are formed when a bainitic transformation occurs. Since the acicular ferrite microstructure provides a large number of mobile dislocations and high residual stresses, these steels exhibit a high rate of work hardening. Finally, bainitic HSLA varieties combine low carbon levels with controlled cooling to produce nearly 100 percent bainite. Of particular interest are the ultra low carbon bainitic (ULCB) steels which have high levels of manganese and some boron. These steels have a very fine grain size with excellent strength and toughness properties [51].

On a somewhat independent path, the benefits of adding copper to the iron melt was recognized primarily as a corrosion resistant enhancement. Copper containing steel was actively marketed by the American Tin Plate Company as early as 1911 [54]. In the early 1930's, research was initiated in order to ascertain the nature of the interaction between copper and iron so that strength and corrosion resistance could be optimized through judicious choice of melt composition and heat treatment. The operative strengthening mechanism was identified as precipitation hardening. In an early work, Smith and Palmer [59] conducted a detailed study of the precipitation hardening phenomenon in order to determine its dependence on variations in heat treatment and composition. They concluded that steels which contained more than 0.7 percent copper were capable of being hardened by precipitation, the degree of strengthening increasing to a maximum at 1.5 percent copper and then declining.

The process required solutionizing at above 1470 degrees F (799 degrees C) to ensure that all of the copper was dissolved in the iron matrix followed by air cooling (vice quenching) and subsequent reheating to precipitate the copper particles. Maximum hardness was obtained by reheating for 24 hours at 842 degrees F (450 degrees C), 4 hours at 932 degrees F (500 degrees C) or 15 minutes at 1112 degrees F (600 degrees C). Increasing the carbon content was found to reduce the improvement in yield strength due to copper precipitation while increasing the overall yield strength of the steel due to higher base levels inherent to increased carbon concentration. An example of a typical steel (containing 1.45 percent copper and .202 percent carbon) is as follows:

TABLE 3.2

PRECIPITATION HARDENED COPPER STEEL

	YIELD STRENGTH KSI (MPa)	TENSILE STRENGTH KSI (MPa)	ELONGATION 2 IN (50 mm)	RED. OF AREA (%)
NORMALIZED TO 1470 DEGREES F (799 DEGREES C)	69.6(479.8)	85.2(595)	29.5	60.1
REHEAT TO 842 DEGREES F (450 DEGREES C) FOR FOUR HOURS	90.0(620.5)	107.8(743)	23.5	54.8

The primary perceived benefit of the copper steel heat treatment was that a stronger product could be produced without resort to quenching with its attendant danger of warping and cracking; the required heat treatment being relatively benign and simplistic. Historical hindsight reveals a different benefit; that of the forerunner to microalloying as a strengthening technique in general and of the copper precipitate HSLA 80 in particular [60].

3.2 A710 CLASS 3 HSLA STEEL

3.2.1 DEVELOPMENT

The combination of copper precipitation hardening to niobium microalloyed HSLA steels led to the ultimate development of the Navy's HSLA 80. In spite of the fact that copper precipitation was recognized as a viable hardening mechanism as early as 1933, commercial development of copper bearing steels was limited to the improved corrosion resistance and mild strengthening until as late as 1967 [60]. The significance of the cooling rate in controlling the amount of copper in solution for subsequent aging precipitation having not been fully appreciated, producers could not achieve an economically viable steel product.

In the mid 1960's, industrial demand for a high strength, high toughness, weldable and relatively economic steel led to the reevaluation of the potential for copper steel strengthening. Drawing on the experience of United States Steel in their manufacture of COR-TEN (0.40% Cu, .30% Ni) and on the demonstrated effects of niobium in improving strength, the International Nickel Company (INCO) undertook a composition study of an age-hardenable nickel-copper-niobium steel [61]. The development of the steel was based on the choice of copper to provide age hardening through precipitation of the epsilon phase. The cooling rates needed to retain the copper in solution and the subsequent heat treatment required to precipitation harden the material were anticipated to be readily adaptable to existing mill facilities and procedures. The primary disadvantage of copper in steel is its tendency to cause edge cracking during hot rolling. Consequently, nickel was chosen as the second major alloying element since the hot shortness effects of copper were known to be mitigated by the toughening effect of nickel when added in a ratio of at least 1 Ni to 2 Cu. The third major alloying element chosen was niobium due to its demonstrated strengthening effect when added in small percentages.

Initial experimentation with small steel heats focussed on studying the effects of varying the amounts of the primary constituents (plus carbon) on the mechanical properties of the product. This compositional study indicated that 1.3 % copper provided optimum strengthening, that .85% nickel prevented edge cracking and improved toughness and that .03% niobium would significantly improve strength. Carbon, the traditional steel strengthener, was found to have only a moderate effect on ultimate tensile strength and virtually no effect on the yield strength while lowering the reduction of area from 75.2% at .02% carbon to 59.0% at .19% carbon, a considerable loss in ductility. Preliminary investigations of the effects of molybdenum, manganese and chromium gave evidence of strength improvements at the expense of notch toughness. Finally, lower hot rolling finishing temperatures were prescribed as beneficial to yield stress. The product steel, named "Nicuage" [62] was recommended with the composition and properties delineated below:

TABLE 3.3

NICUAGE PROPERTIES

CARBON	0.05
MANGANESE	0.55
SILICON	0.28
NICKEL	0.90
COPPER	1.25
NIOBIUM	0.03

FINISHING TEMPERATURE	1600 DEGREES F (871.1 DEGREES C)
YIELD POINT	70-100 KSI (482.6-689.4 MPa)

With the advent of pipelines extending to the farthest and coldest reaches of the North American Continent came the need for pipeline steels that could withstand the permafrost soil conditions. Although "Nicuage" had shown good notch toughness at moderately low temperatures (.5 inch {12.7 mm} plate had a notch toughness of 71 ft lbs at -75 degrees F {96.3 joules at -59.4 degrees C} and .325 inch {8.26 mm} plate had a notch toughness of 53 ft lbs at -100 degrees F {71.9 joules at -73.3 degrees C} [61]), the arctic requirement was more stringent. In the early 1970's the International Nickel Company developed IN-787 as a modification to Nicuage to meet these requirements. The primary difference between the two steels was the addition of small amounts of chromium and molybdenum so as to delay autoaging on cooling after hot rolling to optimize the benefits obtained from the aging treatment [63]. Modification of the aging time and temperature parameters revealed that the notch toughness could be substantially improved by prescribing a specific heat treatment process. Optimal low temperature toughness (the 15 ft lb {20.3 joules} Charpy V-notch transition temperature was measured at -115 degrees F {-81.4 degrees C} as compared to -15 degrees F {-26.1 degrees C} for Nicuage) was achieved by austenizing the steel at 1650 degrees F (898.8 degrees C) for 30 minutes followed by water quenching and a one hour age at 1200 degrees F (648.9 degrees C). The composition was as specified below:

TABLE 3.4

IN-787 COMPOSITION

CARBON	0.04
MANGANESE	0.50
SILICON	0.28
PHOSPHOROUS	0.025
SULFUR	0.025
NICKEL	0.90
CHROMIUM	0.60
MOLYBDENUM	0.20
COPPER	1.20
NIOBIUM	0.05

Subsequent to the development of IN-787 as a line-pipe steel for cold weather applications, it became evident that its excellent toughness and relatively high strength would make it a potential candidate for offshore and ship hull applications. Consequently, a three year test program was undertaken to determine its performance in the corrosive sea water environment [64]. Having previously established the strength and toughness properties of the steel, it remained only to determine the corrosion behavior of the base plate and of welded sections (as virtually all marine structures are welded vice riveted). General corrosion was determined to be less than that for other low carbon steels currently in use by the marine industry. There was no evidence of selective corrosive attack at or near the weldments. Stress corrosion cracking was evaluated by subjecting weld metal and base plate U-bend specimens (the U-bend providing the requisite tensile stress) to sea water. The specimens were cathodically charged to -1250 mv referenced to a saturated calomel electrode to create a hydrogen charging environment (the potential of steel cathodically protected by zinc anodes is about -1000mv) [3,49,65]. The IN-787 alloy exhibited excellent SCC resistance; no cracks were observed after a period of more than one year. The conclusion reached was that IN-787 could be used with confidence by the offshore and shipbuilding industries. A standard specification for the steel was requested and approved by the American Society for Testing and Materials as ASTM A710 in 1979 [50]. The composition is specified in Table 3.5 below.

TABLE 3.5

ASTM A710 GRADE A HSLA STEEL

CARBON	0.07
MANGANESE	0.40-0.70
PHOSPHOROUS	0.025
SULFUR	0.025
SILICA	0.40
NICKEL	0.70-1.00
CHROMIUM	0.60-0.90
MOLYBDENUM	0.15-0.25
COPPER	1.00-1.30
NIOBIUM	0.02

The demonstrated potential of HSLA steels for ship applications effectively mandated an official evaluation by the U. S. Navy, an historical supporter of the research and development of high strength steels. An exploratory development program was thus started in 1981 by the Naval Sea Systems Command (NAVSEA) to identify candidate steels for warship hull and topside structural applications. The impetus for the program was economic in the sense of reduced fabrication expense and in the sense of reduced "weight expense". Reduced fabrication costs were postulated on the advertised (and to some extent demonstrated) weldability of HSLA steels without the need for expensive preheating and postheating of the weld joint. Reduced "weight expense" was also related to weldability in that the stronger HSLA could be used to replace the ubiquitous High Tensile Strength (HTS) Steel in thinner sections without additional material and fabrication costs. Since structural weight comprises the largest total percentage of a ship's overall displacement, reducing this weight could provide either a smaller vessel with the same operational capability or allow for increased payload weight for a given displacement vessel to enhance mission performance.

At its inception, the NAVSEA program was directed at the development of thin section HSLA steels for lightweight topside structures and thick plate high toughness steels for hull and framing applications. The thin section program task was distinct in that it focussed on the use of existing HSLA steels to take advantage of their formability in ship deckhouse construction. The development of HSLA varieties with enhanced strength and toughness was hence not required as yield strengths in the range of 60 to 80 ksi (413 to 552 MPa) were readily attainable in numerous existing production steels. Following an evaluation of these steels, Republic Steel Corporation's MA-60 was chosen as prime candidate for thin sheet truss cored panel assemblies (yield strength 65 ksi {448 MPa}) and Maxiform-80 for orthotropic panel construction [66]. Both steels conform to ASTM Specification A715, a high strength low alloy steel with improved formability with specifications listed in Table 3.6 below [67]:

TABLE 3.6

ASTM A715 HSLA TYPE 7 PROPERTIES

CARBON	0.15
MANGANESE	1.65
PHOSPHOROUS	0.025
SULFUR	0.035
NIOBIUM	0.005
SILICON	0.60
NITROGEN	0.020

	GRADE 60	**GRADE 70**
YIELD POINT KSI (MPa)	60(415)	70(485)
TENSILE STRENGTH KSI (MPa)	70(485)	80(550)
ELONGATION IN 2 INCHES (50 mm)	22	20

The thick section developmental task was much broader in scope in that it involved exploratory development of an HSLA steel for near term ship construction that was similar to HY 80. The task thus involved not only the identification of candidate steels from among current steel products but the study of derivative products with specific desirable strength and toughness properties. Specifically, the approach used was to:

(1) Survey domestic steel procedures.

(2) Procure and characterize candidate steels.

(3) Conduct weld process development.

(4) Select a primary candidate HSLA steel.

(5) Characterize the properties of the candidate steel.

(6) Characterize the properties of the candidate steel weldment.

(7) Conduct shipyard producibility studies.

(8) Conduct fragmentation and crack arrest evaluations.

The specific property requirements of 3/16 to 3/4 inch (4.76 to 19 mm) steel plate are listed in Table 3.7 below [49]:

TABLE 3.7

80 KSI (551.5 MPa) HSLA STEEL PLATE PROPERTIES

I. PLATE

YIELD STRENGTH (.2% offset): 80-99.5 KSI (552-686 MPa)
ELONGATION: 20 % MINIMUM IN 2 INCHES (50 mm)

CHARPY V-NOTCH TOUGHNESS (>1/2 INCH (12.7 mm) PLATE):

60 FT-LBS AT 0 DEGREES F (81.4 J AT -17.7 DEGREES C)
35 FT-LBS AT -120 DEGREES F (47.5 J AT -84.4 DEGREES C)

DYNAMIC TEAR TOUGHNESS:

450 FT-LBS AT -40 DEGREES F (610.2 J AT -40 DEGREES C)

II. WELD METAL

YIELD STRENGTH: 82-94 KSI (565.3-648 MPa)

CHARPY V-NOTCH TOUGHNESS (>1/2 INCH (12.7 mm) PLATE):

60 FT-LBS AT 0 DEGREES F (81.4 J AT -17.7 DEGREES C)
35 FT-LBS AT -60 DEGREES F (47.5 J AT -51.1 DEGREES C)

DYNAMIC TEAR TOUGHNESS:

425 FT-LBS AT 30 DEGREES F (576.3 J AT -1.1 DEGREES C)
300 FT-LBS AT -20 DEGREES F (407 J AT -28.8 DEGREES C)

Other requirements for the 80 ksi (551.5 MPa) HSLA steel included structural assessment, equivalence to HY 80 in fracture toughness and corrosion performance and weldability and process development.

The feasibility study was completed in 1983 and resulted in the selection of two candidate materials for extensive characterization. The candidate steel with the greatest potential for HY 80 comparability with minimum production and fabrication costs (as measured by the need to preheat welds for satisfactory joint properties) was ASTM A710 Grade A, the precipitation hardened copper steel originally developed by the International Nickel Company for arctic linepipe applications. It was further determined that the ASTM standard would have to be modified for Navy applications.

Studies conducted in 1982 and 1983 [51,68] estimated the cost savings for the use of HSLA in place of HY 80 and the weight reduction (and small cost penalty) for the use of HSLA in thinner sections in place of HTS. The results, summarized in Table 3.8, show that Navy shipbuilding costs could be reduced by 0.2 to 1.0 billion dollars per decade and that the weight of a cruiser or destroyer could be reduced by about 500 tons at a cost of under 2 million dollars. These obvious tangible benefits of HSLA research and development gave impetus to an acceleration of the certification process that led ultimately to its virtual completion in early 1984. HSLA has since been introduced to the fleet in new ship construction and has been designated for use in future design projects.

TABLE 3.8

PROJECTED USAGE, COST SAVING AND WEIGHT SAVING DATA FOR HSLA 80 STEEL BY SHIP TYPE

(UNITS IN LONG TONS WHERE 1 LT = 2240 LBS = 1000 Kg)

A. TYPICAL HY 80/HY 100 AND HTS USAGE (TONS) BY SHIP TYPE:

	HY 80	HY 100	HTS
CARRIERS	1496	21,527	22,370
CRUISERS	707	0-122	2,725-3,500
DESTROYERS	707	0	2,230-2,370
SUBMARINES	1,673-5,033	0	720-1,270

B. PROJECTED HY 80/ HY 100 AND HTS USAGE BY DECADE:

	HY 80	HY 100	HTS
1983-1993	188,700	96,100	570,000
1993-2003	159,800	92,400	620,000
TOTAL	348,500	188,500	1,190,000

C. COST SAVINGS FOR HSLA REPLACEMENT OF HY STEELS:

BASIS:	HY 80/HY 100 AS FABRICATED COST	$6-$7/LB
	HSLA BASE METAL SAVINGS	$.20-$.50/LB
	HY 80/HY 100 PREHEAT COSTS	$.20-$.40/LB
	NET HSLA COST DIFFERENCE	$.40-$.90/LB

CRUISER: $485,000-$1,090,000 PER SHIP IF ONE HALF HY 80 REPLACED

CARRIER: $9,200,000-$20,700,000 PER SHIP IF ONE HALF HY 80/HY 100 REPLACED

D. WEIGHT SAVINGS FOR HSLA REPLACEMENT OF HTS STEELS:

BASIS: NET WEIGHT REDUCTION 10-30 PERCENT HTS
NET COST PENALTY $.35/LB

CRUISER: 270-810 TON WEIGHT REDUCTION FOR $1,908,000

DESTROYER: 220-660 TON WEIGHT REDUCTION FOR $1,560,000

3.2.2 METALLURGY AND HEAT TREATMENT

As part of the certification process, the metallurgy of ASTM A710 was studied extensively, and the optimum heat treatment was developed for desirable metallurgical properties [69].The paramount importance of studying the effects of heat treatment on the mechanical properties of HSLA arises from the use of thermally induced microstructure changes to achieve the high strength and toughness of the product. The reduction of the grain size and the extent of precipitation hardening are both determined by the thermal history of the alloy system. Further, the weldability of HSLA is related to thermal effects in that welding is essentially a smaller scale version of the initial fabrication process. (i.e. the material in the region of the weld joint is subjected to thermal gradients analagous to those experienced during plate manufacture without the rigorous controls available on the steel mill production line).

The recommended heat treatment for ASTM A710 Grade A Class 3 steel is austenitization at 1650 degrees F (898.9 degrees C) for 68 minutes, water quenching, and aging at 1100 degrees F (593.3 degrees C) for 30 minutes followed by air cooling (the temperatures are mandatory while the times are at the discretion of the manufacturer). The "soaking" period at the austenitization temperature allows for a certain amount of copper to go into solid solution. When the steel is quenched, this copper remains in solution in a super-saturated condition and does not contribute appreciably to strength (which at this point is about 60 ksi (413.6 MPa)). Aging the steel at 1100 degrees F (593.3 degrees C) allows the copper to come out of solution as a precipitate to impede dislocation motion, thereby raising the yield strength to the 80 to 90 ksi (551.5-620.5 MPa) range. Niobium also contributes to the strengthening of the steel by inhibiting the growth of ferrite so as to produce very fine grains (approximately ASTM 10). As previously discussed, the use of precipitation hardening for strength reduces the dependence on carbon as a strengthening agent and hence allows for a more weldable product. Nickel is added to eliminate the hot shortness effects of copper and small amounts of chromium and molybdenum are added to preclude auto-aging (i.e. copper precipitation) after hot-rolling. The ASTM designation A710 also specifies requirements for a lower toughness Grade B steel without chromium and molybdenum and for a Grade A Class 1 steel which is aged in the as-rolled condition. A Grade A Class 2 steel is additionally specified which is aged after normalizing. Grade B heat treatment is the same as that for Grade A Class 1.

In order to determine the effects of heat treatment on ASTM A710, mechanical properties were measured after austenitization for as short as 30 minutes and for as long as 90 minutes at 1650 degrees F (898.9 degrees C) followed by aging at 900, 1000, 1100 and 1200 degrees F (482.2, 537.8, 593.3 and 648.9 degrees C) for 30,60 and 90 minutes [69]. It was determined that the time variations in both austenitizing and aging treatments had very little effect on mechanical properties. The aging temperature variations, on the other hand, indicated that low temperatures (900 degrees F {482.2 degrees C}) produced higher yield strengths at the expense of lower toughness and that high temperatures (1200 degrees F {648.9 degrees C}) caused a coarsening of the grains resulting in sharply lower flow stresses. The relatively benign variation in the strength and toughness properties of the HSLA steel with thermal transients was concluded to be of major importance in relation to its weldability, particularly since overaging would only increase the impact resistance.

The mechanical properties of ASTM A710 HSLA steel were determined by an extensive experimental evaluation of fifteen different commercially produced plates ranging in thickness from 3/16 to 1 1/4 inch (4.76 to 31.75 mm) including both Class 3 (quenched and aged) and Class 1 (as-rolled and aged) varieties [49]. Tension test results showed that all plates exceeded the 80 ksi (551.5 MPa) minimum strength requirements and that two plates exceeded the specified 99.5 ksi (686 MPa) maximum strength. Ductility requirements of 20 percent minimum elongation over a two inch (50 mm) gage length were met by all but one plate type. The impact toughness test results were far more revealing in terms of material characterization and selection in that three distinct groups were identified (see Figure 13). The Class 1 plates did not meet the Charpy V-notch (CVN) requirements of either 60 ft lbs at 0 degrees F (81.4 Joules at -17.7 degrees C) or 35 ft lbs at -120 degrees F (47.5 Joules at 84.4 degrees C). The Class

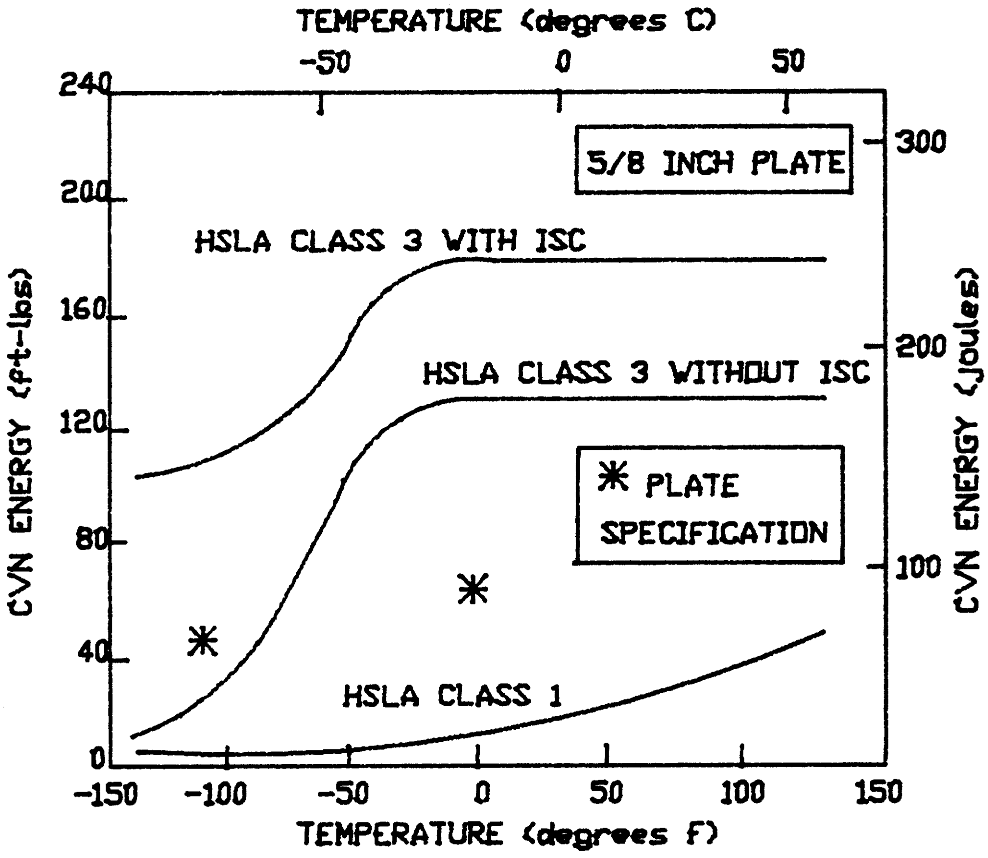

FIGURE 13 - Charpy V-Notch Impact Toughness Versus Test Temperature.

3 plates were found to have excellent toughness properties (CVN greater than 100 ft lb at -120 degrees F {135.6 Joules at -84.4 degrees C}) only if they had received inclusion shape control during fabrication. Inclusion shape control (ISC) refers to the addition of calcium to the melt during the steel making process to spheroidize sulfur inclusions and thereby mitigate their harmful effects on toughness (the irregular inclusion surfaces serving as crack initiation sites). The Class 3 plate without inclusion shape control was found to be within specification with one exception for a plate with sulfur concentration in excess of .010. Sulfur, a natural contaminant of the steel making process is limited to a maximum of .025 in the ASTM A710 classification. Based on these results, recommendations for a modification to the ASTM A710 designation were made for the fabrication of HSLA 80 for ship construction purposes:

(1) ASTM A710 Class 3 heat treatment.

(2) Inclusion Shape Control.

(3) Sulfur to be limited to a maximum of .010.

With the modifications prescribed above, ASTM A710 Class 3 steel was determined to meet all NAVSEA mechanical property requirements for ship construction over the thickness range evaluated.

3.2.3 WELDING AND FABRICATION

As the key selling point of the HSLA program, the economy of less stringent welding procedures in fabrication applications required extensive demonstration. HY 80 has been in widespread use by the Navy for more than twenty years with great success in high strength and high toughness applications. The inherent conservatism in design procedures, particularly where material applications are concerned, favors its continued use. In point of fact, however, HY 80 is expensive and if the same thing can be done cheaper it is worth the investigation. The expense of HY 80 stems primarily from its susceptibility to cold cracking or hydrogen cracking. This susceptibility is quantitatively expressed by its relatively high Carbon Equivalent Index (CE) of 0.40 due to high nickel and carbon concentrations. The result is that HY 80 must be preheated to keep the hydrogen out of the weld metal and the heat affected zone. The prescribed minimum preheat and interpass temperatures are 200 degrees F (93.3 degrees C) for thicknesses over 1.125 inches (28.6 mm), 125 degrees F (51.7 degrees C) for thicknesses between .5 inches (12.7 mm) and 1.125 inches (28.6 mm) and 60 degrees F (15.6 degrees C) below .5 inches (12.7 mm). In that maintaining this temperature is expensive (and in some applications physically difficult), the fact that HSLA with its CE of only .25 is not susceptible to hydrogen cracking makes it a viable alternative.

The certification program [70] investigated the welding of HSLA using the four processes expected to be used in production applications:

(1) Submerged arc welding (SAW) for flat position automated modular construction.
(2) Shielded metal arc welding (SMAW) for all position repair capability in difficult access areas.
(3) Gas metal arc welding (GMAW) for precision welding.
(4) Flux cored arc welding (FCAW) for all position welding capability with high deposition rates.

HY 80 welding consummables were specified due to their availability and proven performance (MIL-E-23765/2 Type 100S-1 for SAW and GMAW, MIL-E-11018 for SMAW and MIL-E-101TM for FCAW) [71]. The evaluation program was subdivided into four segments to meet all specification requirements:

(1) Weldability and weld repair were determined by indirect testing to compare HSLA to HY 80 (implant test to measure hydrogen cracking susceptibility and varestraint test to measure hot cracking resistance) and by direct testing to assess the fabricability of HSLA (keyhole test to assess root cracking, controlled thermal severity test to evaluate heat input effects, cruciform test to evaluate fillet and tee welds and the circular patch test to assess high restraint multiple pass welds).

(2) Weld process development was undertaken to determine the welding parameters and preheat temperatures needed to produce acceptable welds. The control variable for the production of acceptable weldments was the weld metal cooling rate.

(3) Dissimilar metal welding was evaluated by producing welds of HSLA and HTS and HY 80 and HY 100 so as to determine the metallurgical compatability of the resultant joint.

(4) Shipyard producibility was determined by performing a broad range of fabrication exercises in the shipyard environment.

The results of the certification program were as expected in that the weldability of HSLA was determined to be superior to HY 80 with comparable yield strength and toughness properties. The minimum required preheat temperature for welding HSLA in critical applications was found to be 60 degrees F (15.6 degrees C) while a minimum weld metal cooling rate of 10 degrees F per second at 1000 degrees F (5.6 degrees C per second at 537.8 degrees C) was measured. The required combination of welding heat input, plate thickness and preheat temperature to achieve this cooling rate are shown in Figure 14. This limit is necessary to assure adequate weld metal mechanical properties. Weldments of HSLA and HTS, HY 80 and HY 100 were all determined to be satisfactory when fabricated with the welding procedures as specified by the

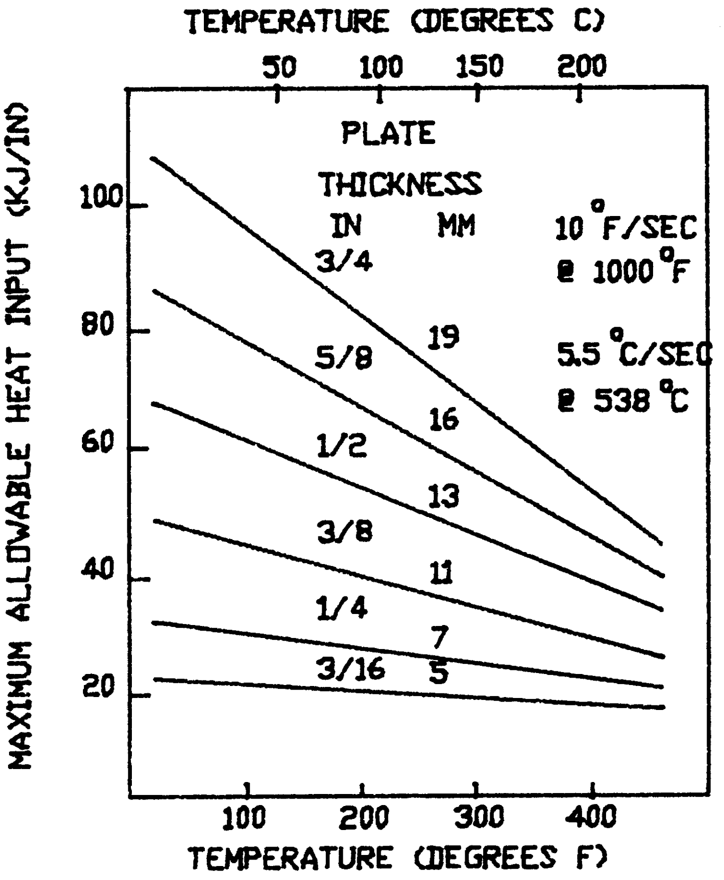

FIGURE 14 - Welding Conditions for Achieving Minimum Weld Cooling Rate.

more critical alloy. Production welds made at Ingalls Shipbuilding and Design in Pascagoula, Mississippi and at the Bath Iron Works in Bath, Maine were successful with reduced fabrication costs [72]. HSLA 80 hence met all program goals with regard to the ability to produce satisfactory metal joints at reduced expense.

3.2.4 CORROSION PERFORMANCE

In the field of Materials Science, quantitative measures of corrosion performance (with the possible exception of general corrosion) are perhaps the most empirical of all property measurements. Strength is accepted based on a standard tension test and toughness on the Charpy test but corrosion resistance must be based on actual "time in the water" experiments. Results typically consist of a simple yes or no answer based on whether the material exhibited degraded behavior when exposed to sea water. Unfortunately, extrapolation of data for long term applications is a relatively tenuous proposition, for if a material doesn't crack after one month's exposure one cannot say unequivocally that it won't crack after one year. Consequently, experiments are often long term propositions and intermediate results and "testing in progress" caveats prevail. In the case of HSLA 80, the requirement to demonstrate equivalence to HY 80 mitigates the experimental conundrum to the extent that side by side samples of each can be compared after reasonable intervals and parity established with some degree of certainty.

The certification program for HSLA 80 consisted of a demonstrate HY 80 equivalence for general corrosion, galvanic corrosion, crevice corrosion and stress corrosion cracking [72]. General corrosion or uniform attack is the most common form of corrosion, consisting of an electrochemical reaction which occurs over the entire surface exposed to the electrolyte. Although it represents the greatest material loss to corrosion of all the various modes possible, it is of limited technical concern as it can be readily measured and compensated for. For HSLA 80 certification, its general corrosion behavior was compared to six other materials when exposed to total seawater immersion, alternate wetting and drying and marine atmosphere for periods up to and including three years of which two years have been completed to date. Results confirmed that HSLA 80 general corrosion behavior was similar to other standard materials tested with rates of about 5 mils per year (127 microns per year) in both flowing seawater and partial immersion tests and 2 mils per year (50 microns per year) in the atmospheric tests. The maximum pit depth was also characterized as analagous to existing steel products in reaching a maximum of about 25 mils (635 microns) after one year with no significant growth with increased exposure.

Galvanic corrosion is the establishment of an electrochemical cell with two coupled dissimilar metals acting as the electrodes and an aqueous solution such as sea water acting as the electrolyte. Pure materials differ in their electronegativity from the noble gold to the reactive magnesium. Alloys of pure metals reflect their constituents to the extent that varying the relative amounts of the same materials changes the electronegativity of the resultant alloy. Thus, though HSLA 80 and HY 80 contain the same basic ingredients, they differ in their electronegativity. Galvanic corrosion tests of these two materials when electrically coupled indicated that HSLA 80 was mildly anodic to HY 80 since its corrosion rate increased from 5 mils per year (127 microns per year) to 9 mils per year (229 microns per year) whereas that of HY 80 decreased from 5 mils per year (127 microns per year) to 2 mils per year (50 microns per year). A galvanic couple between HSLA 80 and HTS, on the other hand, produced no preferential corrosion indicating electrochemical compatability.

Crevice corrosion is a geometrically induced anodic dissolution of material due to the presence of a restriction to the free flow of electrolyte. This restriction leads to a so-called differential aeration between the material within the crevice and that without as the oxygen within the crevice is depleted and cannot be replaced. When the oxygen is depleted, the dissolution of metal continues and an excess of positively charged metal ions builds up in the crevice. The positive charge attracts negative ions such as chloride which react with the metal ions to produce hydrochloric acid and metal salts. The resultant lowering of the PH (to the 2 to 3 range) accelerates the dissolution rate in the crevice causing rapid pitting. Testing of HSLA 80, performed by creating an artificial crevice with a plate mounted washer, indicated that it was not susceptible to crevice corrosion.

The mechanisms and theories of SCC have been addressed at some length in a previous section as they are the focus of this research. As discussed therein, susceptibility to SCC must be determined by experimentation with specific alloys in specific environments owing to the lack of a universal closed form mechanistic solution. To date, the evaluation of HSLA 80 SCC susceptibility has included the performance of bent beam tests, U-bend tests and precracked cantilever beam tests [49,72]. The bent beam tests consisted of loading 12 inch (30.5 cm) specimens to 75 to 90 percent of yield strength and placing them in a flowing seawater trough for a period of one year. Half of the specimens were cathodically protected by attached zincs. Inspection of the beams after the experimental period revealed that no cracking had occurred on any of the specimens. The U-bend tests were conducted in low velocity seawater, marine atmosphere, and sulfide bearing mud with electrochemical potentials of free corrosion, zinc cathodic protection and overprotection (hydrogen generation). The testing period was 3 years for base plate and 2 years for weldments. No detectable cracking has been observed. Cantilever beam specimens were precracked and loaded to varying values of stress intensity to determine that required for fracture (K_{ISCC}). The values reported are not valid in that specimen dimensions did not meet the plastic zone size requirement of ASTM procedure E399 (which would have required a specimen about 4 inches or about 10 centimeters thick). Since this experimental flaw is also true for for HY 80 (as it is generally true for all high toughness materials), comparability can be established. The reported values for K_{ISCC} were:

(1) 93-98 ksi$\sqrt{in}$ (102.2-107.7 MPa$\sqrt{m}$) for baseplate under cathodic protection in seawater (HY 80 K_{ISCC} is 100 ksi$\sqrt{in}$ {109.9 MPa$\sqrt{m}$}).

(2) 93-113 ksi$\sqrt{in}$ (102.2-124.2 MPa$\sqrt{m}$) for weld metal under cathodic protection in seawater.

(3) 95-102 ksi$\sqrt{in}$ (104.4-112.1 MPa$\sqrt{m}$) for the heat affected zone under cathodic protection in seawater.

The overall results of the SCC testing indicated that HSLA plates and weldments in thicknesses ranging from 3/16 to 1 1/4 inch (4.76 to 31.75 mm) were not susceptible to SCC and that their performance was comparable to HY 80.

3.2.5 CONCLUSIONS

Based on test results to date, one must conclude that HSLA 80 is an excellent candidate for ocean structure applications. It has the strength and toughness of HY 80 and the weldability and workability of HTS, thus providing a seeming panacea to the cost conscious production enterprise. The official recommendation for use of HSLA 80 in the construction of U. S. Navy ships was made in 1984 [49]. ASTM A710 Class 1 Steel was subsequently certified for use in thin section products (less than 5/16 inch {7.94 mm}) and ASTM A710 Class 3 was certified for thicker sections (up to 1 1/4 inches {31.75 mm}) with the following modifications:

(1) Sulfur content less than .010 percent (as opposed to .025 percent) to ensure adequate toughness.

(2) Inclusion shape control (ISC) required to spherodize the sulfur inclusions for adequate toughness at low temperatures.

The resultant steel product was further designated HSLA 80 to distinguish it from ASTM A710 as a low alloy steel for naval ship construction. Fabrication guidelines provided for the use of existing HTS welding procedures with certified HY 80 welding consummables. Satisfactory welding was predicated on maintaining a cooling rate of at least 10 degrees F per second at 1000 degrees F (5.6 degrees C per second at 537.8 degrees C).

HSLA 80 has since been designated for use in future naval surface ship construction. Although no new material can be fully proven until service use has been demonstrated, the extensive testing program conducted on thin section HSLA makes its future satisfactory performance highly likely. The susceptibility of HSLA to hydrogen embrittlement (HEM) has not been studied, however, and hence warrants further investigation. Future applications await testing of thick section HSLA 80 plate and development of a higher strength product with the same toughness and fabrication benefits. The experiments conducted in this research study were carried out on 2 inch (50 mm) thick sections of HSLA and hence should contribute to the certification of thick plate for military use. In addition, a detailed investigation of the effects of hydrogen on HSLA is included in the experimental program to be discussed in succeeding sections.

3.3 MECHANICAL PROPERTIES

Two inch thick steel plate was provided by David Taylor Naval Ship Research and Development Center (DTNSRDC), Annapolis, Maryland. The plate was manufactured by the Lukens Steel Company (heat number D6873) based on specifications for HSLA 80 provided by DTNSRDC. Chemical composition, heat treatment and mechanical properties were provided by the manufacturer and are listed in Table 3.9. Local testing was performed to certify the manufacturer's data and to gain some experience with HSLA for future experimental interpretation. The importance of microstructure to the behavior of a material when subjected to environmental testing mandated a relatively thorough microstructural evaluation. Specimens were extracted from a section of plate that was shipped prior to the completion of the welding for this purpose. All orientations within the as-received plate section were investigated to determine the homogeneity of the material. Through thickness variations in material properties were considered of particular significance due to the thickness of the plate. In addition to microstructural evaluation, tensile testing, hardness testing and Charpy impact testing were conducted.

TABLE 3.9

MANUFACTURER'S DATA
2 INCH (50 mm) HSLA 80 PLATE

I. COMPOSITION (WEIGHT PERCENT):

CARBON	0.06
MANGANESE	0.50
PHOSPHOROUS	0.013
SULFUR	0.004
COPPER	1.16
SILICON	0.28
CHROMIUM	0.75
NICKEL	0.88
MOLYBDENUM	0.21
NIOBIUM	0.039
ALUMINUM	0.03

II. MECHANICAL PROPERTIES:

.2% YIELD STRENGTH	87.9 KSI	(606 MPa)
UPPER YIELD POINT	89.9 KSI	(628 MPa)
ULTIMATE TENSILE STRENGTH	103.6 KSI	(723 MPa
REDUCTION OF AREA	74.0	PERCENT
ELONGATION	30.0	PERCENT

CHARPY ENERGY (AVERAGE OF 3 VALUES) IN FT-LBS (Joules):

	−120 °F	−50 °F	0 °F
TOP	46.7 (63.3)	128.0 (173.6)	226.7 (307.4)
BOTTOM	93.0 (126.1)	132.7 (180.0)	174.0 (236.0)

III. HEAT TREATMENT:

AUSTENITIZED AT 1650 °F (898.9 °C) FOR 60 MINUTES
WATER QUENCH
AGED AT 900 °F (482.2 °C) FOR 60 MINUTES
AIR COOLED

3.3.1 MICROSTRUCTURE

An orthogonal representation of the as-received plate is shown in Figure 15. The microstructure consists primarily of ferrite with small amounts of pearlite and bainite. The most noticeable feature of the microstructure is the small grain size (approximately .008 mm diameter grains corresponding to an ASTM grain size of 11). The prevention of grain growth during the aging process is attributed to niobium as previously discussed. The use of calcium to control the shape of the sulfur inclusions (ISC- Inclusion Shape Control) is also apparent from their spheroidal shape and the absence of any directional dependency.

The effects of welding are shown in Figure 16, where the three zones (weld metal, heat-affected zone and base metal) are clearly visible. The weld metal, shown individually at higher magnification in Figure 17, is characterized by a very fine grain structure associated with rapid solidification [73]. The heat-affected zone, shown in Figure 18, is comprised of bainite and martensite. This microstructure is caused by heating above the austenizing temperature followed by rapid quenching due to the cooling effect of the surrounding base plate. Grain growth is evident when comparison is made to the base metal photomicrograph (approximately .05 mm corresponding to an ASTM grain size of about 5.5).

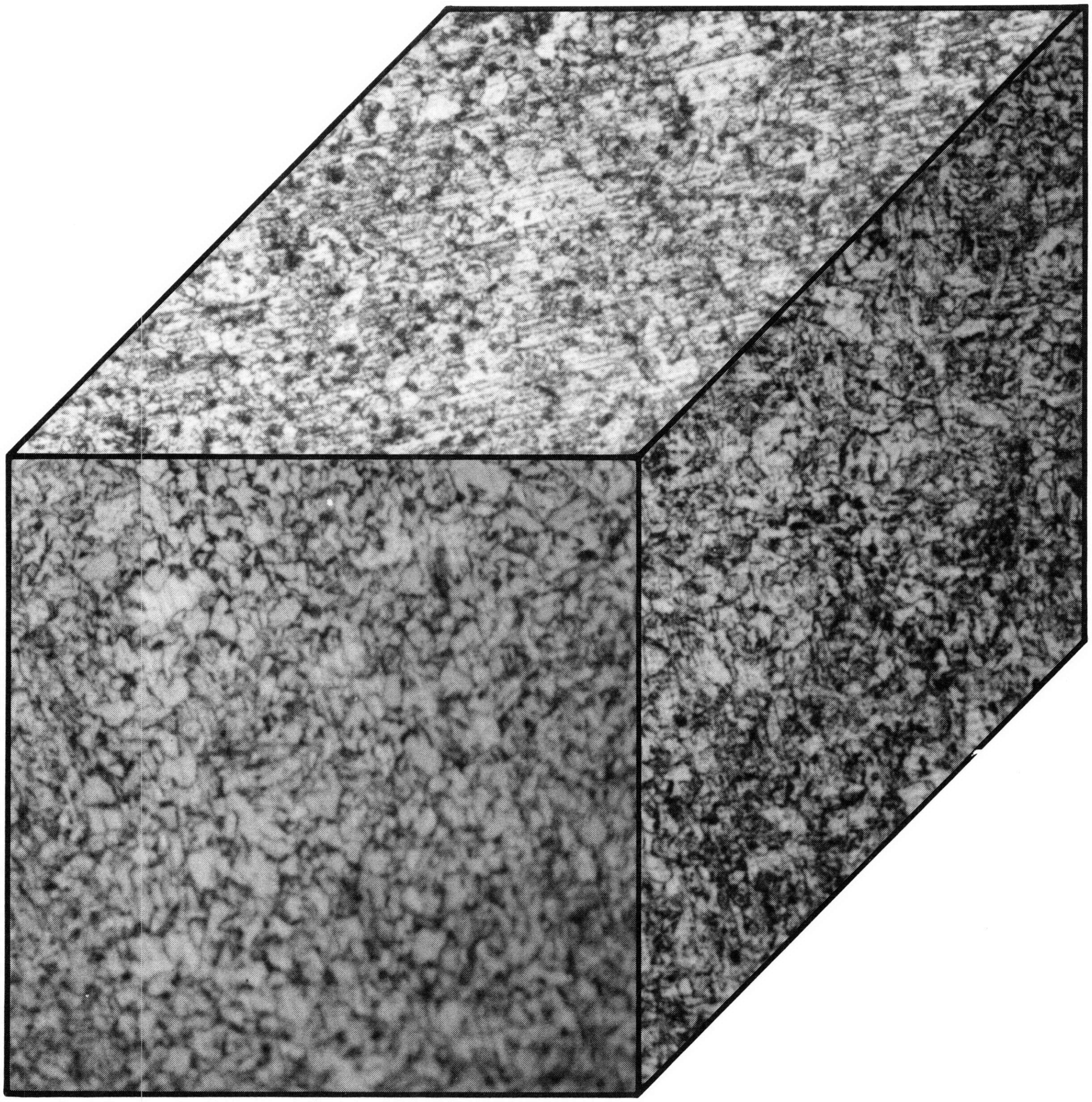

FIGURE 15 - Photomicrograph of As-Received Plate Showing Longitudinal, Transverse and Thickness Surfaces (500 X).

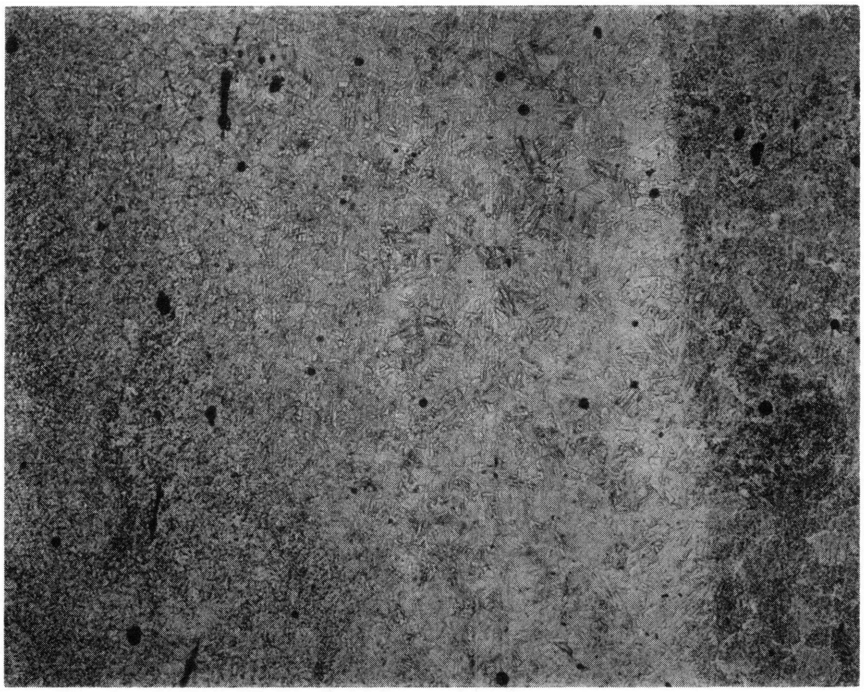

FIGURE 16 - Photomicrograph of Weld Region Showing Base Metal, Heat-Affected Zone and Weld Metal Grain Size Effects (100 X).

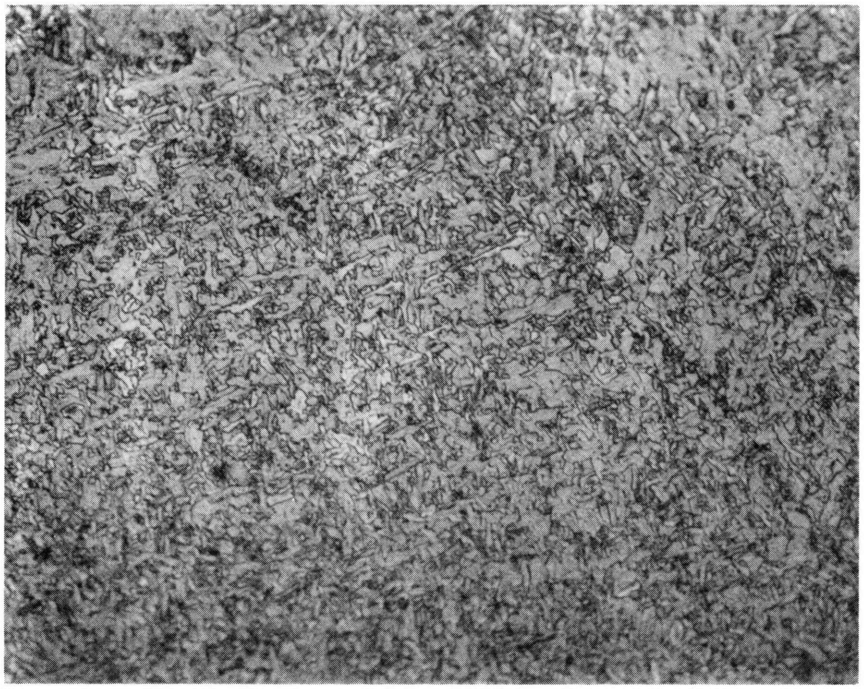

FIGURE 17 - Photomicrograph of Weld Metal Region (625 X).

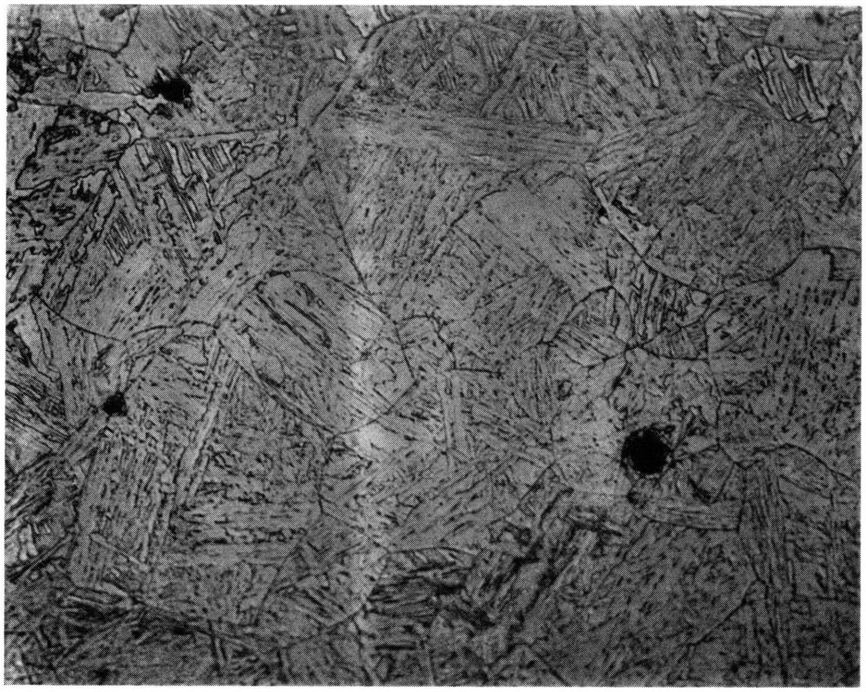

FIGURE 18 - Photomicrograph of Heat Affected Zone Region (625 X).

Further evidence of the effect of welding on the material is provided by hardness measurements taken in the three regions:

TABLE 3.10

KNOOP HARDNESS OF WELDED HSLA (AVERAGE OF 5 VALUES)

BASE METAL	134
WELD METAL	148
HEAT-AFFECTED ZONE	160

The higher hardness levels for the weld metal and the heat-affected zone are a direct result of the heat treatment inherent to the welding process. Yield strength scales directly with hardness since hardness measures the ability of a material to resist surface penetration and the surface is penetrated when a material yields locally (in fact, it can be shown that hardness is approximately three times yield strength [74]). Conversely, one would expect the toughness to degrade with increasing hardness [75]. Since these parameters were not explicitly measured in materials property testing, the correlation will be validated on analysis of stress strain data from the slow strain rate (SSR) testing portion of the experimental program.

Hardness measurements were also taken through the thickness of the plate to provide a measure of the homogeneity of the fabrication process. A standard Rockwell hardness tester with 1/16 inch ball was used for the B-scale measurements. The results are shown on Figure 19 and indicate a 9 percent difference in hardness readings between the minimum and maximum values. The random distribution of the hardness measurements indicate a negligible spacial dependence. The as-received plate may hence be considered essentially homogeneous in the thickness direction with respect to hardness and indirectly with respect to yield strength. This supports the observation of the microstrucure which did not display any directional dependency, as hardness is a microstructure sensitive property.

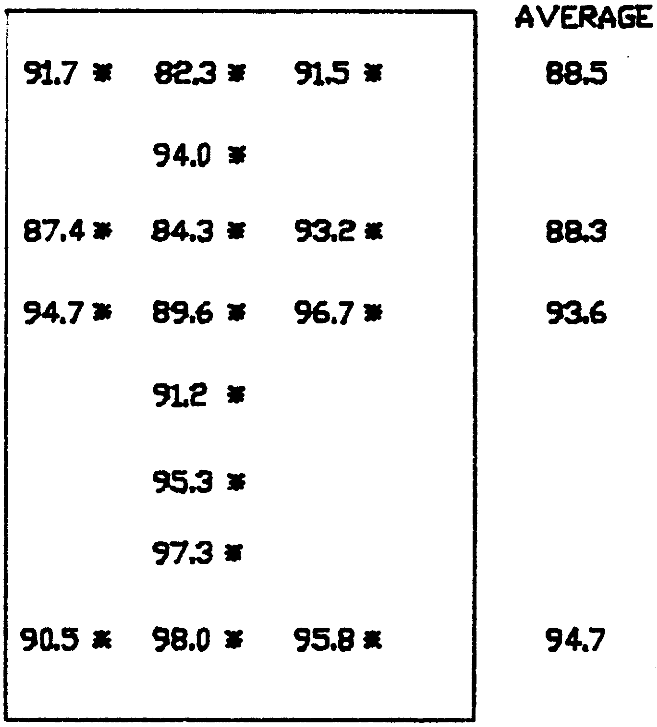

FIGURE 19 - Through Thickness Hardness Measurements (Rockwell B-Scale).

3.3.2 TENSILE TESTING

Tensile testing was performed on an Instron Universal Testing Machine Model TTC M1.6. Specimens were machined from base metal to the standard dimensions of ASTM E8 (1 inch {25.4 mm} gage length and 0.5 inch 12.7 mm} diameter). In order to assess the dependence of material properties on plate rolling direction, specimens were taken in the T-L and L-T configurations (i.e. in the rolling direction and perpendicular to it). Two tests were run for each type of specimen to provide backup data. The results are tabulated in Table 3.11 below:

TABLE 3.11

TENSILE DATA

	LT1	TL1	LT2	TL2
FINAL LENGTH in	1.31	1.27	1.19	1.21
(mm)	(33.3)	(32.3)	(30.2)	(30.7)
FINAL AREA sq. in	.007	.012	.012	.012
(sq. mm)	(4.52)	(7.74)	(7.74)	(7.74)
ELONGATION (%)	31.2	26.6	18.8	25.8
REDUCTION OF AREA (%)	85.9	75.0	75.0	75.0
0.2% YIELD STRENGTH ksi	93.7	105.3	88.6	87.4
(MPa)	(645.9)	(725.9)	(610.8)	(602.5)
ULTIMATE STRENGTH ksi	101.9	-	99.8	97.8
(MPa)	(702.5)		(688.0)	(674.2)

Yield points were observed to display an upper and lower yield value with a drop of about 2 ksi (13.8MPa). Comparison to the data of Table 3.9 provided by the manufacturer reveals a very close correlation in all material properties with the exception of elongation which was found to be lower than that reported (particularly for the LT2 specimen). Comparison of the LT data to the TL data indicates that material properties are not substantially affected by the rolling direction, as would be expected form the homogeneity of the microstructure.

3.3.3 CHARPY IMPACT TESTING

Charpy Impact Testing was conducted on a Tinius Olsen Testing Machine (Number 32828) rated at 264 foot-pounds (360 joules). Standard size specimens were prepared in accordance with ASTM Standard Method E23-82 "Notched Bar Impact Testing of Metallic Materials" in the LT (parallel to rolling direction), TL (transverse to rolling direction) and SL (through the thickness) orientations. Two tests of each specimen type were conducted at 0 degrees F (-17.7 degrees C) and -60 degrees F (-51.1 degrees C) to provide data for comparison to manufacturer's data (Table 3.8) and to reference 49 data as shown in Table 3.11 below:

TABLE 3.11

CHARPY IMPACT TEST DATA
FT-LBS (JOULES)

	TEMPERATURE degrees F (C)	LT	TL	SL
1. CURRENT TESTING	0(-17.7)	114(155)	148(201)	86(117)
(AVG OF 2 VAL)	-60(-51.1)	150(203)	151(205)	25(34)
2. REFERENCE 49 DATA	0(-17.7)	199(270)	187(254)	-
(1 1/4 IN PLATE)	-60(-51.1)	202(274)	164(222)	-

		LT (TOP)	LT (BOTTOM)
3. MANUFACTURER'S	0(-17.7)	226.7(307)	174.0(236)
DATA	-50(-45.6)	128.0(174)	132.7(180)

The specification for HSLA 80 (Table 3.6) of 60 ft-lbs (81.4 joules) at 0 degrees F (-17.7 degrees C) was met in all tests indicating satisfactory performance at this temperature. The requirement of 35 ft-lbs (47.5 joules) at -120 degrees F (-84.4 degrees C) was not measured explicitly but the data at -60 degrees F (-51.1 degrees C) for the LT and TL orientations suggest satisfactory compliance with the lower temperature specification.

The poor correlation between the three sets of measured impact energy data is indicative of variation of toughness properties through the thickness of the 2 inch (50 mm) plate. The manufacturer's data were obtained from specimens removed from the top and bottom of the plate where heat treatment is more effective in achieving greater toughness. The specimens used for this testing were removed from the plate about one half inch (13.7 mm) from the surface where heat treatment is less effective resulting in some toughness degradation. The reference 49 data were for a thinner and hence more homogeneous plate.

Further evidence of through thickness variation of toughness properties is provided by the SL test data. The low impact energies obtained for these orientations indicate that the center of the plate is much more brittle than the top or the bottom. This again is directly attributable to the difficulty in obtaining homogeneity in the processing of thick plate. Although there is no specification for SL impact energies, the low toughness of the center of the plate merits further investigation. Since this research is concerned primarily with the corrosion properties of HSLA 80, the need for further characterization of plate toughness variations through the thickness must be left as a recommendation for future work (Section 9).

4. MOTIVATION AND OBJECTIVES OF EXPERIMENTAL RESEARCH

The susceptibility of a specific material to stress corrosion cracking and/or hydrogen embrittlement in a specific environment cannot be predicted on the basis of current theory. Rather, such an assessment must be based on experimental data from conditions that duplicate anticipated service use to the maximum extent practicable. Thus, in the case of SCC and HEM, empirical results form the foundation for engineering recommendations in lieu of providing only a backup to theoretical analyses. The paramount importance of experiment motivates a thorough research effort.

HSLA steels have demonstrated great potential in ship construction by reducing fabrication costs and by reducing structural weight requirements. To date, only thin section (less than 1 1/4 inches {31.75 mm}) products have been fully evaluated and approved for service use. Future applications await the results of experiments with thick section (2 inch {50 mm}) plating. In the fiscally constrained environment of warship design and construction, the availability of a cheaper yet equally capable product means more ships for less dollars. The potential for an enhanced defense posture motivates a timely and accurate assessment of the SCC and HEM properties of thick section HSLA steels.

The objectives of this research effort are as follows:

(1) To evaluate the susceptibility of thick section HSLA 80 to stress corrosion cracking.

(2) To evaluate the susceptibility of thick section HSLA 80 to hydrogen embrittlement.

(3) To evaluate the effects of submerged arc welding (SAW) and gas metal arc welding (GMA) on the SCC and HEM performance of HSLA 80.

(4) To measure the critical stress intensity for the initiation of stress corrosion cracking (K_{ISCC}) for the base metal, weld metal and the heat-affected zone (HAZ) of the two weld processes.

(5) To determine if cathodically generated hydrogen affects the critical stress intensity to the extent that definition of a separate critical stress intensity for hydrogen embrittlement (K_{IHEM}) is justified.

(6) To reach a conclusion as to the future use of thick section HSLA 80 in marine hull structure applications.

To meet these objectives, the experimental program described in the next section was developed. In essence, the program provides qualitative and quantitative measures of HSLA 80 base metal, weld metal and heat-affected zone susceptibility to stress corrosion cracking and hydrogen embrittlement in a seawater environment.

5. PROCEDURES AND APPARATUS FOR EXPERIMENTAL RESEARCH

5.1 OVERVIEW

The overall experimental program is outlined in Table 5.1. Two sets of experiments were conducted. The Wedge-Opening Load (WOL) experiment was selected to provide quantitative measures of crack growth rate and stress intensity. The fundamental advantage of the WOL test over the more traditional cantilever beam test is that each individual WOL specimen provides a quantitative stress intensity at which the crack arrests. The cantilever beam test, on the other hand, provides only a data point (i.e. it either breaks or it does not break) at a prescribed stress intensity. Consequently, the WOL experiment is more thorough (for a given number of specimens) in that data correlation and analysis between specimens is possible. The Slow Strain Rate (SSR) experiment was selected primarily for qualitative assessment of fracture appearance (i.e. brittle or ductile failure), although quantitative data such as time of failure (TOF) and reduction of area (ROA) were also measured to further characterize material behavior.

Synthetic seawater was prepared in accordance with ASTM D1141-75 for the experimental environment. This selection was made to ensure reproducibility of experimental results at other laboratory facilities and to provide a known homogeneous solution for direct data comparison and correlation. Further, the use of flowing natural seawater was considered inappropriate due to the inherent seasonal and geographic

TABLE 5.1

EXPERIMENTAL PROGRAM MATRIX

1. WEDGE-OPENING LOADING (WOL) TESTING

MATERIAL	FREE CORROSION	-1000 MV SCE	-1250 MV SCE
BASE METAL	A,B	A,B	A,B,C
GMA WELD	A,B,C	A,B,C	A,B,C
GMA HAZ	A,B,C	A,B,C	A,B,C
SAW WELD	A,B,C	A,B,C	A,B,C
SAW HAZ	A,B,C	A,B,C	B,C

PRIMARY VARIABLE: STRESS INTENSITY $Ksi\sqrt{In}$ $(MPa\sqrt{m})$

A = 90 (98.9)

B = 100 (109.9)

C = 110 (120.9)

TOTAL SPECIMENS: 42

2. SLOW STRAIN RATE (SSR) TESTING

MATERIAL	FREE CORROSION	-1000 MV SCE	-1250 MV SCE
BASE METAL	A,B	A,B	A,B
GMA WELD	A,B	A,B	A,B
GMA HAZ	A,B	A,B	A,B
SAW WELD	A,B	A,B	A,B
SAW HAZ	A,B,C	A,B,D	A,B,D

PRIMARY VARIABLE: STRAIN RATE in/in/sec OR mm/mm/sec

$A = 6.67 \times 10^{-5}$

$B = 8.33 \times 10^{-6}$

$C = 1.67 \times 10^{-4}$

$D = 8.33 \times 10^{-7}$

TOTAL SPECIMENS = 32

variability of littoral sources and the lack of availability of a homogeneous deep water source. Experimental time constraints precluded specimen submission to a dedicated seawater test facility. Finally, a recent study conducted by DTNSRDC [76] concluded that K_{ISCC} measurements were essentially invariant whether testing was conducted in natural seawater, synthetic seawater or thirty day old seawater.

Three corrosion potentials were chosen in order to characterize the behavior of HSLA in three specific field environments:

(1) FREE CORROSION - Specimens were immersed in synthetic sea water with no potential control to provide baseline data. This condition represents that of unprotected hull plating or structural members subjected to continuous seawater immersion. Such would be the case for an area of the hull distant from protective sacrificial anodes from which the protective paint coating had been removed or improperly applied. The free corrosion potential of HSLA base metal was measured as approximately -435 millivolts with reference to a saturated calumel electrode (SCE). This corresponds to -220 millivolts when referenced to a standard hydrogen electrode (SHE). A weld metal specimen was additionally measured and found to have essentially the same free corrosion potential.

(2) **ZINC-COUPLED** - Specimens were immersed in synthetic seawater with an applied cathodic potential of -1000 millivolts SCE. This corresponds to -720 millivolts SHE and -950 millivolts when referenced to a saturated Ag/AgCl electrode. This condition is that of HSLA plate protected by sacrificial anodes (usually zinc) or by the direct application of a potential from an electrical source for cathodic protection. In that the potential of zinc-coupled HSLA varies with material and environmental conditions (such as when a film forms on the specimen surface), experimental measurement was compared to both analytical calculation and to the potential used in related corrosion experimentation to arrive at the chosen value of -1000 mv SCE.

(a) **Direct Corrosion Cell Measurement** - A zinc specimen was electrically coupled to an HSLA specimen and immersed in a beaker filled with synthetic seawater. The potential was measured with a digital voltmeter and recorded over a five minute period. The initial potential was -1030 mv SCE and the final potential was -1050 mv SCE. A weld metal sample yielded similar results when coupled to the zinc specimen. The validity of the direct corrosion potential measurements was determined by measuring the potential of a single zinc electrode and of a single HSLA electrode and comparing them to published results [77]. The measured potential for zinc was −1065 mv SCE compared to the published value of −1030 mv SCE and the measured potential of HSLA was −435 mv SCE compared to the published value of −610 mv SCE for carbon steel and −530 mv SCE for Type 304 Stainless Steel. The differences between the measured and published results are not significant since slightly different environments (e.g. natural seawater versus synthetic seawater) or differences in sample surfaces (e.g. freshly machined surface versus filmed surface) could readily account for the deviation.

(b) Analytical Derivation – The Tafel equations and basic corrosion kinetics were used to approximate the zinc-coupled potential for HSLA. Assuming exchange current densities (I_o) of 10^{-7} amps/cm^2 for hydrogen forming on zinc and 10^{-6} amps/cm^2 for hydrogen forming on iron and an equilibrium zinc ion activity of 10^{-6} [78], one may compute relationships for the anodic overpotential (N_a) and the cathodic overpotential (N_c) as follows:

$$N_a = E_{corr} - E_{zn} = .059\log(i_{corr}) - .059\log(i_{o\,zn})$$

$$N_c = E_{corr} - E_h = .118\log(i_{o\,h}) - .118\log(i_{corr})$$

Solving these two equations simultaneously for corrosion current (i_{corr}) and corrosion potential (E_{corr}) yields:

$$i_{corr} = .2 \text{ ma/cm}^2$$

$$E_{corr} = -744 \text{ mv [SHE]}$$

This corrosion potential corresponds to -1020 mv SCE.

(c) Related Experimental Literature - Corrosion experiments with HSLA reported in reference 49 used potentials of -850 and -1000 millivolts referenced to Ag/AgCl which corresponds to about -1050 mv SCE. Corrosion experiments with HY 130 reported in reference 3 used -1000 millivolts referenced to Ag/AgCl.

In actual field applications, the potential of a zinc-coupled HSLA plate would vary locally due to seawater compostional, PH and temperature gradients, local variance in plate and zinc composition and the geometry of the galvanic couple. The final rounded value of -1000 mv SCE was chosen as a representative cathodic potential that could be readily set and maintained on available laboratory instruments.

(3) HYDROGEN GENERATING - Specimens were immersed in synthetic seawater with an applied cathodic potential of between -1250 and -1300 mv SCE. The experimental objective of this environment was to generate sufficient hydrogen to evaluate the susceptibility of HSLA to hydrogen embrittlement. In field applications such a situation could arise on systems cathodically protected by an externally applied voltage which had been improperly set or allowed to drift to an overvoltage situation. The potential presence of monatomic hydrogen must be assumed as possible in any field application, however, as it can be introduced to the environment from a wide variety of sources (e.g. battery charging or the electrolytic production of oxygen from water). The cathodic potential at which hydrogen evolution occurred was determined by conducting a polarization experiment. An HSLA sample was spot welded to an Inconel Alloy 600 wire and encased in a 7/8 inch diameter epoxy mold (Bueheler Sampl-Kwick Acrylic no. 20-3560). The one square centimeter exposed face of the sample was then polished and the edges sealed with Tolbert Micro-Super 2000 protective lacquer. The attached wire was encased in glass tubing which was sealed against the environment at the back of the epoxy mold. The encased sample with the single exposed face was immersed in an environment of synthetic seawater to serve as the working electrode of an electrochemical cell referenced to a saturated calumel electrode. The system was subsequently connected to an

Aardvark Model V-2LR Potentiostat with a Model Scan-4 Scanning Unit. The potential was varied at a rate of 35.7 mv/sec from an initial value of -600 mv SCE to a final value of -2000 mv SCE and the current recorded to produce the polarization diagram shown in Figure 20. The surface of the sample was visually inspected during the experiment to detect the onset of hydrogen generation. This was found to occur at approximately -1250 mv SCE at a current of about 8 milliamps. At -1300 mv SCE and 10 milliamps, hydrogen generation was fully developed and blanketed the surface of the specimen. The hydrogen generation potential was hence chosen as between -1250 mv SCE and -1300 mv SCE to be adjusted as necessary to achieve visible but not excessive hydrogen generation.

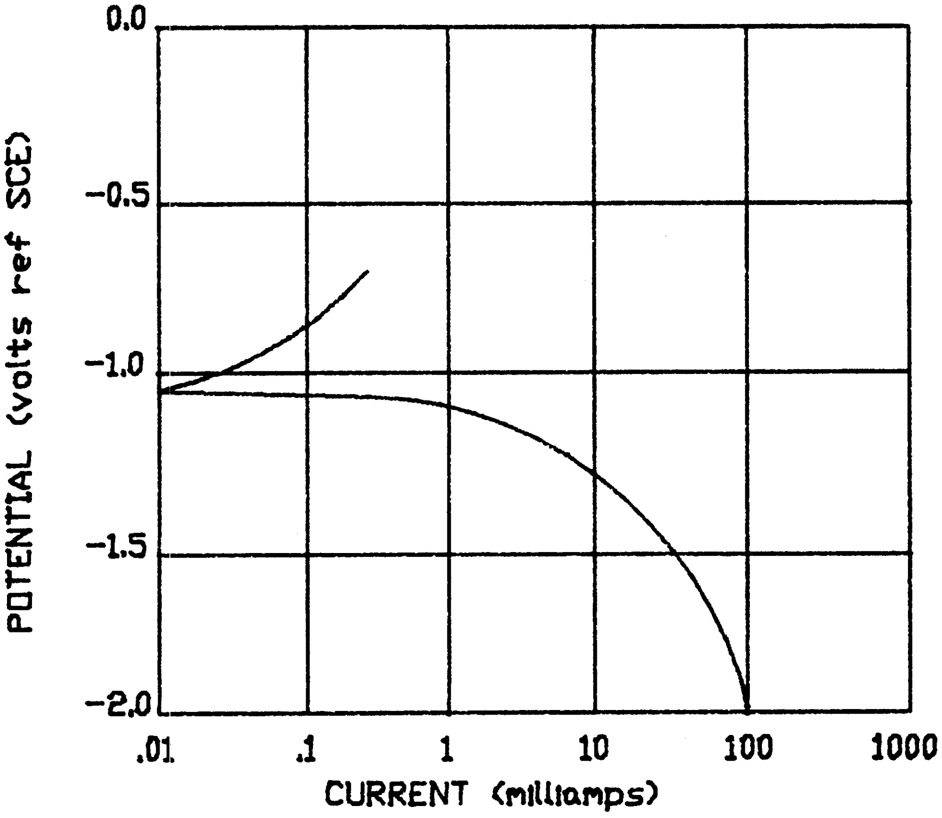

FIGURE 20 - Polarization Diagram
of HSLA Steel at 35.7 mv/sec.

5.2 WELDING OF HSLA PLATE

Welding was performed at David Taylor Naval Ship Research and Development Center (DTNSRDC), Annapolis between 12 and 14 August, 1985. Two weld processes were chosen for evaluation; submerged arc welding (SAW) due to its wide use in large scale production welding jobs (such as ship hull plate) and gas metal arc welding (GMA) as a representative of the inert gas processes used for smaller, more detailed welding jobs (such as ship frame welds). The six foot long, two inch thick as received plate was cut into four six inch wide sections to form the two flat weld joints (one for SAW and one for GMA). The weld joints were further cut into a "K" configuration weld prep as shown in Figure 21. This configuration was chosen in favor of the more typical "double-V" weld prep in order to provide a flat surface with a relatively homogeneous heat-affected zone to facilitate subsequent specimen preparation. Photomicrographs of macroscopic cross sections of the completed weldments are shown in Figure 22.

Specific welding parameters as delineated in the following sections for the two processes were chosen [79] to provide a cooling rate of greater than 10 degrees F per second at 1,000 degrees F (5.5 degrees C per second at 538 degrees C) in order to ensure adequate yield strength and toughness as recommended by DTNSRDC [49]. The use of empirical weld parameter specifications is virtually universal as the thermal effects of welding on the heat-affected zone are very complex and analytical results do not adequately predict field

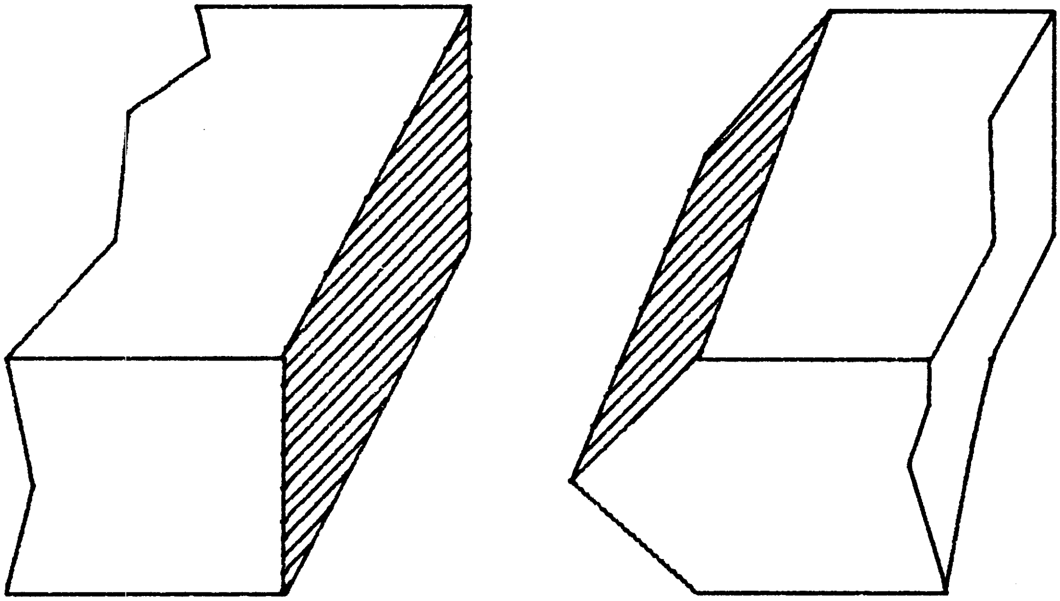

FIGURE 21 - Weld End Preparation Showing "K" Configuration.

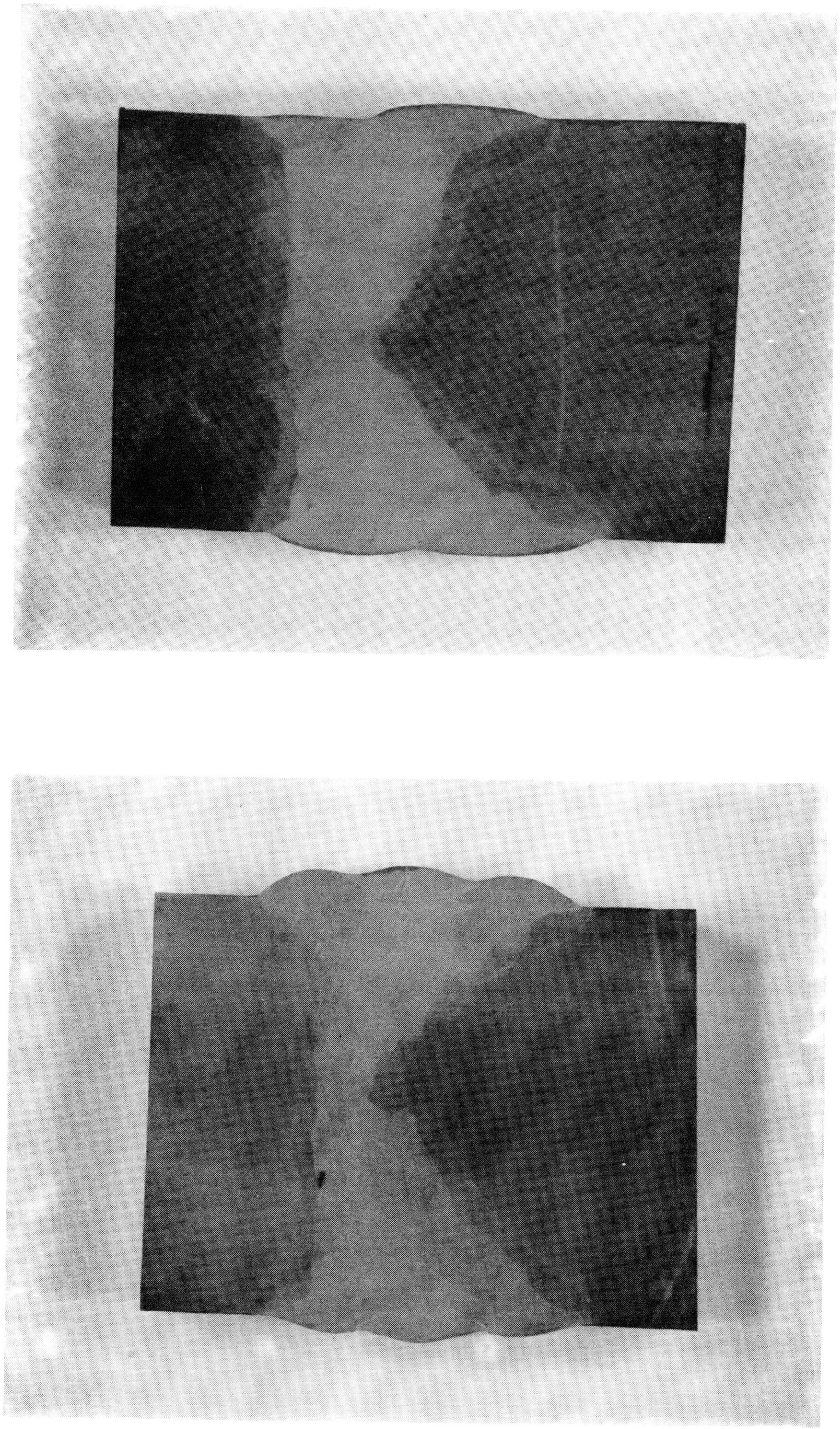

FIGURE 22 - Macroscopic Etched Surfaces of Gas Metal Arc (GMAW) and Submerged Arc (SAW) Welds.

experience [46]. The cooling rate of the heat-affected zone is generally used as the key parameter in determining its post-weld mechanical properties. The cooling rate is in turn dependent on various factors including plate thickness, welding conditions (voltage, current, heat input and gas composition), preheat, weld length and joint geometry. Too high a cooling rate creates hard, brittle martensite which could lead to cracking and too low a cooling rate results in overaging of the heat-affected zone with a concomitant reduction in the toughness and the yield strength.

Predicting the cooling rate from the welding parameters is largely speculative, although empirical results have been published. Kihara et al [80] proposed a relationship to relate cooling rate to its determinant parameters as follows:

$$P = \left(\frac{T - To}{I/v} \right)^{1.7} * \left(1 + \frac{2}{pi} \text{ARCTAN}\left(\frac{t - to}{alpha} \right) \right)$$

$$\text{COOLING RATE (degrees C/sec)} = 0.35 * (P)^{0.8}$$

where T = Temperature at which cooling rate is is considered (degrees C)

To = Preheat temperature (degrees C)

I = Weld current (amps)

v = Travel speed (inches/min)

t = Plate thickness (inches)

to = .56 at 540 degrees C

alpha = .16 at 540 degrees C

For the weld parameters chosen to make the subject GMA and SAW joints, this formula yields cooling rates of 22.4 degrees C/sec and 21.5 degrees C/sec respectively which meet the required criteria.

A more common and practical method of relating cooling rate to its major relevant independent variables is to construct a family of curves for different plate thicknesses and a series of heat inputs. The cooling rate for each condition may be measured with thermocouples or predicted with empirical formulas (as above) or by a combination of the two. Heat input (h) is the predominant process variable since it relates voltage (V) in volts, current (i) in amperes and travel speed (v) in inches per minute according to [46]:

$$h = 60 \ (Vi/v)$$

These curves may then be used to define a functional operation envelope (FOE) which specifies the range over which acceptable welding conditions exist. It then remains to be determined experimentally where within the FOE welding must be conducted to produce a weld with adequate mechanical properties. Such a procedure was carried out by DTNSRDC [49] for HSLA plate with a preheat temperature of 125 degrees F (51.7 degrees C) and a maximmum plate thickness of 3/4 inch (19 mm). The GMA result, shown in Figure 23 yields an extrapolated cooling rate of about 40 ^{o}F/sec (22.2 ^{o}C/sec) for a 2 inch (50 mm) thick weld

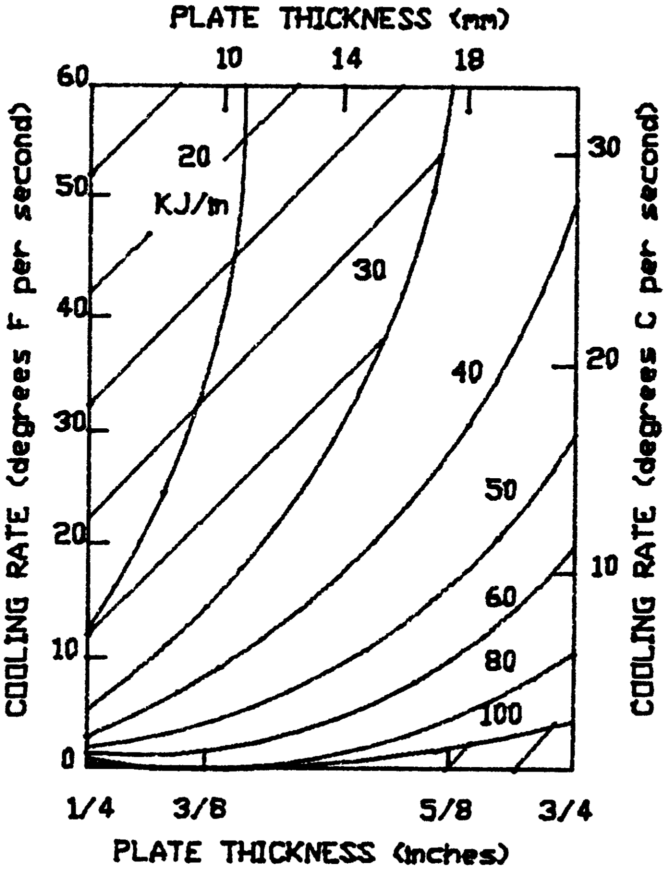

(Hatched Area Indicates Unsatisfactory Weld)

FIGURE 23 - Functional Operating Envelope (FOE) for Gas Metal Arc Welding (GMAW).

made with 60 KJ/inch heat input specified for this research study. This compares favorably with the empirical result of Kihara calculated above.

Weld preheat and interpass temperature limits were imposed at 200 degrees F (93.3 degrees C) minimum and 300 degrees F (148.9 degrees C) maximum respectively for both weld processes. Weld preheat is normally incorporated into weld procedures in order to eliminate the possibility of hydrogen induced cold cracking as discussed in Section 2.4. One of the primary advantages of HSLA, however, is its apparent immunity to cold cracking making it an economically cheaper production process since it requires no preheat. The specification of a preheat temperature in this instance was based on eliminating any possible hydrogen effects since the weldability of HSLA was not an issue in this study, having been previously demonstrated [49]. The maximum interpass temperature specification, on the other hand, was required to ensure an adequate cooling rate for each weld pass. Clearly, if the weld region is not allowed to cool down between passes, there would be an insufficient temperature differential to cause cooling according to heat transfer principles.

Following welding, each plate was radiographed along its entire length to check for slag inclusions, porosity or delamination. No significant defects were noted. The plates were subsequently shipped to MIT for specimen preparation.

5.2.1 GAS METAL ARC (GMA) WELDING

Gas metal arc (GMA) welding is one of several weld processes that use an externally supplied gas shielding to protect the weld from the oxygen and nitrogen in the atmosphere, which, when allowed to enter the weld, cause porosity. The heat for welding is obtained from an electric arc drawn between the metal electrode and the workpiece. The GMA process was developed in 1948 from the gas tungsten arc (GTA) process in order to increase the welding speed and thereby increase productivity [81]. The GTA process is characterized by a nonconsummable tungsten electrode which generates the arc. Additional material needed to fill the weld joint gap (known as filler metal) must be added separately to the "weld puddle" as the workpiece is traversed. GMA welding, on the other hand, combines the functions of the electrode and the filler metal into a single moving filament of metal which is called a consummable electrode. This simplification, which results in greater efficiency of heat input, allows the welder to traverse the workpiece more rapidly, up to about four times the weld deposition rate of GTA welding. The GMA process has hence come into wide use in many industrial applications.

The selection of shielding gas for use when welding with the GMA process depends on the type and thickness of material to be welded, the joint configuration and economic factors such as speed and quality requirements. For welding carbon steels, an argon-oxygen mixture is normally recommended.

Since the inert gas is used to shield the weld area from the harmful effects of the atmosphere, it may seem counterproductive to add oxygen to the gas. It has been found, however, that a small amount of oxygen greatly improves the arcing characteristics without adversely affecting the weld's mechanical properties.

GMA welding is normally performed with the electrode positive and the workpiece negative, a configuration known as direct current reverse polarity (dcrp). This is the opposite of GTA welding, which uses direct current straight polarity (dcsp). The effect of the dcrp electrical connection for GMA welding is that the positive gas ions are accelerated from the electrode to the workpiece by the action of the electrical field. It is postulated [81] that these ions impart their velocity to the metal drops as they move from the electrode to the workpiece. The result is a deeply penetrating weld which improves the strength of the joint.

GMA welding for this application was performed using an Airco Direct Current Aircomatic Dual 600 Ampere Welder (model number 6DVR-24-CPA) with automatic wire feed and carriage movement provided by a Union Carbide J Governor. Filler wire was 0.062 inch Linde 95 (heat number 095074), an approved HY 80 consummable as recommended by reference 49. Welding parameters were monitored continuously during each of the 25 passes to verify conformance to the established specifications listed in Table 5.2.

TABLE 5.2

GAS METAL ARC WELD PARAMETERS

VOLTAGE	32 VOLTS
CURRENT	340 AMPERES
TRAVEL SPEED	11 INCHES/MINUTE
HEAT INPUT	60 KILOJOULES/INCH
SHIELD GAS	98% ARGON/2% OXYGEN
GAS FLOW RATE	50 CUBIC FEET/HOUR
ELECTRICAL	DIRECT CURRENT REVERSE POLARITY

5.2.2 SUBMERGED ARC WELDING (SAW)

Submerged arc welding is similar to GMA welding in the use of a continuously fed electrode that serves as both the filler metal and the heat source. The difference between the two processes rests with the method employed to shield the work area from the environment. As the name implies, SAW employs a shielding blanket of granular, fusible material called flux which "submerges" the arc. It produces high quality, low cost welds on carbon steel plate and is hence widely used for large production jobs.

The flux is the key element of the SAW process as it serves to concentrate heat to enhance melting and fusion and to provide a conductive path from the electrode to the workpiece in addition to shielding the weld area from the atmosphere. At room temperature, flux is a granular non-conductor of electricity. When the arc is struck between the electrode and the workpiece, the flux in the immediate vicinity of the weld becomes a highly conductive molten medium. Since the remainder of the flux surrounding the joint retains its granular insulating properties, the heat generated by the arc in the weld region is concentrated and hence exceptionally intense. Under these conditions the base metal is readily melted so that smaller weld prep "V" grooves may be used and less filler metal supplied. In addition, high welding speeds may be used without sacrificing quality making the process extremely economical in comparison to both GMA and GTA welding. Since the flux solidifies at a lower temperature than the molten metal, it forms a hard crust on top of the weld that can readily be removed at the conclusion of each pass.

Although both alternating and direct current power supplies may be used for SAW, direct current is generally preferred since it provides better control of weld bead shape, weld penetration and welding speed [81]. This is especially true when close arc control is needed as in the case where contours must be followed at maximum speed. Alternating current is generally preferred for higher current applications.

SAW for this application was performed with a Union Carbide Linde VCR-801 CV/DC Welder with automatic wire feed provided by a UCC-8 controller. Filler wire was .062 inch Linde 95, the same as that used for the GMA weld. The flux was Oerlikon OP121TT (lot number 1033). The welding parameters are listed in Table 5.3.

TABLE 5.3

SUBMERGED ARC WELD PARAMETERS

VOLTAGE	31 VOLTS
CURRENT	350 AMPERES
TRAVEL SPEED	11 INCHES/MINUTE
HEAT INPUT	60 KILOJOULES/INCH
ELECTRICAL	DIRECT CURRENT

5.3 WEDGE-OPENING LOAD (WOL) TESTING

5.3.1 BACKGROUND

Wedge-opening load (WOL) testing using a bolted specimen was developed by Novak and Rolfe [82] from the original machine loaded WOL specimen developed by Manjoine [83] in order to provide a simple and self-contained specimen load geometry for the evaluation of stress corrosion cracking and hydrogen embrittlement. Prior to this development, the cracking susceptibility of a material with a preexisting flaw was determined by the cantilever beam test developed by Brown [84]. In the cantilever beam test, a series of precracked beams are subjected to different constant loads so as to produce stress intensity levels below the critical stress intensity in air (K_{IC}). Once loaded, the beams are exposed to the environment for which SCC or HEM susceptibility is to be determined and the time to failure recorded. A graph of stress intensity versus time to failure similar to Figure 24 is prepared and the value of K_{ISCC} determined as that stress intensity below which time to failure approaches infinity. Although this method is effective in measuring K_{ISCC}, it requires a large number of specimens for which the fabrication, material and the environment must be stictly controlled to prevent inadvertent differences from introducing data inaccuracies. Additionally, exposure to the environment may be quite difficult, particularly for high temperature and/or pressure applications.

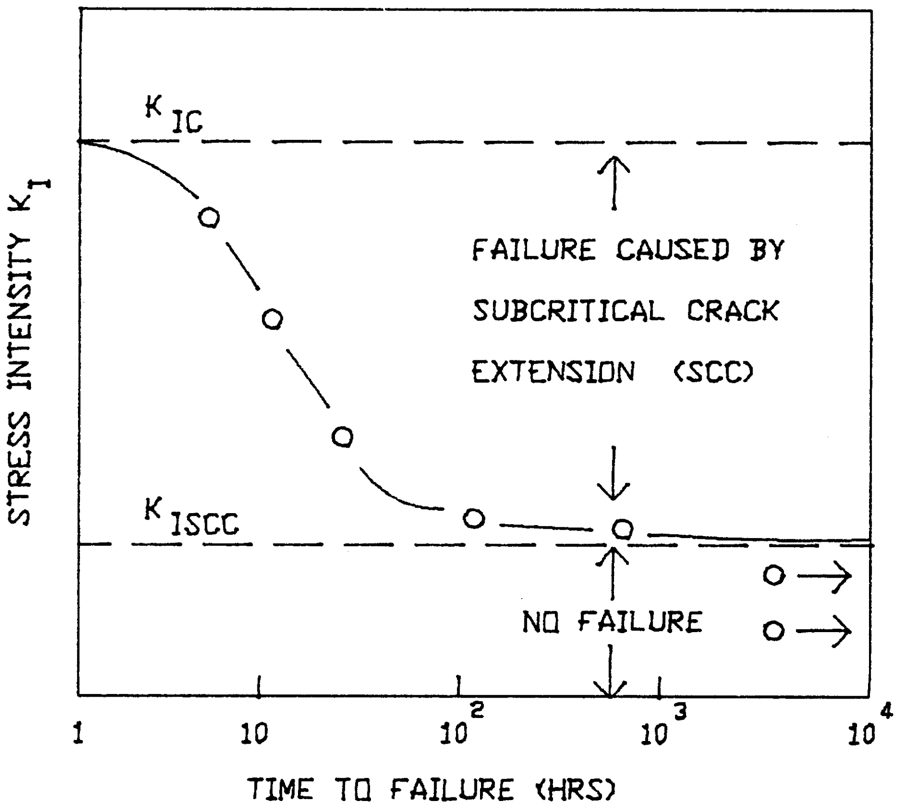

FIGURE 24 - Schematic Representation for Obtaining Critical Stress Intensity for SCC with Cantilever Beam Specimens.

The WOL test provides an equally valid measurement of K_{ISCC} with a single specimen by using the principle of constant displacement vice constant load for establishment of experimental conditions. The WOL specimen used for this experimental study was a slightly modified 1T specimen as shown in Figure 25. The deviations from the standard (bolted) specimen are as follows:

(1) The width B was reduced from the standard 1.0 inch (25.4 mm) to .9 inch (22.9 mm) in order that two specimens could be taken through the thickness of the 2.0 inch (50 mm) thick welded plate with allowance for machining and cutting tolerances.

(2) Side grooves were machined along each face of the specimen to guide the crack along a single plane and to prevent shear lips.

Constant displacement is achieved by threading a bolt into the top of the specimen until it impacts against the loading tup. The bolt is subsequently torqued while monitoring the crack opening displacement (COD) with a clip gage mounted between the two notches cut for this purpose at the mouth of the specimen as shown in Figure 25. (It should be noted at this juncture that the COD as a parameter is measured at the crack tip [23] and not at some arbitrary location on the specimen. However, the measurement taken at the mouth of the specimen can be directly correlated to the crack tip COD as it is in the same plane. In order to avoid unnecessary verbiage in future discussion, COD shall be used interchangeably,

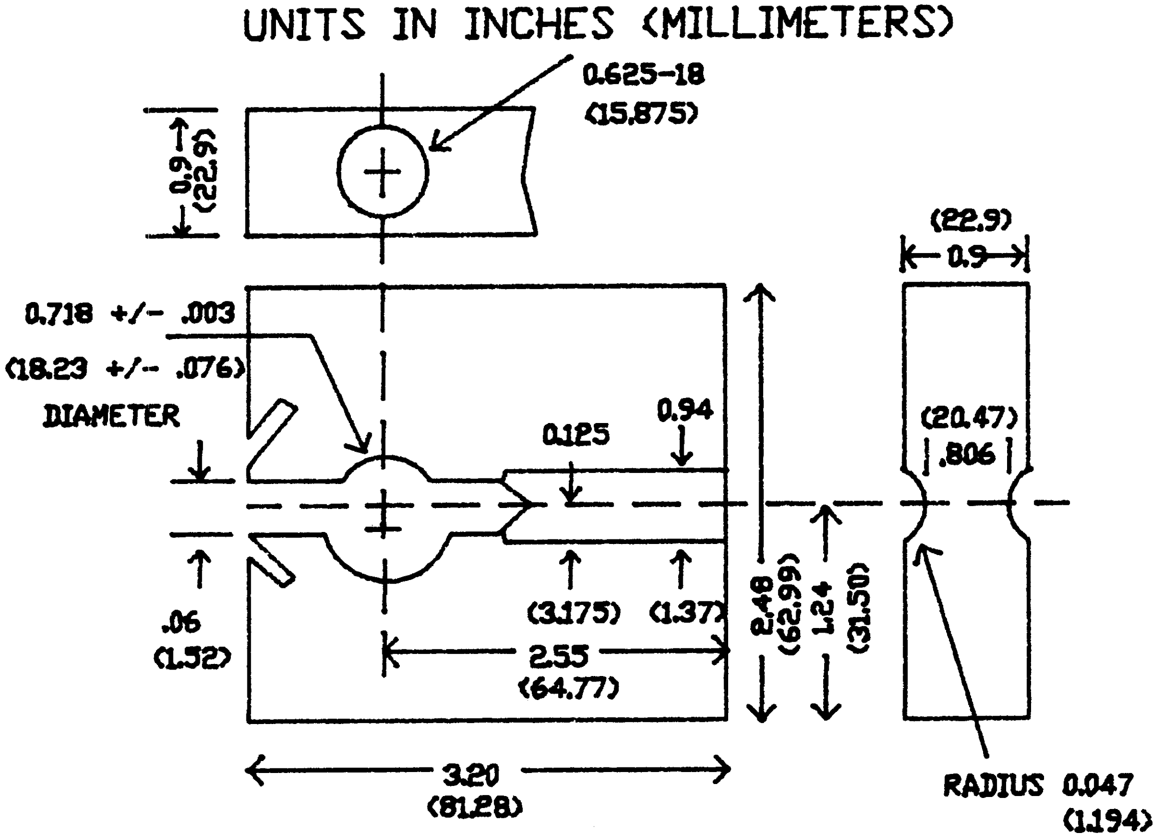

FIGURE 25 - Modified Wedge-Opening Load (WOL) Specimen used for Experimentation.

recognizing that it is a relative measure of COD that is being determined in the case of clip gage readings). Once loaded to the predetermined COD, the specimens are immersed in the test environment. Since the COD is fixed by the rigid bolt, the load and hence the stress intensity decrease as the crack extends. When the stress intensity has decreased sufficiently so that the crack stops growing, the critical stress intensity for stress corrosion cracking (K_{ISCC}) has been reached. The fundamental difference between WOL testing and cantilever beam testing is then that the constant load of the latter leads to increasing stress intensity with crack extension so that fracture will ultimately occur in every instance where initial stress intensity is greater than K_{ISCC}. This difference is shown graphically in Figure 26.

The relationship among crack length, stress intensity, COD and load have been established both theoretically and experimentally for the bolt-loaded modified WOL specimen of Novak and Rolfe [82]. It is these relationships that are used to set the original COD for a desired stress intensity (K_I) and to determine the final K_I reached at crack arrest. Two basic compliance equations are used to characterize the four fundamental variables, one relating COD (V) to load (F) and the other relating stress intensity (K_I) to load:

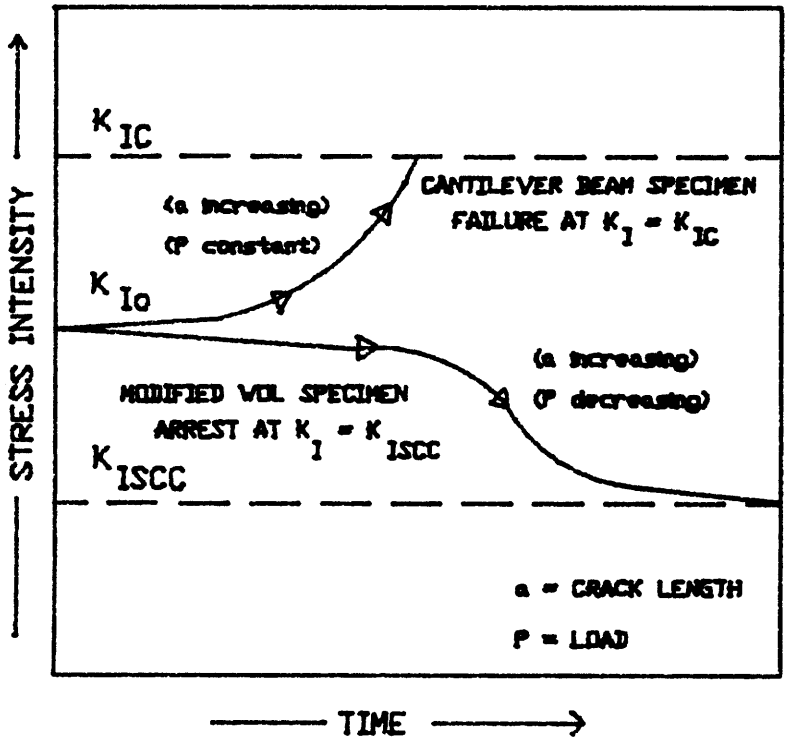

FIGURE 26 - Difference in Behavior for WOL and Cantilever Specimens.

(1) COD/LOAD COMPLIANCE CORRELATION

$$C_6(a/W) = E * (BB_N) * (V/P)^{1/2}$$

$$C_6(a/W) = e^{f(a/W)}$$

$$\text{Where } f(a/W) = 3.453 - 8.097(a/W) + 42.314(a/W)^2 - 64.677(a/W)^3 + 36.843(a/W)^4$$

(2) STRESS INTENSITY/LOAD COMPLIANCE CORRELATION

$$C_3(a/W) = a^{1/2} * (BB_N)^{1/2} * (K_I/P)$$

$$C_3(a/W) = 30.96(a/W) - 195.8(a/W)^2 + 730.6(a/W)^3 - 1186.3(a/W)^4 + 754.6(a/W)^5$$

Where a = Crack length

W = Specimen depth

B = Specimen thickness

B_N = Net specimen thickness (between grooves)

E = Young's modulus of elasticity

V = Crack Opening Displacement (COD)

P = Load

K_I = Stress intensity

The above equations yield a family of relationships among the key variables once crack length (a) is known:

EQUATION 1

$$V = K_I/E * (aB_N/B)^{1/2} * \{C_6(a/W)/C_3(a/W)\}$$

EQUATION 2

$$P = (EBV_{INITIAL})/\{C_6(a/W)\}$$

EQUATION 3

$$K_I = \{PC_3(a/W)\}/\{(BB_N)^{1/2} * a^{1/2}\}$$

These three equations, in addition to the empirical compliance equations, were used in this research to characterize the load and stress relationships for WOL testing.

5.3.2 SAMPLE PREPARATION

On receipt of the as-welded plates from DTNSRDC, specimen blanks were saw cut for further machining. Five different specimen types were chosen for analysis:

(1) Base metal.

(2) GMA weld metal.

(3) GMA heat-affected zone.

(4) SAW weld metal.

(5) SAW heat-affected zone.

Base metal samples were cut out along the plate without regard to rolling direction as mechanical property testing and microstructural analyses revealed no orientation differences. Weld metal and heat-affected zone samples were cut out such that the notches would be perpendicular to the weldment surface as shown in Figure 27. This configuration was chosen for two reasons:

(1) Specimens notched perpendicular to the weldment surface exhibit lower values of K_{ISCC} than specimens notched parallel to the weldment surface [85].

(2) Specimens notched parallel to the weldment surface would have required the use of .5T vice 1T specimens due to the constraints of plate thickness. The larger specimens were preferred as they were closer to meeting the dimensional size requirements of ASTM Specification E399.

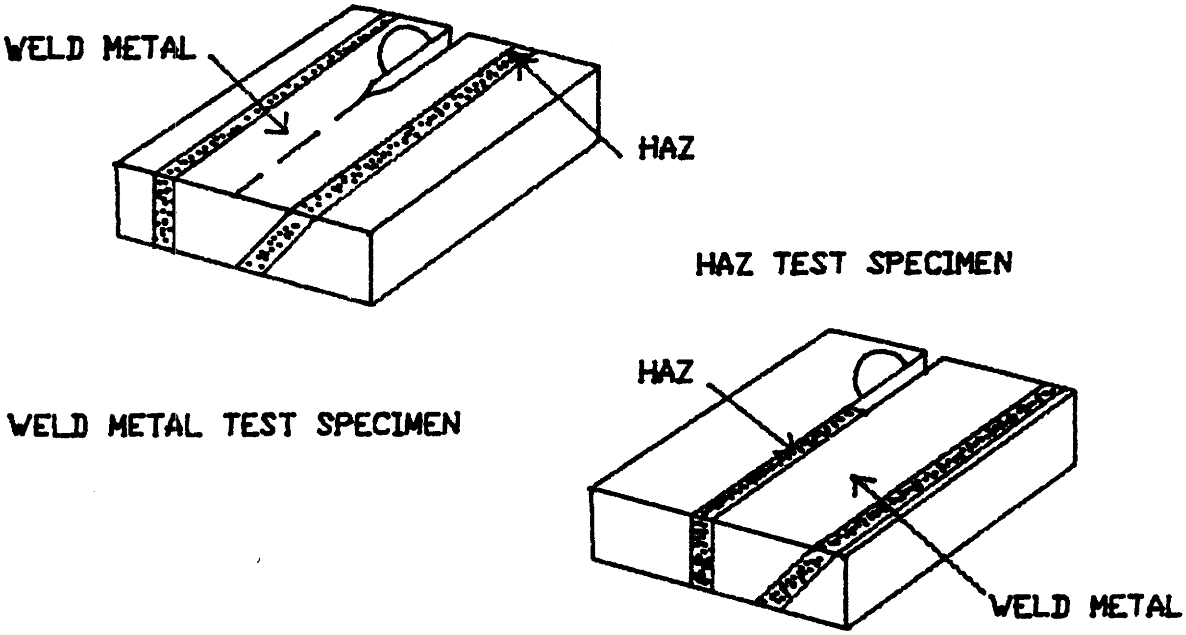

HAZ TEST SPECIMEN

WELD METAL TEST SPECIMEN

FIGURE 27 - Orientation of WOL Specimens Removed from Weldments.

The location of the heat-affected zone was determined by macroetching the end of each plate with a 5 percent Nital solution. The "K" weld prep was clearly visible with the heat-affected zone appearing as a darkened strip centered about 1/4 inch (6.4 mm) from the edge of the weld with a thickness of about 1/8 inch (3.2 mm). The heat-affected zone specimens were subsequently saw cut so as to be centered on the dark strip on the straight side of the "K". The weld metal samples were cut to be centered on the outermost weld bead (at the top and bottom of the "K") as shown in Figure 27. Following the rough saw cut of the specimen blanks, each individual heat-affected zone blank was macroetched with 5 percent Nital to locate the center of the heat-affected zone. Each blank was then stamped at the center of the heat-affected zone to serve as a guide for final specimen machining.

On receipt of the machined WOL specimens, the side grooves were hand polished with three grades of sandpaper (320, 400 and 600 grit) and emory paper to remove longitudinal machine scratches so that crack growth could be monitored during precracking and loaded testing. Three electrical leads were then welded to each specimen. Two of the leads were mounted on opposite sides of the notch to serve as sensing points for the potential drop system used to monitor crack initiation and growth during precracking as discussed below. The third lead was mounted on the top of the specimen to serve as a connection point for establishment of the desired potential during environmental testing.

Precracking was accomplished on an MTS Model 312.31 (serial number 1296) tensile tester rated at 55,000 pounds (244,750 newtons) controlled by an MTS 445 Controller with a Model 468 Test Processor. Precracking was computer controlled with an LSI 1123 Computer and an RT-11 Operating System. Each specimen was sinusoidally cycled in tension-tension at 10 Hertz with a maximum load of 6,568 pounds (29,228 newtons) and a minimum load of 656.8 pounds (2,923 newtons) for an R value of 0.1. This loading produced a maximum stress intensity of 30 ksi/in (33 MPa/m) at the root of the notch.

Crack growth was monitored by a potential drop system during cycling and by compliance measurement when a cycle run was terminated by excessive potential drop or by reaching a maximum preset number of cycles. The potential drop system, illustrated schematically in Figure 28 was powered by a Sorensen QRD 20-4 4.0 amp Power Supply. The potential drop across the specimen was amplified and input to the MTS Controller to serve as a shutdown signal in the event that the potential change associated with crack growth reached a limit set at the start of each run. The system essentially prevented excessive cycling on a given run so that crack growth could not proceed to the point at which K_{IC} was reached and rapid failure occurred.

Following each run of between 10,000 and 72,000 cycles (depending on the material), the compliance was determined by measuring the COD with a clip gage at the mouth of the specimen at 2,000, 3,000 and 4,000 pounds (8,900, 13,350, and

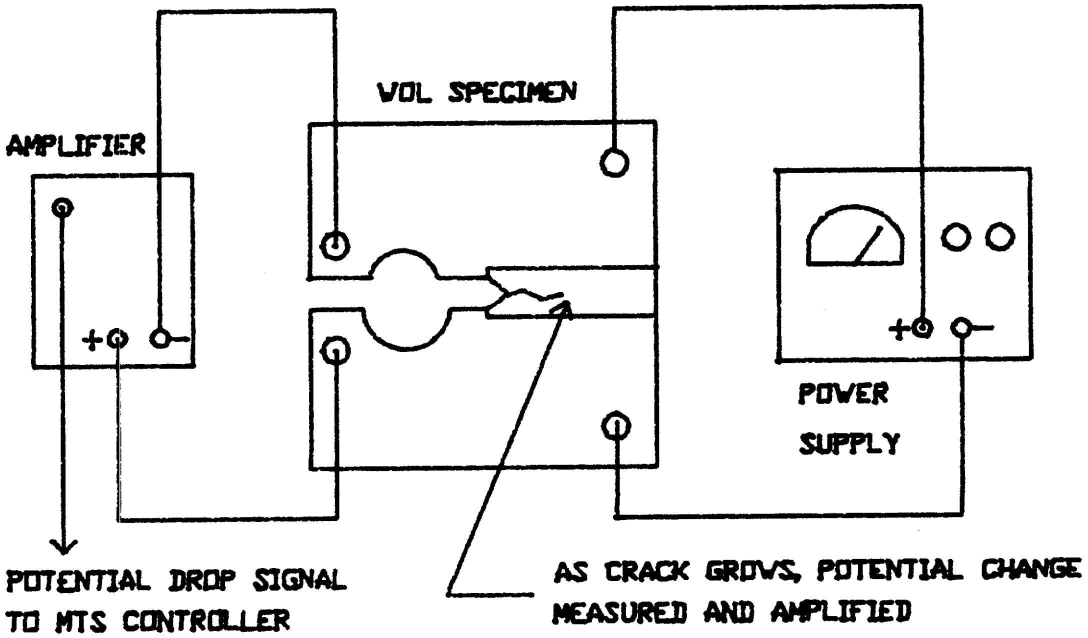

FIGURE 28 - Schematic of Potential Drop System used to Monitor Crack Growth during Precracking.

17,800 newtons). The measured compliance was compared to the experimental compliance of Reference 82 for crack length estimation. When the compliance indicated a crack length in excess of the required .1 inches (2.54 mm), the specimen was removed and inspected using a travelling stage microscope. The 0.1 inch (2.54 mm) minimum length for the precrack ensured that the crack tip extended beyond any potential notch machining effects such as cold work or thermally induced microstructure changes.

Visual measurement of precrack length was very difficult due to the hairline nature of the crack and the curved geometry of the notch. To provide a more accurate measurement of crack length to use in the final torque computation, the COD was computed for a stress intensity of 30 $\text{ksi}\sqrt{\text{in}}$ (33 $\text{MPa}\sqrt{\text{m}}$) since this had been used for precracking and each specimen was subsequently bolted open to the calculated COD value. The crack length on each side of the specimen was then measured and an arithmetic average computed. Based on this crack length, the COD for the environmental testing stress intensity (90 $\text{ksi}\sqrt{\text{in}}$, 100 $\text{ksi}\sqrt{\text{in}}$ or 110 $\text{ksi}\sqrt{\text{in}}$ {98.9 $\text{MPa}\sqrt{\text{m}}$, 109.9 $\text{MPa}\sqrt{\text{m}}$ or 120.9 $\text{MPa}\sqrt{\text{m}}$}) was computed and each specimen torqued to the required value. Final crack lengths were then measured and the actual stress intensities were computed based on this value and on the actual COD achieved.

The final crack lengths, measured compliances, calculated compliances and Reference 82 interpolated experimental compliances are compared in Tables 5.4, 5.5 and 5.6. The calculated compliances were determined from:

$$(V/P) = C_6 (a/W)/(E(BB_N)^{1/2}$$

Where E = 30,000,000 psi (206,820 MPa)

B = .9 inch (22.86 mm)

B_N = .806 inch (20.47 mm)

Crack length is listed as measured from the center of the load bolt which is .77 inches (19.56 mm) from the root of the notch. The actual precrack length is hence .77 inches (19.56 mm) less than that listed. The nominal stress intensity, computed COD, actual COD and actual stress intensity are listed in Tables 5.7, 5.8, and 5.9. Differences between nominal and actual stress intensity are due primarily to minor errors in crack length measurement between the preliminary torque value for 30 ksi$\sqrt{in}$ (33 MPa$\sqrt{m}$) and the final torque value. When fully torqued, the crack was readily visible and a very accurate crack length could be measured.

On completion of the final torquing process, the specimens were cleaned with methanol to prepare them for a beeswax coating application over all surfaces except the side grooves and the notch. Beeswax was chosen in lieu of paint or stop-off lacquer based on its reported successful use in similar seawater experiments [3] and on the recommendation of local researchers with seawater corrosion experimental experience. Additionally, an HSLA sample was coated with beeswax and immersed in the synthetic seawater used in this series of experiments for a period of one week prior to specimen torquing to certify coating integrity. Inspection at the end of this period revealed that the coating protected the underlying metal with no evidence of degradation or delamination.

The coating was considered necessary for all three of the corrosion potentials selected for analysis to prevent galvanic corrosion between the dissimilar metals (i.e. the loading bolt and the tup) and dissimilar weld regions (i.e. base metal, heat-affected zone and weld metal) of the loaded specimen assembly. As a secondary concern, coating was necessary for the specimens to be subjected to overcathodic protection at -1250 to -1300 millivolts SCE due to the high current levels which would be required if the entire specimen surface were open to the environment. Based on the polarization experiment discussed previously, it was determined that the current necessary to maintain the required potential would be 10 milliamps for every one square centimeter of surface area exposed. For 14 uncoated specimens, this would amount to about 1.7 amps per specimen or about 24 amps total current required. Coating was anticipated to reduce this requirement to about 20 milliamps per specimen or about .28 amps total.

TABLE 5.4

SAW (S) AND GMA (G) WELDED SPECIMENS COMPLIANCE CORRELATION

	CRACK LENGTH in (mm)	MEASURED COMPLIANCE in/lb (mm/N) $\times 10^{-6}$	CALCULATED COMPLIANCE in/lb (mm/N) $\times 10^{-6}$	REFERENCE 82 COMPLIANCE in/lb (mm/N) $\times 10^{-6}$
S1	1.040	1.695	1.787	1.738
	(26.41)	(191.6)	(202.0)	(196.4)
S2	1.089	1.787	1.934	1.864
	(27.66)	(202.0)	(218.6)	(210.7)
S3	0.991	1.525	1.650	1.621
	(25.17)	(172.4)	(186.5)	(183.2)
S4	1.113	1.751	2.012	1.934
	(28.27)	(197.9)	(227.4)	(218.6)
S5	0.988	1.627	1.643	1.614
	(25.10)	(183.9)	(185.7)	(182.4)
S6	1.263	1.612	2.561	2.520
	(32.08)	(182.2)	(289.4)	(284.8)
S7	1.008	1.582	1.695	1.662
	(25.60)	(178.8)	(191.6)	(187.9)
S9	1.169	1.868	2.202	2.122
	(29.69)	(211.1)	(248.9)	(239.8)
S0	1.130	2.058	2.066	1.983
	(28.70)	(232.6)	(233.5)	(224.1)
G1	1.032	1.626	1.764	1.719
	(26.21)	(183.8)	(199.4)	(194.3)
G2	1.035	1.699	1.771	1.726
	(26.29)	(192.0)	(200.2)	(195.1)
G4	1.133	1.896	2.078	1.992
	(28.78)	(214.3)	(234.9)	(225.1)
G5	0.961	1.546	1.570	1.551
	(24.41)	(174.7)	(177.5)	(175.3)
G6	1.017	1.597	1.719	1.683
	(25.83)	(180.5)	(194.3)	(190.2)
G7	1.049	1.700	1.812	1.759
	(26.64)	(192.2)	(204.8)	(198.8)
G8	1.001	1.465	1.676	1.645
	(25.43)	(165.6)	(189.4)	(185.9)
G0	1.069	1.743	1.872	1.807
	(27.15)	(197.0)	(211.6)	(204.2)

TABLE 5.5

SAW (SH) AND GMA (GH) HAZ SPECIMENS COMPLIANCE CORRELATION

	CRACK LENGTH in (mm)	MEASURED COMPLIANCE in/lb (mm/N) $\times 10^{-6}$	CALCULATED COMPLIANCE in/lb (mm/N) $\times 10^{-6}$	REFERENCE 82 COMPLIANCE in/lb (mm/N) $\times 10^{-6}$
SH1	1.003	1.676	1.681	1.650
	(25.48)	(189.4)	(190.0)	(186.5)
SH2	0.939	1.479	1.516	1.500
	(23.85)	(167.2)	(171.4)	(169.5)
SH3	1.002	1.604	1.678	1.648
	(25.45)	(181.3)	(189.7)	(186.3)
SH4	0.999	1.612	1.670	1.641
	(25.37)	(182.2)	(188.8)	(185.5)
SH5	0.970	1.583	1.594	1.571
	(24.64)	(178.9)	(180.2)	(177.6)
SH6	0.900	1.531	1.425	1.412
	(22.86)	(173.0)	(161.1)	(159.6)
SH8	0.984	1.699	1.631	1.605
	(24.99)	(192.0)	(184.4)	(181.4)
SH9	1.065	1.787	1.861	1.798
	(27.05)	(202.0)	(210.3)	(203.2)
SH0	0.975	1.706	1.607	1.583
	(24.77)	(192.8)	(181.6)	(178.9)
GH1	1.036	1.802	1.775	1.729
	(26.31)	(203.7)	(200.6)	(195.4)
GH2	1.116	1.962	2.020	1.942
	(28.35)	(221.8)	(228.3)	(219.5)
GH3	0.959	1.582	1.567	1.546
	(24.34)	(178.8)	(177.1)	(174.7)
GH5	1.316	2.630	2.792	2.630
	(33.43)	(297.3)	(315.6)	(297.3)
GH6	0.977	1.684	1.611	1.587
	(24.82)	(190.3)	(182.1)	(179.4)
GH7	0.980	1.626	1.619	1.595
	(24.89)	(183.8)	(183.0)	(180.2)
GH8	1.151	2.110	2.139	2.044
	(29.23)	(238.5)	(241.8)	(231.0)
GH9	1.026	1.750	1.745	1.705
	(26.06)	(197.8)	(197.2)	(192.7)
GH0	1.158	2.103	2.163	2.064
	(29.41)	(237.7)	(244.4)	(233.3)

TABLE 5.6

BASE METAL (N) SPECIMENS COMPLIANCE CORRELATION

	CRACK LENGTH in (mm)	MEASURED COMPLIANCE in/lb (mm/N) $\times 10^{-6}$	CALCULATED COMPLIANCE in/lb (mm/N) $\times 10^{-6}$	REFERENCE 82 COMPLIANCE in/lb (mm/N) $\times 10^{-6}$
N1	1.313	2.520	2.780	2.622
	(33.35)	(284.8)	(314.2)	(296.4)
N2	1.655	5.054	5.140	5.053
	(42.03)	(571.2)	(580.9)	(571.1)
N3	1.502	3.787	3.823	3.681
	(38.15)	(428.0)	(432.1)	(416.0)
N4	0.986	1.707	1.637	1.609
	(25.04)	(192.9)	(185.0)	(181.8)
N5	1.442	3.326	3.441	3.339
	(36.62)	(375.9)	(388.9)	(377.4)
N6	1.273	2.505	2.604	2.542
	(32.33)	(283.1)	(294.3)	(287.3)
N7	1.011	1.692	1.703	1.669
	(25.68)	(191.2)	(192.5)	(188.6)

TABLE 5.7

SAW (S) AND GMA (G) WELDED SPECIMENS
NOMINAL AND ACTUAL COD AND STRESS INTENSITY VALUES

	NOMINAL STRESS INTENSITY ksi/in (MPa/m)	COMPUTED COD in (mm)	ACTUAL COD in (mm)	ACTUAL STRESS INTENSITY ksi/in (MPa/m)
S1	100	.0268	.0268	96.9
	(109.9)	(0.681)	(0.681)	(106.5)
S2	110	.0304	.0305	106.5
	(120.9)	(0.772)	(0.775)	(117.0)
S3	110	.0280	.0287	107.9
	(120.9)	(0.711)	(0.729)	(118.6)
S4	100	.0265	.0266	91.1
	(109.9)	(0.673)	(0.676)	(100.1)
S5	100	.0266	.0266	100.2
	(109.9)	(0.676)	(0.676)	(110.1)
S6	90	.0268	.0267	82.6
	(98.90)	(0.681)	(0.678)	(90.8)
S7	110	.0287	.0299	111.0
	(120.9)	(0.729)	(0.759)	(122.0)
S9	90	.0259	.0260	82.3
	(98.90)	(0.658)	(0.660)	(90.4)
S0	90	.0266	.0270	91.4
	(98.90)	(0.676)	(0.686)	(100.4)
G1	100	.0269	.0271	98.7
	(109.9)	(0.683)	(0.688)	(108.5)
G2	90	.0246	.0246	89.5
	(98.90)	(0.625)	(0.625)	(98.4)
G4	90	.0262	.0267	90.2
	(98.90)	(0.665)	(0.678)	(99.1)
G5	100	.0259	.0262	100.8
	(109.9)	(0.658)	(0.665)	(110.8)
G6	110	.0298	.0299	110.4
	(120.9)	(0.757)	(0.759)	(121.3)
G7	110	.0296	.0300	108.1
	(120.9)	(0.752)	(0.762)	(118.8)
G8	110	.0290	.0292	108.8
	(120.9)	(0.737)	(0.742)	(119.6)
G0	100	.0281	.0282	100.1
	(109.9)	(0.714)	(0.717)	(110.0)

TABLE 5.8

SAW (SH) AND GMA (GH) HAZ SPECIMENS NOMINAL AND ACTUAL COD AND STRESS INTENSITY VALUES

	NOMINAL STRESS INTENSITY ksi/in (MPa/m)	COMPUTED COD in (mm)	ACTUAL COD in (mm)	ACTUAL STRESS INTENSITY ksi/in (MPa/m)
SH1	100	.0267	.0277	103.3
	(109.9)	(0.678)	(0.703)	(113.5)
SH2	110	.0274	.0277	108.3
	(120.9)	(0.696)	(0.703)	(119.0)
SH3	100	.0267	.0270	100.6
	(109.9)	(0.678)	(0.686)	(110.5)
SH4	90	.0236	.0238	88.9
	(98.90)	(0.599)	(0.605)	(97.7)
SH5	110	.0293	.0294	112.1
	(120.9)	(0.744)	(0.747)	(123.2)
SH6	110	.0272	.0286	115.3
	(120.9)	(0.691)	(0.726)	(126.7)
SH8	100	.0259	.0262	99.0
	(109.9)	(0.658)	(0.665)	(108.8)
SH9	90	.0249	.0255	90.6
	(98.90)	(0.632)	(0.648)	(99.5)
SH0	90	.0237	.0237	89.2
	(98.90)	(0.602)	(0.602)	(98.0)
GH1	100	.0275	.0283	102.8
	(109.9)	(0.699)	(0.719)	(113.0)
GH2	90	.0264	.0267	91.5
	(98.90)	(0.670)	(0.678)	(100.6)
GH3	110	.0283	.0280	107.8
	(120.9)	(0.719)	(0.711)	(118.5)
GH5	100	.0330	.0336	100.5
	(109.9)	(0.838)	(0.853)	(110.4)
GH6	110	.0287	.0292	110.9
	(120.9)	(0.729)	(0.742)	(121.9)
GH7	110	.0282	.0285	107.9
	(120.9)	(0.716)	(0.742)	(118.6)
GH8	90	.0268	.0268	89.5
	(98.90)	(0.681)	(0.698)	(98.4)
GH9	100	.0269	.0272	99.5
	(109.9)	(0.683)	(0.708)	(109.3)
GH0	90	.0272	.0272	90.3
	(98.90)	(0.691)	(0.708)	(99.2)

TABLE 5.9

BASE METAL (N) SPECIMENS
NOMINAL AND ACTUAL COD AND STRESS INTENSITY VALUES

	NOMINAL STRESS INTENSITY ksi/in (MPa/m)	COMPUTED COD in (mm)	ACTUAL COD in (mm)	ACTUAL STRESS INTENSITY ksi/in (MPa/m)
N1	90	.0299	.0307	92.0
	(98.90)	(0.759)	(0.780)	(101.1)
N2	90	.0340	.0368	87.7
	(98.90)	(0.864)	(0.925)	(96.4)
N3	100	.0363	.0364	99.5
	(109.9)	(0.922)	(0.925)	(109.4)
N4	100	.0270	.0349	101.7
	(109.9)	(0.686)	(0.886)	(111.8)
N5	90	.0319	.0327	91.5
	(98.90)	(0.810)	(0.831)	(100.6)
N6	100	.0321	.0326	100.2
	(109.9)	(0.815)	(0.828)	(110.1)
N7	110	.0295	.0298	110.1
	(120.9)	(0.749)	(0.757)	(121.0)

5.3.3 TEST APPARATUS

Following coating, the specimens were transported to the test facility and placed in a bath of recirculating synthetic seawater. The experimental arrangement is depicted schematically in Figure 29. As shown in the test matrix (Table 5.1), the 42 total specimens were subdivided into three groups of fourteen for the three corrosion potentials to be evaluated. Within each group of fourteen, the five different specimen material types (base metal, GMA weld metal, GMA HAZ, SAW weld metal and SAW HAZ) were torqued to two or three levels of stress intensity to fully cover the anticipated K_{ISCC} range.

The free corrosion specimens were torqued, coated and immersed on 7 January, 1986. A separate tank was used for these specimens to physically isolate them from the cathodically charged samples to minimize ionic interference. The cathodically protected (zinc-coupled) samples were torqued, coated and immersed on 17 January, 1986. The -1000 MV SCE potential was maintained with a Wenking 70TS1 Potentiostat manufactured by G. Bank Electronik. The counter electrode was a .065 inch thick sheet of Hastalloy S, a nickel based alloy very similar in composition to Hastalloy C and hence very noble with respect to iron and steel [12]. This material was chosen in lieu of the more commonly used platinum due to its availability and due to the expense of a large platinum sheet. The overcathodically protected (hydrogen generating) samples were torqued, coated and immersed on 23

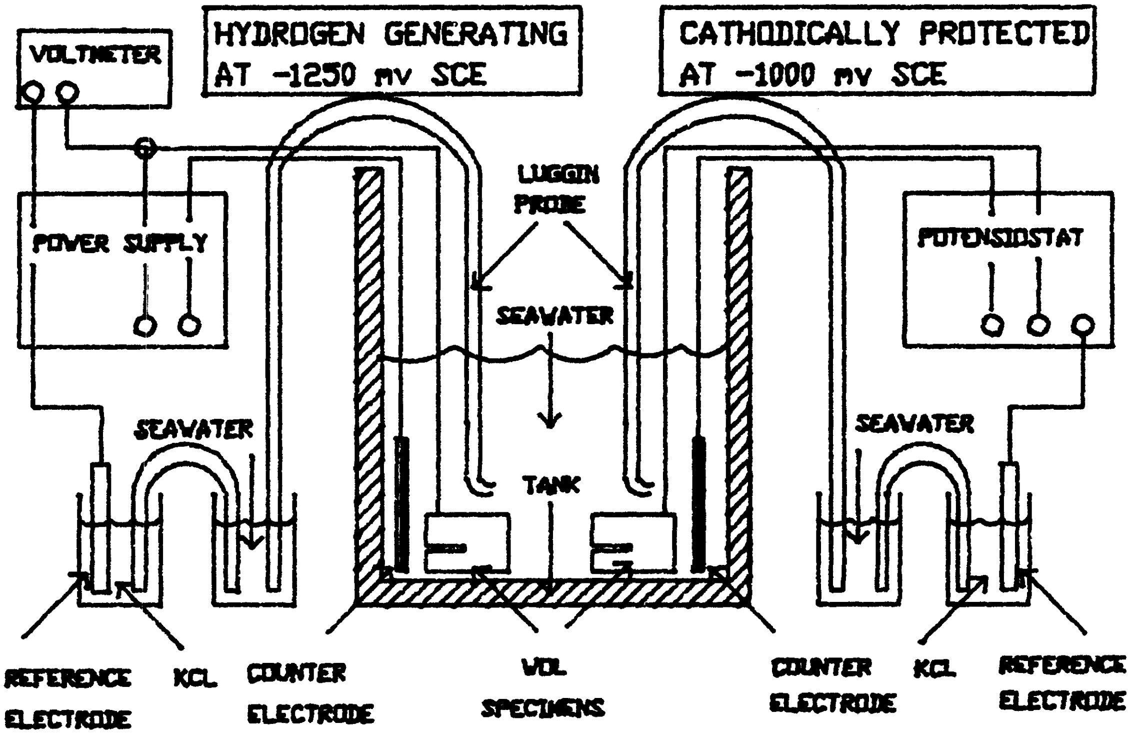

NOTE: FREE CORROSION SAMPLE IN SEPARATE TANK WITH NO ELECTRICAL CONNECTIONS

FIGURE 29 - Schematic of Test Apparatus used for Potential Control of WOL Specimens in Synthetic Seawater Environment.

January, 1986. The -1250 to -1300 MV SCE potential was monitored with a John Fluke 8600A Digital Voltmeter with current supplied by a Sorenson QRD 20-4 4.0 amp Regulated Power Supply. The counter electrode used for this cell was also a sheet of Hastalloy S.

During the course of the experiment, the specimens were visually inspected at least daily and voltage and current readings taken and adjusted if necessary. The specimens were removed from the seawater bath weekly for the first month and biweekly thereafter for observation with a travelling stage microscope. The side grooves required light abrasion to remove accumulated rust in order to monitor crack advance. This was accomplished with light nylon brushes, sandpaper and cotton tipped applicators.

5.4 SLOW STRAIN RATE TESTING

5.4.1 BACKGROUND

The slow strain rate (SSR) test for the evaluation of material susceptibility to stress corrosion cracking has now been in use for a number of years and has been widely accepted by the most skeptical of the experimental research community [86]. As the name implies, it is essentially a slow tensile test in the sense that a specimen is pulled apart at a constant strain rate until failure occurs. Its primary advantage over the related constant load and constant total strain tests is that it concludes with the failure of the specimen marking a distinct termination point. Under other forms of loading, failure may or may not occur and the test must be terminated at an arbitrary time. This may give rise to some doubt as to the validity of the test and result in considerable data scatter in otherwise identical experiments.

The role of dynamic strain in SCC is central to the argument for the validity of the SSR test. Since most service failures appear to occur under conditions of static load, the case for dynamic strain merits some explanation. SCC is a crack initiation and propogation process under specific stress and environmental conditions. Even under constant load, the stress at the crack tip must increase for the crack to propogate. Whether this occurs due to electrochemical dissolution or film rupture or by some other mechanism is a theoretical issue which has been previously discussed and is immaterial to the current argument. Regardless of the mechanism chosen, dynamic strain must play a role in SCC [87]. To show that this is in fact the case, Parkins [86] conducted a series of experiments with C-Mn steel loaded in an environment of carbon trioxide-hydrocarbonate, which was known to cause SCC for a given range of potentials. To establish the baseline condition, the material was first loaded in the potential range known to cause SCC (Curve A of Figure 30) and then in the potential range where SCC did not occur (Curve B). The difference between Curves A and B then reflects the increased deflection caused by SCC crack initiation and propogation. To validate the strain rate dependence, two additional tests were run. In the first, the potential was initially held in the non-SCC range for about 40 hours and then changed to the SCC range. Curve C reflects the fact that no SCC occurred. In the second, the potential was again held in the non-SCC range initially, but changed to the SCC range after about 12 hours. Curve D reflects the fact that SCC occurred. The only difference between the two tests was the creep rate or strain rate of the material following initial load application. For Curve C, the creep rate had dropped to a very low value whereas for Curve D it remained at its initial high value. These results, along with similar results in other material/environment systems, confirm the fact that strain rate is a controlling parameter for SCC.

The foregoing experiment points out another key aspect of the strain rate dependence of SCC in that there is some critical value of strain rate below which SCC will not occur.

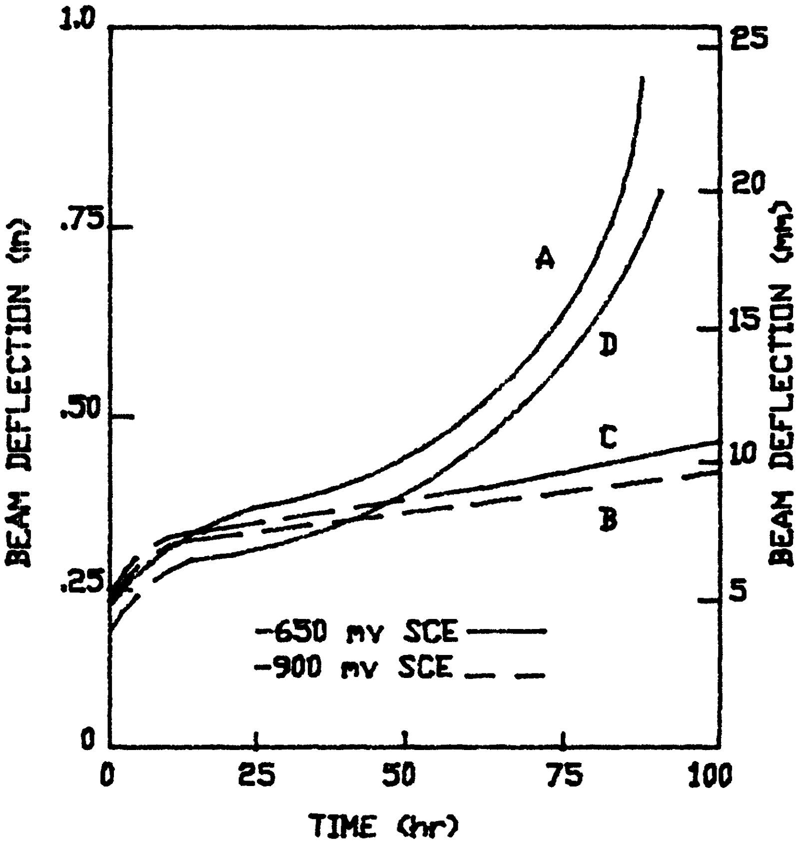

FIGURE 30 - Beam Deflection-Time Curves for Constant Load Cantilever Beam Tests on C-Mn Steel in an SCC Environment Showing Effects of Cracking (-650 mv) and Non-cracking (-900 mv) Potentials.

In fact, there is an experimentally observed strain rate range with both an upper and lower limit for which a specific material/environment system will undergo SCC. Straining outside this range results in the same mode of failure which would have occurred in the absence of environmental effects (i.e. no SCC detected). For example, Ti-5Al-2.5Sn in NaCl will undergo SCC in the range of 10^{-5} to 10^{-4} second^{-1} for unnotched specimens [88]. For most systems, strain rates in the range 10^{-5} to 10^{-6} second^{-1} promote SCC [86]. Steels generally exhibit the most severe SCC at a strain rate of about 10^{-6} second^{-1} regardless of the specific SCC producing environment [87].

The upper limit on strain rate is fairly easy to explain. With a high strain rate, there is insufficient time for the crack to propogate relative to the strain occurring in the substrate [85]. Further, rapid straining does not allow sufficient time for the establishment of the electrochemical conditions necessary to promote SCC [86]. The lower limit on strain rate is not as easy to explain and there is some conjecture as to its cause. The most plausible and widely held theories [87,88] emphasize the role of film formation in the SCC process. According to the Film Rupture Theory [30], straining induces the formation of slip-steps which emerge at the surface of the material, breaking the film in the process. The small area of metal thus exposed is anodic to the filmed regions adjacent to the emergent slip-step and is hence locally corroded by the environment. Once initiated, the crack propogates in like manner as long as straining continues. The slow strain rate test induces slip-step emergence by the application of continuous strain, thus providing the conditions necessary for SCC to occur.

Based on the Film Rupture Theory, the lower limit on strain rate may be explained in several ways. The first is based on the rate of film formation versus the rate of film rupture. If the conditions are such that a protective film covers the freshly exposed material from a film rupture event before the electrochemical conditions for localized corrosion can be established, then the crack won't grow. The strain rate, which governs the rate of slip step emergence, would then have a lower limit determined by the film formation rate [87]. A second related explanation is based on the fact that SCC causing electrolytes dissolve protective films at a finite rate [88]. If the film that is stressed by the application of continuous strain is then dissolved and replaced by stress free film before it can rupture, then the exposure of fresh material to the corrosive electrolyte would be precluded. These conditions would also depend on a low strain rate to limit the rate of stressed film formation to that which could be removed and replaced. Finally, if SCC depends on a poorly protective film and slow straining allows for the formation of a more protective film, then SCC susceptibility would again be suppressed at some critical low strain rate.

A similar strain rate dependence does not occur in the case of hydrogen-assisted cracking (HAC) since the entry of hydrogen into a material so as to cause embrittlement does not require film rupture. In fact, lower strain rates favor HAC since more time is available for the cathodic reduction reaction to generate hydrogen and for the hydrogen to diffuse into the material. An upper strain rate limit would still occur in the case of HAC since some finite time is required for hydrogen generation and diffusion. The slow strain rate test performed at different strain rates can thus serve to identify the failure mechanism, as shown in Figure 31 [87].

The slow strain rate test also requires the establishment of an electrode potential within a well defined range to cause cracking. Since SCC is fundamentally an electrochemical process, its dependence on electrode potential is hardly surprising and has long been recognized [89]. In essence, the cracking process requires a balance between the activity at the crack tip relative to the passivity of the crack sides. Again using the Film Rupture Theory, crack advance by SCC will occur only when the small area of exposed material at the crack tip is anodic with respect to the larger adjacent crack sides. The narrow range of electrode potential at which this relationship is possible defines the critical cracking potential range which depends not only on the material/environment system, but on the applied strain rate as well [88].

The data derived from slow strain rate tests can be used to characterize the susceptibility of a specific material/ environment system to SCC and HAC both qualitatively and

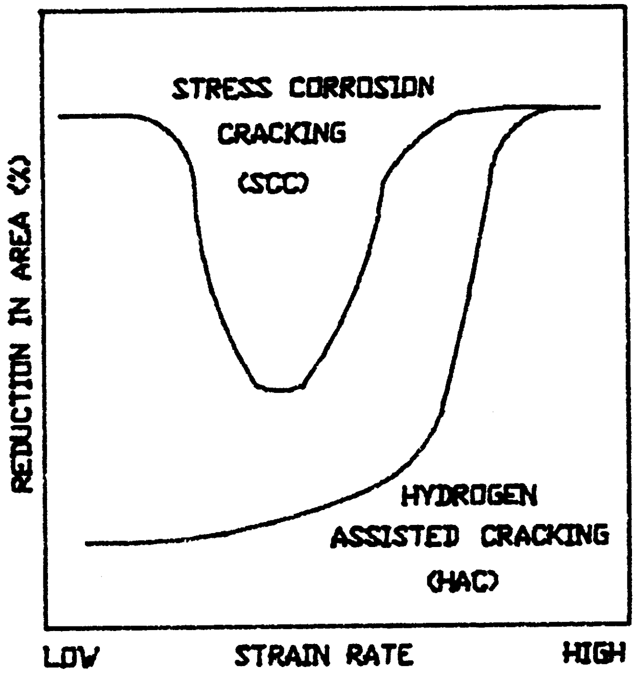

FIGURE 31 - Comparison of the Effects of Strain Rate on Stress Corrosion Cracking and Hydrogen Embrittlement.

quantitatively. The most conclusive indication of susceptibility to environmental cracking is the qualitative analysis of the fracture surface by photomicrographic study and evaluation [90]. Fracture surfaces with cleavage planes characteristic of brittle failure and the presence of numerous secondary cracks perpendicular in orientation to the applied stress are unambiguous indications of environmentally induced cracking. These qualitative measures are supported by a wide range of quantitative parameters which characterize the strength and ductility of the material tested [86-88,90,91]:

(1) **Reduction of Area (ROA)** - ROA quantitatively expresses the ductility of a material by taking the ratio of the change in the cross sectional area of the specimen due to testing to the initial area as follows:

$$ROA = (A_o - A_f)/A_o$$

Where A_o = Initial Area
A_f = Final Area

A material with high ductility has a relatively high ROA in relation to one with low ductility since it can be deformed more extensively prior to fracture.

(2) **Time-of-Failure (TOF)** - TOF provides a quantitative index of cracking severity since cracking promotes premature failure. Since TOF is not an absolute measure it must be correlated to a baseline condition to provide a relative measure of cracking severity. Typically, TOF

values measured during an SCC slow strain rate test are divided by TOF values measured under identical strain and temperature conditions in an environment that does not promote SCC. For TOF data normalized in this manner, a value less than one indicates SCC or HAC susceptibility.

(3) __Load-Extension Curve Parameters__ - During slow strain rate tesing, a plot of applied tensile load versus specimen elongation is obtained. For most materials, the curve has three distinct regions: the elastic region in which load increases linearly with elongation; the uniform plastic region in which load continues to increase at less than a linear rate until the onset of necking; and the plastic region in which load decreases as the specimen necks ultimately falling to zero at failure. Numerous parameters can be measured from the load extension curve to serve as a relative index to SCC or HAC severity. As shown in Figure 32, these include load at yield (L_y), maximum load (L), failure load (L_f), uniform plastic elongation (e_u), total elongation (e_t) and area under the curve (A). The derived parameters of yield strength (YS), ultimate tensile strength (UTS), and failure strength (FS) may then be determined by dividing L_y, L, and L_f respectively by the original specimen cross sectional area. Under conditions which cause environmental cracking, the curve will typically be smaller and shorter as indicated in Figure 32 so that any of the above parameters may be used to characterize

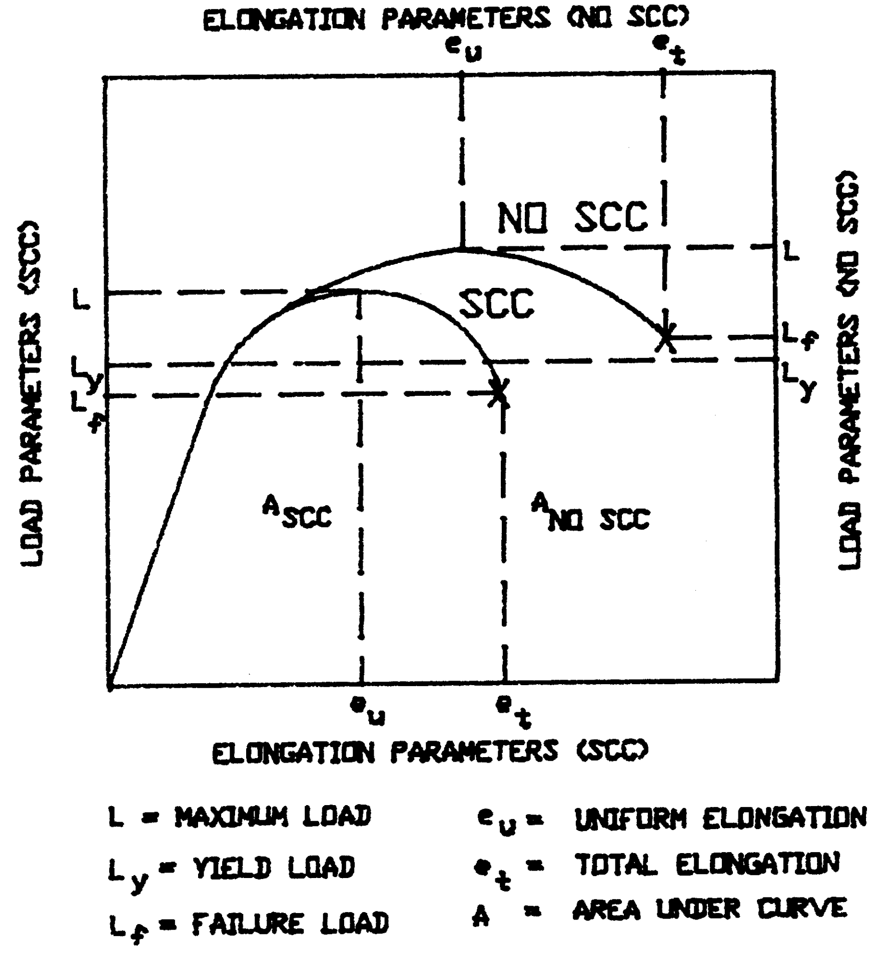

FIGURE 32 - Parameters Derived from Load-Extension Curve.

relative SCC or HAC susceptibility.

(4) **Zero Gage Length Elongation (e)** - Elongation measurements taken during slow strain rate testing are not directly comparable due to cross sectional area changes that vary with the ductility of the material. To eliminate this effect, the constancy of volume may be employed to derive the zero gage length elongation from ROA data as follows:

$$A * L = A_o L_o \quad \text{by constant volume}$$

$$L_o/L = A/A_o$$

$$ROA = (A - A_o)/A = 1 - A_o/A$$

$$e = (L - L_o)/L = 1 - A/A_o$$

$$= 1 - (1/(1-ROA))$$

$$= ROA/(1 - ROA)$$

Where A = Final Area

A_o = Initial Area

L = Final Length

L_o = Initial Length

e = Zero Gage Length Elongation

The zero gage length elongation (e) may then be used to directly compare the results of slow strain rate tests conducted with different materials and/or environments as a measure of ductility.

Numerous other quantitative measures and correlations have been proposed as key indicators of susceptibility to SCC or HAC. Regardless of the index or indices chosen, it has been found experimentally that the slow strain rate test is so severe that it may give ambiguous quantitative results [87]. The best indicator must ultimately be the qualitative evaluation of the fracture surface supported by quantitative measures of strength and ductility parameters.

5.4.2 SAMPLE PREPARATION

Slow strain rate specimen blanks were saw cut from the welded plates to a convenient size for machining of the base metal, SAW and GMA weld metal and heat-affected zone specimens. All of the blanks were cut out parallel to the weld axis in the plate longitudinal direction as shown in Figure 33. This configuration was selected to ensure that the entire specimen blank would have a uniform cross-sectional composition. Due to the "K" weld geometry, a specimen taken through the plate thickness would have sections of base metal, weld metal and HAZ along the length of the specimen. Subsequent SSR testing would then have only revealed which of the three regions was the weakest, for failure would always occur in the same material.

The location of the heat-affected zone was determined by macroetching the end of the blank with a 5 percent Nital solution as was done with the WOL specimens. There was no need to etch the ends of the weld metal blanks since the entire blank was removed from the weld metal volume. The specimen blanks were subsequently machined to the final specimen geometry shown in Figure 34. Just prior to testing, the gage length section of each specimen was polished with 3 micron METADI-2 Diamond Compound for Metallography manufactured by Bueheler, Ltd. to remove any surface imperfections.

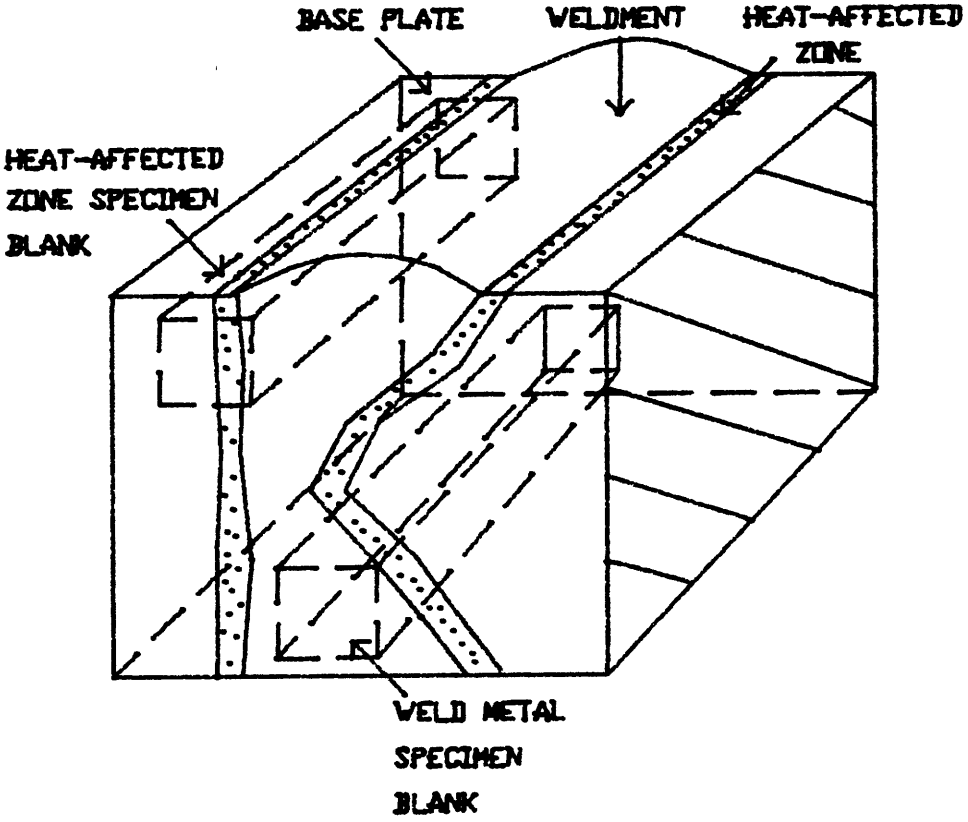

FIGURE 33 - Orientation of Slow Strain Rate Specimens Removed from Weldments.

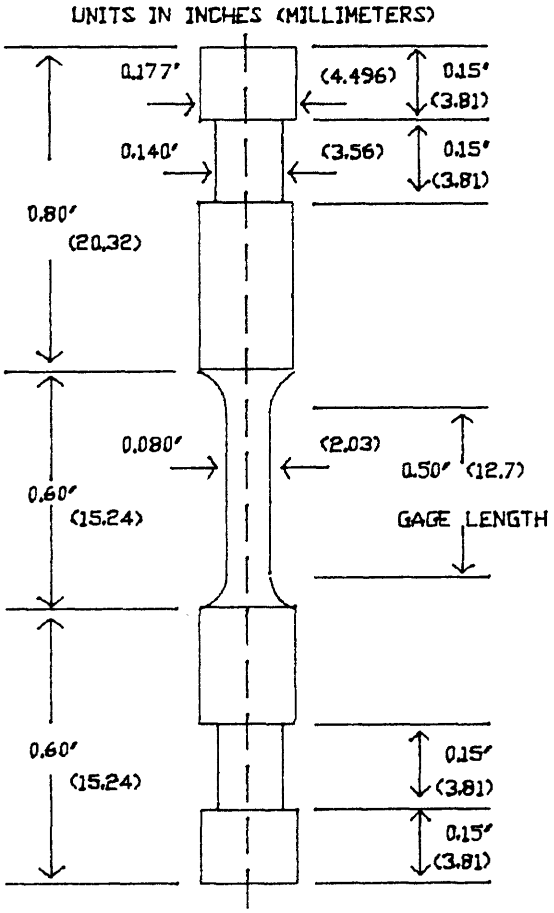

FIGURE 34 - Slow Strain Rate Specimen used for Experiments.

5.4.3 TEST APPARATUS

Slow strain rate testing was conducted on two different tensile loading machines. An Instron Universal Testing Machine Model TTC M1.6 with a minimum crosshead speed of .002 inches per minute (.05 mm per minute) was used for the highest strain rate test. With a 1/2 inch (12.7 mm) gage length, the strain rate was then:

$$\frac{(.002 \text{ in/min}) \text{ X } (1 \text{ min/60 seconds})}{1/2 \text{ inch}} = 6.67 \times 10^{-5} \text{/sec}$$

Since this was the minimum crosshead speed, a second machine was procured and installed for the lower strain rate testing. An Instron Model 1131 with a crosshead speed of .00025 inches per minute (.00635 mm per minute) was used for the lower strain rate of 8.33×10^{-6} /sec derived as above.

The potentials used for the testing at the two strain rates are shown in Table 5.1 and are the same as those used for WOL testing. Selected tests were also conducted at a slower strain rate (8.33×10^{-7} /sec) and at a faster strain rate (1.67×10^{-4} /sec) to provide data for assessment of the strain rate dependence of key parameters.

A schematic of the slow strain rate test apparatus is shown in Figure 35. For free corrosion tests, the specimens were immersed in synthetic seawater at room temperature with no potentiostatic control. For the cathodically protected and hydrogen charging tests, a Wenking 70TS1 Potentiostat was used with a saturated calumel reference electrode and a platinum

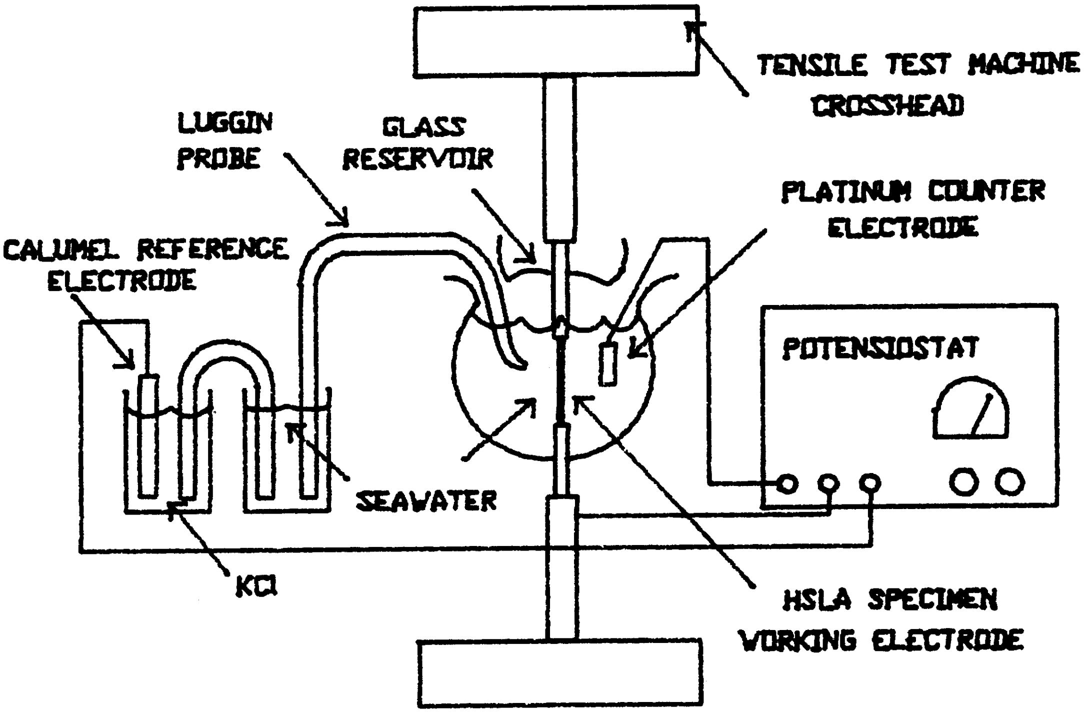

FIGURE 35 - Test Apparatus used for Slow Strain Rate Testing.

counter electrode to control the potential at either -1000 mv SCE or -1250 mv SCE as required for the specific test. A plot of load versus displacement was made during each test for subsequent data evaluation and analysis. Following failure, each specimen was removed from the seawater test enclosure and rinsed with acetone. The final diameter of each specimen was then measured with a hand-held micrometer under a 4X stereoscopic microscope for improved accuracy. The fracture surface of each specimen half was finally coated with an acetate film to protect the fracture surface from damage or further corrosion for future photomicrographic evaluation.

6. RESULTS OF EXPERIMENTAL RESEARCH

6.1 WEDGE-OPENING LOAD TESTING

At the conclusion of the test, the specimens were removed from the seawater bath, dried and cleaned to remove corrosion products from the exposed surfaces and scraped to remove the wax coating from the protected surfaces. The total test duration was 2016 hours for the free corrosion specimens, 1488 hours for the cathodically protected specimens (-1000 mv SCE) and 1608 hours for the cathodically overprotected/hydrogen generating specimens (-1250 mv SCE). Following transport to the mechanical test facility, the specimens were clamped in a vise and unloaded while monitoring the COD with a clip gage at the mouth of the specimen using identical but opposite procedures to those followed in the loading sequence (Section 5.3.2). Each specimen was subsequently mounted on the MTS tensile testing machine used for precracking and loaded to the COD measured during unloading to determine the final arrest load (Parrest). Compliance measurements were taken every 2,000 pounds (8,900 N) by monitoring the change in COD for subsequent crack length correlation.

The 20,000 pound (89,000 N) load limit of the available testing machine precluded specimen separation by direct application of load for all but a few specimens (those with long cracks and small remaining ligaments). Time constraints for data accumulation precluded an extensive cycling program to further fatigue the specimens and extend the cracks. Consequently, the specimens were rebolted open to the maximum extent physically possible and placed in a bath of liquid nitrogen. After allowing approximately 30 minutes for temperature equalization, the specimens were removed from the bath and subjected to an impact load. The combination of applied stress, low temperature and an impact load produced a clean break in the plane of the crack. Although this somewhat unorthodox procedure is contrary to standard practice [3,82], it proved highly effective in producing the desired result.

Following specimen fracture, crack lengths were measured with a travelling stage microscope at each face and at the center of the specimen. An average crack length was then computed as recommended by Novak and Rolfe [82] according to:

$$a_{average} = \frac{a_{left} + 4a_{center} + a_{right}}{6}$$

The crack length data is presented in Table 6.1 with the initial estimated crack length for comparison purposes (in both Tables 6.1 and 6.2 specimens are coded by S for SAW weld metal, G for GMA weld metal, SH for SAW HAZ, GH for GMA HAZ and N for base metal). The final stress intensity was then computed from the average crack length and the arrest load (Parrest) data as follows [82]:

$$K_I = \frac{(Parrest)(C_3(a/W))}{\sqrt{(B)(B_N)(a)}}$$

where the variables are as previously defined. Final stress intensity values are presented in Table 6.2 with crack length and compliance data for each specimen.

While exposed to the seawater test environment, the crack sides became heavily corroded, effectively precluding microscopic evaluation of the final fracture surfaces. In order to clean the fracture surfaces for observation, a chemical etching solution was employed to remove corrosion products. The mixture used was 3 ml of hydrochloric acid (HCl) inhibited with 4 ml of 2-Butyne-1,4-diol in 50 ml of deionized water [92]. Selected specimens (i.e. those specimens for which crack extension was predicted by crack length measurement) were placed in the inhibited acid bath for 30 seconds and subsequently rinsed in deionized water and then alcohol. The chemically etched specimens were then inspected with a stereoscopic microscope to evaluate the extent of cracking.

TABLE 6.1

WEDGE-OPENING LOAD (WOL) CRACK LENGTH CALCULATIONS

CATHODICALLY OVERPROTECTED-HYDROGEN GENERATING
(-1250 MV SCE)

SPECIMEN	LEFT LENGTH in (mm)	CENTER LENGTH in (mm)	RIGHT LENGTH in (mm)	AVERAGE LENGTH in (mm)	INITIAL LENGTH in (mm)
S9	0.42	0.54	0.35	0.49	0.40
	(10.74)	(13.67)	(8.89)	(12.45)	(10.16)
S1	0.33	0.44	0.24	0.38	0.27
	(8.30)	(11.05)	(6.10)	(9.65)	(6.85)
S7	0.15	0.45	0.24	0.37	0.24
	(3.89)	(11.48)	(6.10)	(9.40)	(6.10)
G1	0.19	0.44	0.31	0.38	0.26
	(3.88)	(11.10)	(7.87)	(9.65)	(6.60)
G7	0.25	0.43	0.30	0.38	0.28
	(6.40)	(11.00)	(7.62)	(9.65)	(7.11)
SH0	0.22	0.35	0.15	0.30	0.22
	(5.56)	(8.94)	(3.89)	(7.62)	(5.56)
SH3	0.25	0.31	0.20	0.28	0.23
	(6.35)	(7.87)	(5.08)	(7.11)	(5.84)
SH6	0.11	0.28	0.15	0.23	0.13
	(2.77)	(7.11)	(3.89)	(5.84)	(3.30)
GH8	0.44	0.44	0.28	0.41	0.38
	(11.13)	(11.18)	(7.11)	(10.41)	(9.65)
GH1	0.22	0.36	0.31	0.33	0.27
	(5.56)	(9.14)	(7.87)	(8.30)	(6.85)
GH6	0.25	0.30	0.25	0.28	0.21
	(6.35)	(7.62)	(6.35)	(7.11)	(5.34)
N5	0.65	0.66	0.67	0.66	0.67
	(16.51)	(16.76)	(17.01)	(16.76)	(17.01)
N6	0.51	0.52	0.51	0.52	0.50
	(12.95)	(13.21)	(12.95)	(13.21)	(12.70)
N7	0.25	0.28	0.27	0.27	0.29
	(6.35)	(7.11)	(6.86)	(6.86)	(7.36)

TABLE 6.1
(CONTINUED)

WEDGE-OPENING LOAD (WOL) CRACK LENGTH CALCULATIONS

CATHODICALLY PROTECTED
(-1000 MV SCE)

SPECIMEN	LEFT LENGTH in (mm)	CENTER LENGTH in (mm)	RIGHT LENGTH in (mm)	AVERAGE LENGTH in (mm)	INITIAL LENGTH in (mm)
SO	0.40	0.54	0.32	0.48	0.36
	(10.16)	(13.72)	(8.13)	(12.19)	(9.14)
S5	0.28	0.38	0.12	0.32	0.22
	(7.11)	(9.65)	(3.05)	(8.13)	(5.59)
S3	0.13	0.35	0.29	0.30	0.22
	(3.30)	(8.89)	(7.37)	(7.62)	(5.59)
G4	0.38	0.45	0.36	0.42	0.36
	(9.65)	(11.43)	(9.14)	(10.67)	(9.14)
GO	0.19	0.41	0.40	0.37	0.30
	(4.83)	(10.41)	(10.16)	(9.40)	(7.62)
G8	0.15	0.34	0.29	0.30	0.23
	(3.81)	(8.64)	(7.37)	(7.62)	(5.84)
SH9	0.27	0.34	0.31	0.32	0.30
	(6.86)	(8.64)	(7.87)	(8.13)	(7.62)
SH1	0.24	0.32	0.22	0.29	0.23
	(6.10)	(8.13)	(5.59)	(7.37)	(5.84)
SH2	0.21	0.31	0.12	0.26	0.17
	(5.33)	(7.87)	(3.05)	(6.60)	(4.32)
GHO	0.38	0.45	0.38	0.43	0.39
	(9.65)	(11.43)	(9.65)	(10.92)	(9.91)
GH5	0.45	0.57	0.37	0.51	0.42
	(11.43)	(14.48)	(9.40)	(12.95)	(10.67)
GH7	0.12	0.31	0.16	0.26	0.21
	(3.05)	(7.87)	(4.06)	(6.60)	(5.33)
N1	0.55	0.53	0.54	0.53	0.54
	(13.97)	(13.46)	(13.72)	(13.46)	(13.72)
N3	0.72	0.75	0.75	0.75	0.73
	(18.29)	(19.05)	(19.05)	(19.05)	(18.54)

TABLE 6.1
(CONTINUED)

WEDGE-OPENING LOAD (WOL) CRACK LENGTH CALCULATIONS

FREE CORROSION
(-435 MV SCE)

SPECIMEN	LEFT LENGTH in (mm)	CENTER LENGTH in (mm)	RIGHT LENGTH in (mm)	AVERAGE LENGTH in (mm)	INITIAL LENGTH in (mm)
S6	0.50 (12.70)	0.64 (16.26)	0.41 (10.41)	0.58 (14.73)	0.50 (12.70)
S4	0.33 (8.38)	0.48 (12.19)	0.42 (10.67)	0.45 (11.43)	0.34 (8.64)
S2	0.27 (6.86)	0.48 (12.19)	0.36 (9.14)	0.43 (10.92)	0.32 (8.13)
G2	0.37 (9.40)	0.41 (10.41)	0.15 (3.81)	0.36 (9.14)	0.26 (6.60)
G5	0.14 (3.56)	0.30 (7.62)	0.26 (6.60)	0.27 (6.86)	0.19 (4.83)
G6	0.33 (8.38)	0.46 (11.68)	0.21 (5.33)	0.40 (10.16)	0.25 (6.35)
SH4	0.24 (6.10)	0.35 (8.89)	0.20 (5.08)	0.31 (7.87)	0.23 (5.84)
SH8	0.24 (6.10)	0.34 (8.64)	0.20 (5.08)	0.30 (7.62)	0.21 (5.33)
SH5	0.20 (5.08)	0.33 (8.38)	0.18 (4.57)	0.28 (7.11)	0.20 (5.08)
GH2	0.45 (11.43)	0.36 (9.14)	0.25 (6.35)	0.36 (9.14)	0.35 (8.89)
GH9	0.34 (8.64)	0.34 (8.64)	0.17 (4.32)	0.31 (7.87)	0.26 (6.60)
GH3	0.14 (3.56)	0.30 (7.62)	0.21 (5.33)	0.25 (6.35)	0.19 (4.83)
N2	0.91 (23.11)	0.90 (22.86)	0.87 (22.10)	0.90 (22.86)	0.89 (22.61)
N4	0.22 (5.59)	0.26 (6.60)	0.23 (5.84)	0.25 (6.35)	0.22 (5.59)

TABLE 6.2

WEDGE-OPENING LOAD (WOL) STRESS INTENSITY CALCULATIONS

CATHODICALLY OVERPROTECTED-HYDROGEN GENERATING
(-1250 MV SCE)

SPECIMEN	CRACK LENGTH in (mm)	P_{arrest} lbs (N)	C_3 (a/W)	STRESS INTENSITY ksi$\sqrt{in}$ (MPa$\sqrt{m}$)
S9	1.26	10905	7.12	81
	(32.00	(48505)		(89)
S1	1.15	13173	6.19	89
	(29.21	(58594)		(98)
S7	1.14	14559	6.10	97
	(28.96	(64758)		(107)
G1	1.15	13967	6.12	94
	(29.21	(62125)		(103)
G7	1.15	14565	6.17	98
	(29.21	(64785)		(108)
SH0	1.07	12502	5.50	78
	(27.18	(55609)		(86)
SH3	1.05	14363	5.42	89
	(26.67	(63886)		(98)
SH6	1.00	16314	5.02	96
	(25.40	(72565)		(106)
GH8	1.18	11726	6.42	81
	(29.97	(52157)		(89)
GH1	1.10	14178	5.74	91
	(27.94	(63064)		(100)
GH6	1.05	15169	5.39	94
	(26.67	(67471)		(103)
N5	1.44	8875	9.25	80
	(36.58	(39476)		(88)
N6	1.29	11301	7.44	87
	(32.77	(50,267)		(96)
N7	1.04	14615	5.31	89
	(26.42	(65007)		(98)

TABLE 6.2
(CONTINUED)

WEDGE-OPENING LOAD (WOL)
STRESS INTENSITY CALCULATIONS

CATHODICALLY PROTECTED
(-1000 MV SCE)

SPECIMEN	CRACK LENGTH in (mm)	Parrest lbs (N)	C_3 (a/W)	STRESS INTENSITY ksi$\sqrt{in}$ (MPa$\sqrt{m}$)
S0	1.25 (26.67)	11415	7.04	84 (92)
S5	1.09 (27.69)	12962	5.65	82 (90)
S3	1.08 (27.43)	15248	5.57	96 (106)
G4	1.19 (30.23	11922 (53029)	6.53	84 (92)
G0	1.14 (28.96	14272 (63482)	6.08	95 (104)
G8	1.07 (27.18	15122 (67263)	5.55	95 (104)
SH9	1.09 (27.69	12376 (55048)	5.69	79 (87)
SH1	1.06 (26.92	14931 (66413)	5.47	93 (102)
SH2	1.03 (26.16	15075 (67054)	5.27	92 (101)
GH0	1.20 (30.48	11957 (53185)	6.56	84 (92)
GH5	1.28 (32.51	10961 (48755)	7.36	84 (92)
GH7	1.03 (26.16	15456 (68748)	5.21	93 (102)
N1	1.30 33.02)	10712 (47647)	7.59	84 (92)
N3	1.52 (38.61	8623 (38355)	10.55	87 (96)

TABLE 6.2
(CONTINUED)

WEDGE-OPENING LOAD (WOL)
STRESS INTENSITY CALCULATIONS

FREE CORROSION
(-435 MV SCE)

SPECIMEN	CRACK LENGTH in (mm)	Parrest lbs (N)	C_3 (a/W)	STRESS INTENSITY ksi$\sqrt{in}$ (MPa$\sqrt{m}$)
S6	1.35 (34.29	10355 (46059)	8.10	85 (94)
S4	1.22 (30.99	11910 (52976)	6.75	85 (94)
S2	1.20 (30.48	13789 (61333)	6.55	97 (108)
G2	1.13 (28.70	12707 (56521)	5.96	84 (92)
G5	1.04 (26.41	14363 (63887)	5.30	88 (97)
G6	1.17 (29.72	14269 (63469)	6.29	98 (108)
SH4	1.08 (27.43	12637 (56209)	5.58	80 (88)
SH8	1.07 (27.18	13197 (58700)	5.55	83 (91)
SH5	1.05 (26.67	15125 (67276)	5.39	93 (102)
GH2	1.11 (28.19	12772 (56810)	5.87	83 (91)
GH9	1.08 (27.43	13349 (59376)	5.62	85 (93)
GH3	1.03 (26.16	15078 (67067)	5.21	91 (100)
N2	1.67 (42.42	6159 (27395)	14.05	79 (87)
N4	1.02 (25.91	13879 (61734)	5.17	83 (91)

6.2 SLOW STRAIN RATE TESTING

Raw data from slow strain rate testing were measured from the load-deflection curves and from the initial and final diameters of the fractured specimens. As discussed in Section 5.4.1, key parameters from geometry data are the reduction of area (ROA) and the zero gage length elongation (e). These derived parameters for the 6.67×10^{-5} /sec strain rate are tabulated with the final diameters in Table 6.3 where they are separated according to the applied potential and in Table 6.4 where they are separated according to specimen type. Tables 6.5 and 6.6 present the same data for the 8.33×10^{-6} /sec strain rate. Specimens are identified in these tables by a code consisting of a single letter prefix, a single or double letter suffix and a numerical identifier. The prefixes N,S and G designate base metal, submerged arc weld (SAW) and gas metal arc weld (GMAW) materials respectively. The dual letter for the base metal (N) specimens indicates the orientation of the sample as removed from the as-received plate. The absence of a suffix for the base metal samples indicates the LT (standard) orientation. The single letter suffixes for the S and G specimens indicate weld metal (W) or heat-affected zone (H) material. The numerical identifiers serve as a means of uniquely designating individual specimens for control purposes. These identifiers were assigned to individual specimen blanks as they were saw cut from the as-received plate and hence additionally serve as a means of determining the longitudinal and through thickness location of each specimen. Plots of ROA versus potential and zero gage length elongation versus potential are shown in Figures 36 and 37 for the 6.67×10^{-5} /sec strain rate and in Figures 38 and 39 for the 8.33×10^{-6} /sec strain rate.

Load-deflection curve data include time of failure (TOF), uniform elongation, total elongation, yield strength, ultimate strength and fracture strength as discussed in Section 5.4.1 and displayed schematically in Figure 32. TOF and uniform elongation data are tabulated for the 6.67×10^{-5} /sec strain rate in Table 6.3 by applied potential, and, with the addition of total elongation, in Table 6.4 by specimen type. Tables 6.5 and 6.6 again present the same data for the 8.33×10^{-6} /sec strain rate. Plots of TOF, uniform elongation and total elongation versus potential are shown in Figures 40, 41 and 42 for the 6.67×10^{-5} /sec strain rate and in Figures 43, 44 and 45 for the 8.33×10^{-6} /sec strain rate.

The aforementioned parameters are all essentially indices to indicate the ductility of the material under test. According to Kim and Wilde [87], materials with similar mechanical properties display simple linear relationships when ductility parameters are cross-plotted. To assess data uniformity, cross-plots of TOF versus ROA, TOF versus total elongation and ROA versus total elongation are provided in Figures 46, 47 and 48 for the 6.67×10^{-5} /sec strain rate and in Figures 49, 50 and 51 for the 8.33×10^{-6} /sec strain rate.

Strain rate effects were investigated by conducting three additional experiments on SAW heat-affected zone material at three different strain rates. As shown in Table 6.7, a free corrosion test was conducted at 1.67×10^{-4} /sec and cathodically protected (-1000 mv SCE) and hydrogen generating (-1250 mv SCE) tests were conducted at 8.33×10^{-7} /sec. A plot of RDA versus strain rate for the three corrosion potentials is presented in Figure 52.

Finally, strength data for each test were extracted from the load-deflection curves and are tabulated in Table 6.8 for the 6.67×10^{-5} /sec strain rate and in Table 6.9 for the 8.33×10^{-6} /sec strain rate. Plots of yield strength versus applied potential are presented in Figures 53 and 54 for the two strain rates.

Photomicrographs of fracture surfaces were taken on a Cambridge Instruments Stereoscan 250 Mark 3 Scanning Electron Microscope (SEM). The effect of varying the applied potential to the specimens is shown in Figure 55. The classic cup and cone ductile failure under free corrosion conditions (top photomicrograph) takes on an increasingly brittle appearance as the cathodic potential is increased, as evidenced by the middle (-1000 mv SCE) and bottom (-1250 mv SCE) photomicrographs. This general behavior was seen in all five of the materials tested under all strain rate conditions. Reduced ductility under increasingly cathodic conditions is further shown by the formation of numerous secondary cracks along the gage length as seen in Figure 55 in the bottom two photomicrographs. A higher power magnification of these regions is shown in Figure 56. Ductile regions of the fracture surfaces displayed a classic ductile tear microstructure as shown in Figure 57. For the free corrosion specimens, this microstructure comprised virtually the entire fracture surface, the exception being the shear lips of the "cone" where final separation occurred. The fracture surfaces of cathodically protected and hydrogen charging specimens, on the other hand, had large areas of quasi-cleavage microstructure near the surface of the specimens. This microstructure is shown in Figure 58.

The effect of strain rate on fracture behavior was to produce a much more homogeneous fracture surface. Figure 59 shows three specimens fractured at the lower strain rate (8.33×10^{-6} /sec) at the three experimental corrosion potentials of free corrosion (top), cathodically protected (middle) and hydrogen generating (bottom). A comparison of these three fracture surfaces with those in Figure 55 which are of specimens fractured at the higher strain rate of 6.67×10^{-5} /sec reveals that significant macroscopic tearing deformation was much more prevalent in the case of the latter.

The effect of material type on the fracture behavior is shown in Figure 60, where the fracture surfaces of base metal, SAW weld metal and heat-affected zone and GMA weld metal and heat-affected zone specimens are shown. These specimens were all fractured at the higher strain rate of 6.67×10^{-5} /sec as evidenced by the macroscopic tears along the gage length at a corrosion potential of -1250 mv SCE as evidenced by the presence of secondary circumferential cracking. The only appreciable difference among the material types is that the weld metal specimens fractured relatively uniformly on the plane normal to the direction of applied stress whereas the heat-affected zone and base metal specimens fractured along a shear plane approximately 45 degrees from the direction of applied stress. There was no appreciable difference among material types at the more anodic applied potentials of -1000 mv SCE and free corrosion (-435 mv SCE).

TABLE 6.3

SLOW STRAIN RATE TESTING
POTENTIAL VARIATION DATA
(STRAIN RATE .0000667/SEC)

GAGE LENGTH = 1/2 INCH

	Df (IN)	ROA (%)	ZERO G.L ELONG.	TOF (HR)	UNIFORM ELONGATION
FREE CORROSION		-435 MV SCE			
NLT-1	0.0365	0.784	3.630	0.750	0.059
NSL-1	0.0410	0.744	2.906	0.775	0.065
SW-15	0.0425	0.718	2.546	0.863	0.064
GW-16	0.0420	0.719	2.559	0.846	0.072
SH-16	0.0410	0.734	2.759	1.030	0.105
GH-15	0.0380	0.772	3.386	0.853	0.067
ZINC-COUPLED		-1000 MV SCE			
NLT-2	0.0325	0.833	4.988	0.839	0.065
SW-14	0.0465	0.662	1.959	0.846	0.066
GW-14	0.0460	0.669	2.021	0.826	0.063
SH-14	0.0450	0.684	2.165	0.961	0.082
GH-14	0.0380	0.774	3.425	0.733	0.046
HYDROGEN GENERATING		-1250 MV SCE			
NSL-2	0.0565	0.482	0.931	0.589	0.051
SW-16	0.0625	0.390	0.639	0.633	0.062
GW-15	0.0545	0.528	1.119	0.667	0.038
SH-13	0.0575	0.404	0.678	0.958	0.113
GH-13	0.0650	0.340	0.515	0.594	0.044

TABLE 6.4

SLOW STRAIN RATE TESTING
MATERIAL PROPERTY VARIATION
(STRAIN RATE .0000667/SEC)

GAGE LENGTH = 1/2 INCH

SAMPLE	CORROSION POTENTIAL (MV SCE)	ROA (%)	TOF (HR)	UNIFORM ELONG. (%)	TOTAL ELONG. (%)
NSL-1	- 435	0.744	0.775	0.065	0.159
NLT-2	- 1000	0.833	0.839	0.065	0.175
NSL-2	- 1250	0.482	0.589	0.051	0.118
SW-15	- 435	0.718	0.863	0.064	0.173
SW-14	- 1000	0.662	0.846	0.066	0.176
SW-16	- 1250	0.390	0.633	0.062	0.125
GW-16	- 435	0.719	0.846	0.072	0.176
GW-14	- 1000	0.669	0.826	0.063	0.171
GW-15	- 1250	0.528	0.667	0.038	0.126
SH-16	- 435	0.734	1.030	0.105	0.223
SH-14	- 1000	0.684	0.961	0.082	0.204
SH-13	- 1250	0.404	0.958	0.113	0.211
GH-15	- 435	0.772	0.853	0.067	0.176
GH-14	- 1000	0.774	0.733	0.046	0.151
GH-13	- 1250	0.340	0.594	0.044	0.110

TABLE 6.5

SLOW STRAIN RATE TESTING
POTENTIAL VARIATION DATA
(STRAIN RATE .00000833/SEC)

GAGE LENGTH = 1/2 INCH

	Df (IN)	ROA (%)	ZERO G.L. ELONG.	TOF (HR)	UNIFORM ELONG.
FREE CORROSION		-435 MV SCE			
GW-1	0.0381	0.764	3.237	6.067	0.081
SH-1	0.0280	0.869	6.634	7.700	0.108
GH-1	0.0300	0.848	5.579	6.700	0.090
SW-1	0.0350	0.799	3.975	6.633	0.066
N-1	0.0310	0.840	5.250	6.200	0.075
ZINC-COUPLED		-1000 MV SCE			
GW-2	0.0505	0.575	1.353	4.333	0.054
SH-2	0.0465	0.636	1.747	5.067	0.066
GH-8	0.0591	0.433	0.764	4.517	0.056
SW-2	0.0514	0.561	1.278	5.067	0.072
N-2	0.0536	0.528	1.119	5.450	0.074
HYDROGEN GENERATING		-1250 MV SCE			
GW-3	0.0570	0.466	0.873	4.117	0.054
SH-3	0.0650	0.297	0.422	3.717	0.065
GH-3	0.0675	0.251	0.335	3.133	0.047
SW-3	0.0625	0.351	0.541	4.183	0.072
N-3	0.0670	0.281	0.391	3.667	0.072

TABLE 6.6

SLOW STRAIN RATE TESTING
MATERIAL PROPERTY VARIATION
(STRAIN RATE .00000833/SEC)

GAGE LENGTH = 1/2 INCH

SAMPLE	CORROSION POTENTIAL (MV SCE)	ROA (%)	TOF (HR)	UNIFORM ELONG. (%)	TOTAL ELONG. (%)
N-1	- 435	0.849	6.200	0.075	0.197
N-2	- 1000	0.528	5.450	0.074	0.163
N-3	- 1250	0.281	3.667	0.072	0.110
SW-1	- 435	0.799	6.633	0.066	0.185
SW-2	- 1000	0.561	5.067	0.072	0.152
SW-3	- 1250	0.351	4.183	0.072	0.125
GW-1	- 435	0.764	6.067	0.081	0.193
GW-2	- 1000	0.575	4.333	0.054	0.130
GW-3	- 1250	0.466	4.117	0.054	0.119
SH-1	- 435	0.870	7.700	0.108	0.245
SH-2	- 1000	0.636	5.067	0.066	0.152
SH-3	- 1250	0.297	3.717	0.065	0.111
GH-1	- 435	0.848	6.700	0.090	0.213
GH-8	- 1000	0.433	4.517	0.056	0.135
GH-3	- 1250	0.251	3.133	0.047	0.094

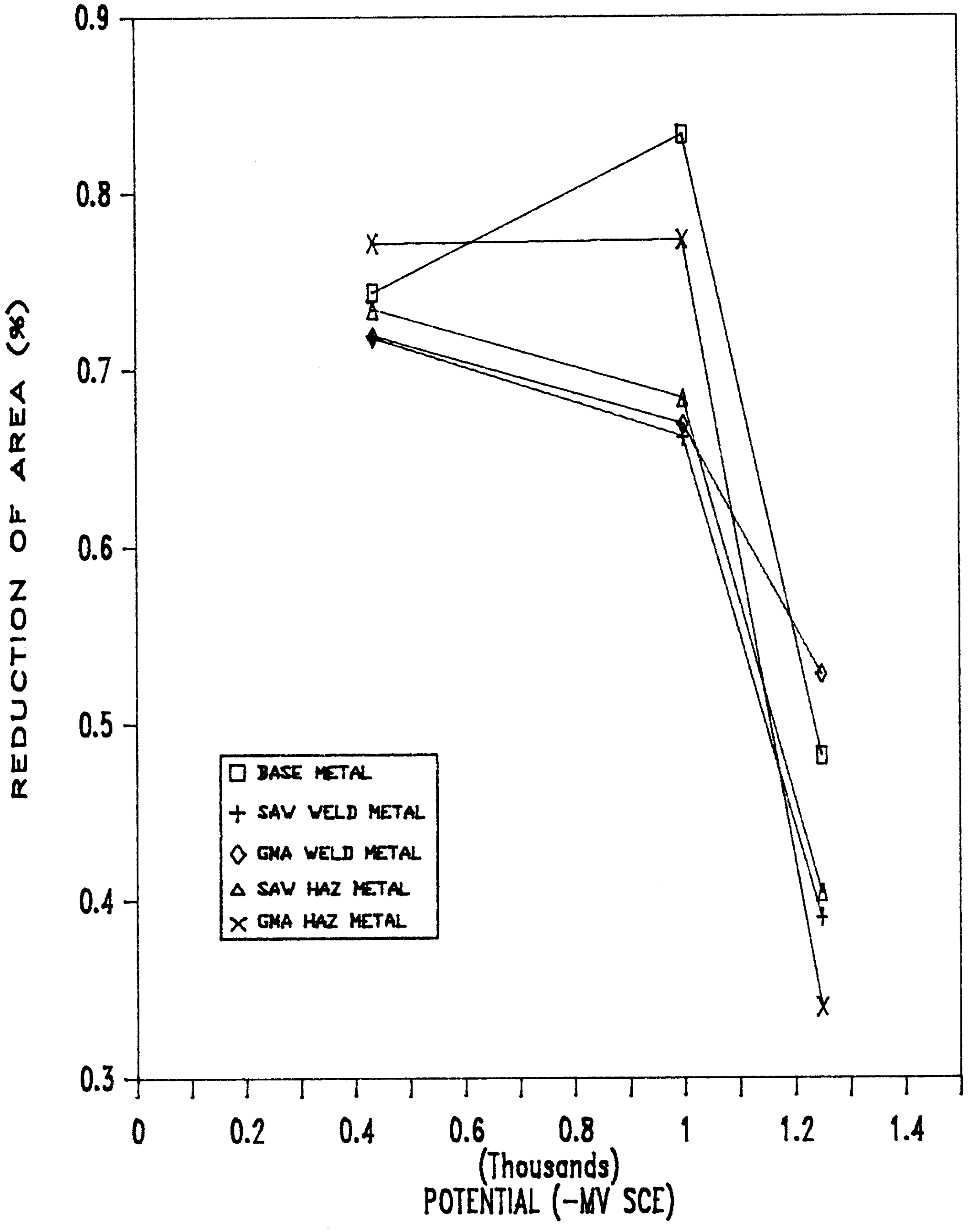

FIGURE 36 - Reduction of Area Versus Potential (Strain Rate .0000667/sec)

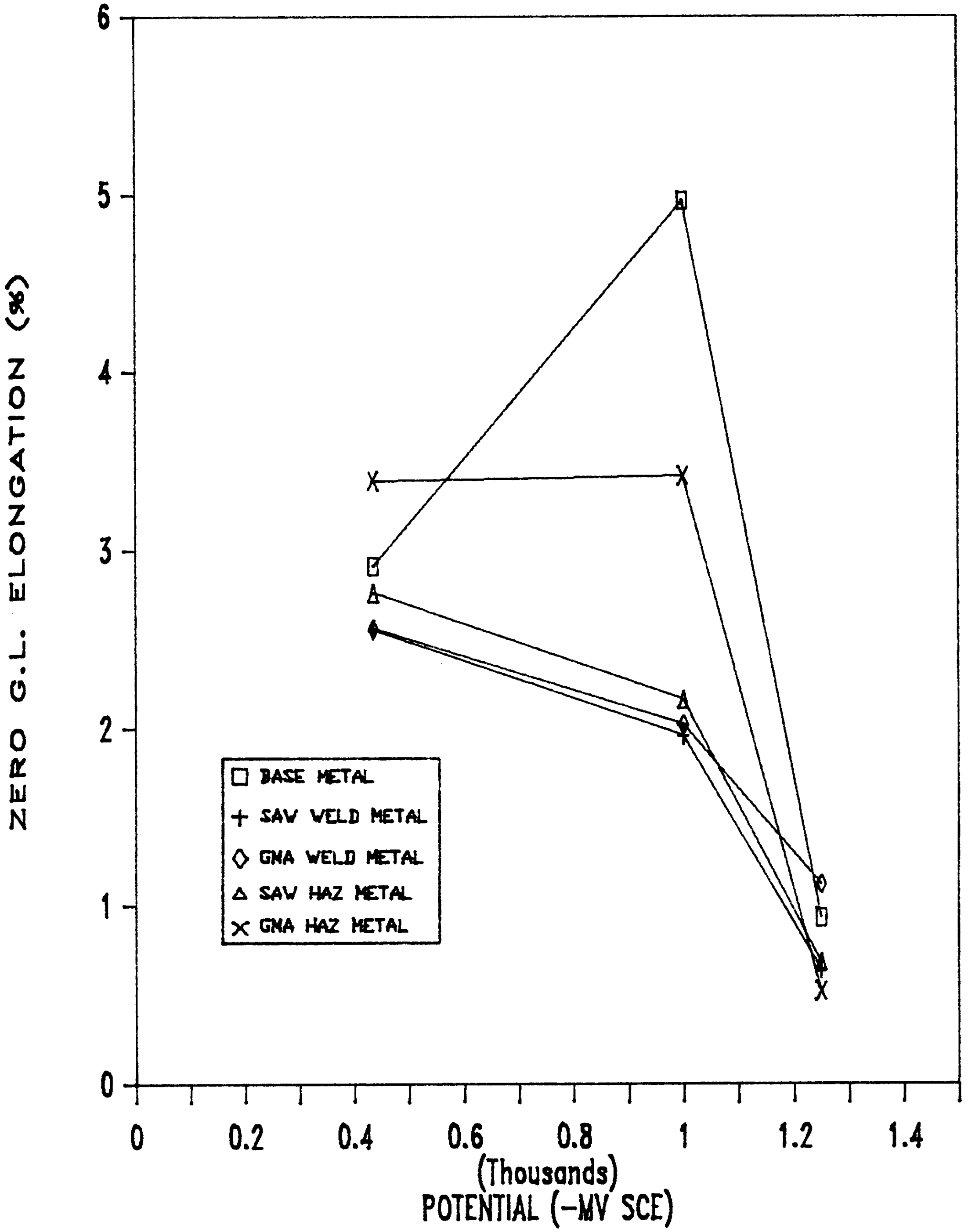

FIGURE 37 - Zero Gage Length Elongation (e) Versus Potential (Strain Rate .0000667/sec)

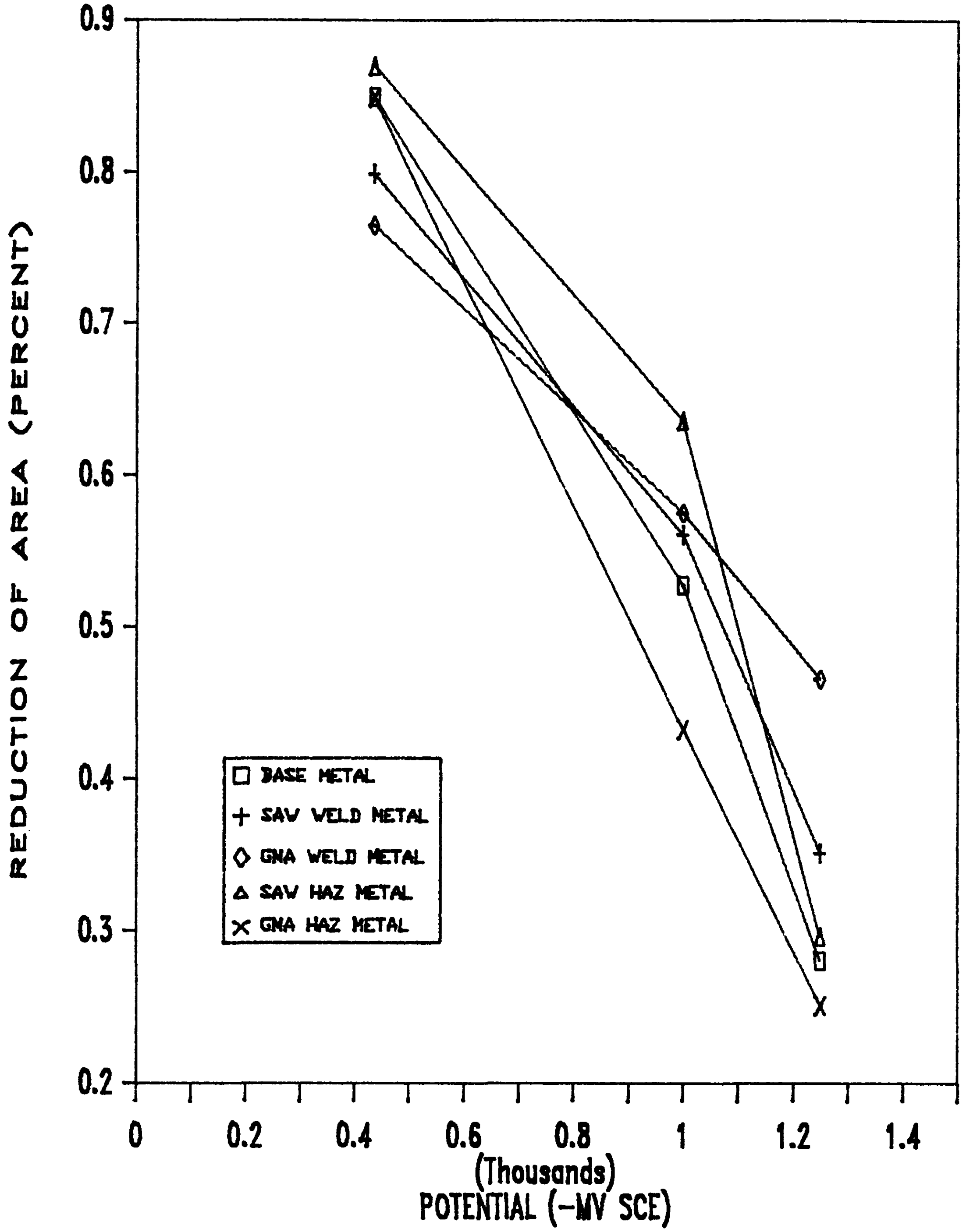

FIGURE 38 - Reduction of Area Versus Potential (Strain Rate .00000833/sec)

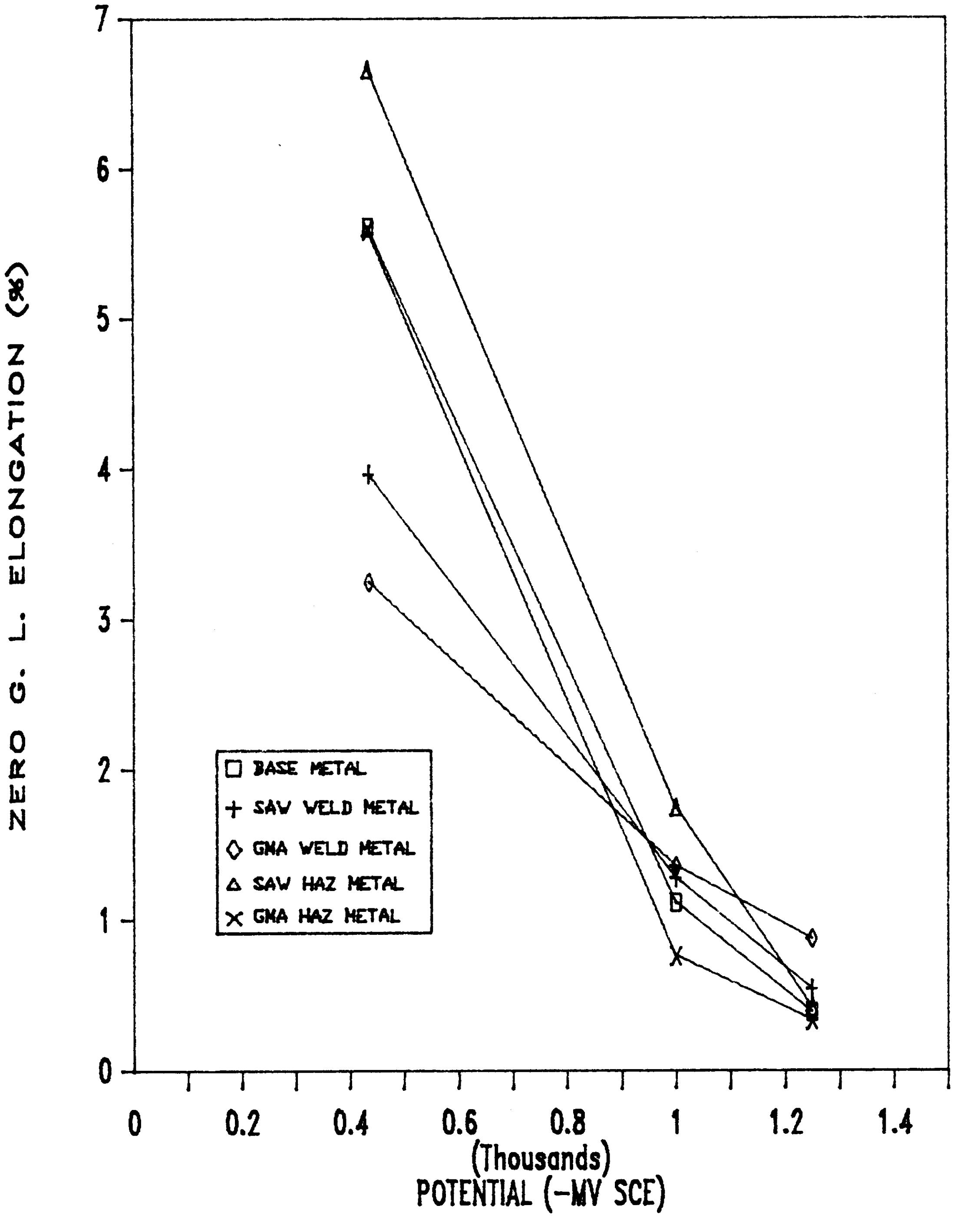

FIGURE 39 - Zero Gage Length Elongation (e) Versus Potential (Strain Rate .00000833/sec)

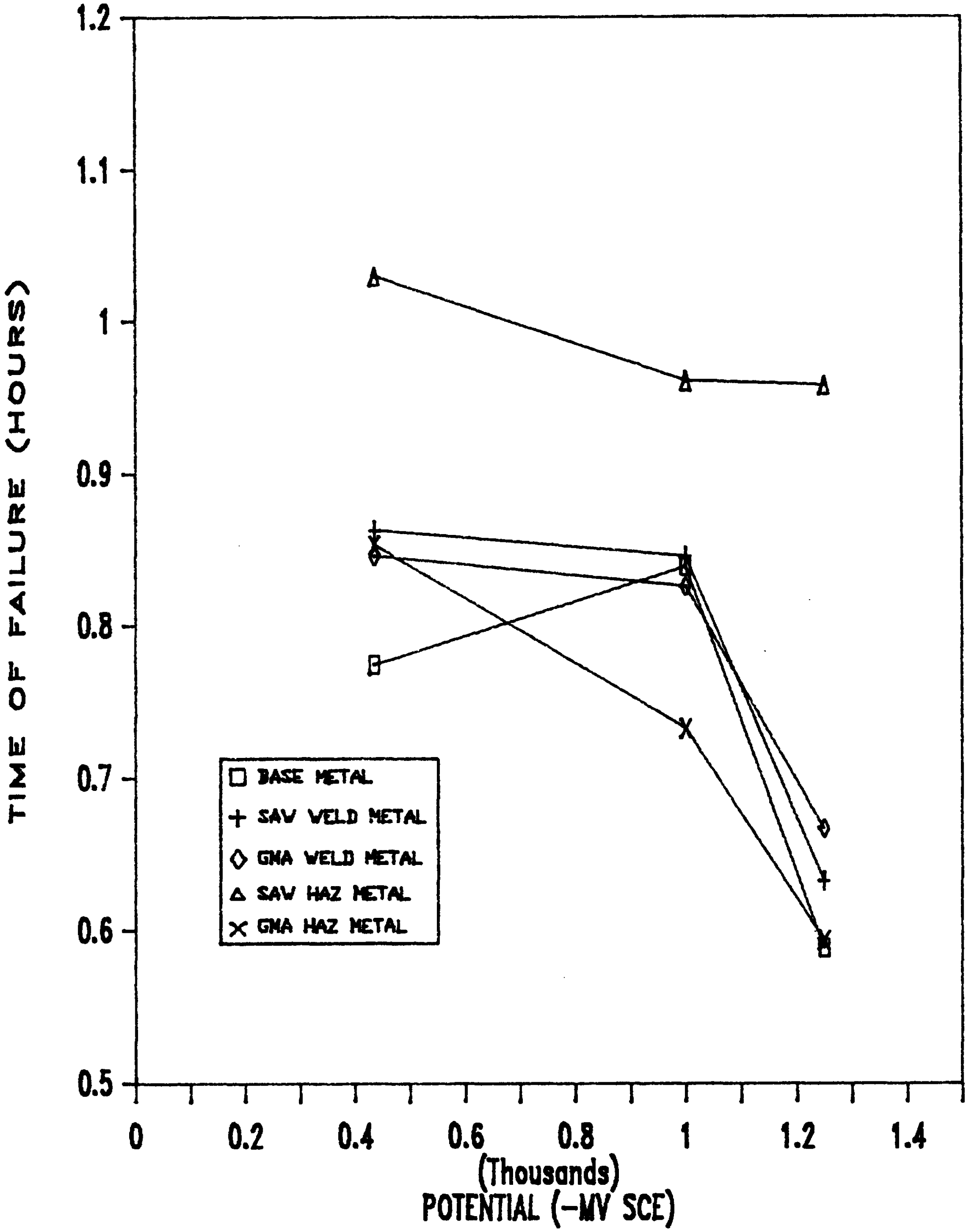

FIGURE 40 - Time of Failure Versus Potential (Strain Rate .0000667/sec)

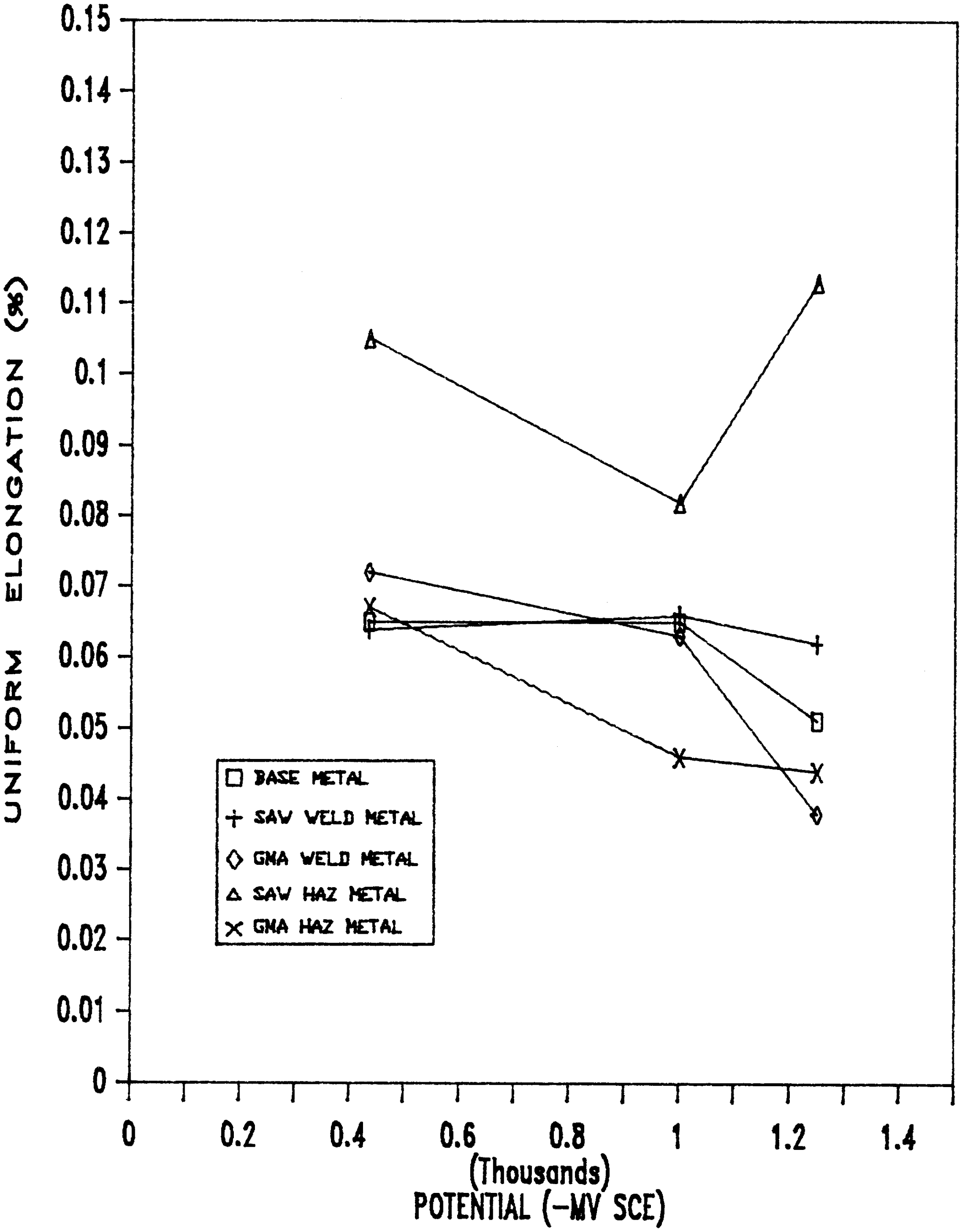

FIGURE 41 - Uniform Elongation Versus Potential (Strain Rate .0000667/sec)

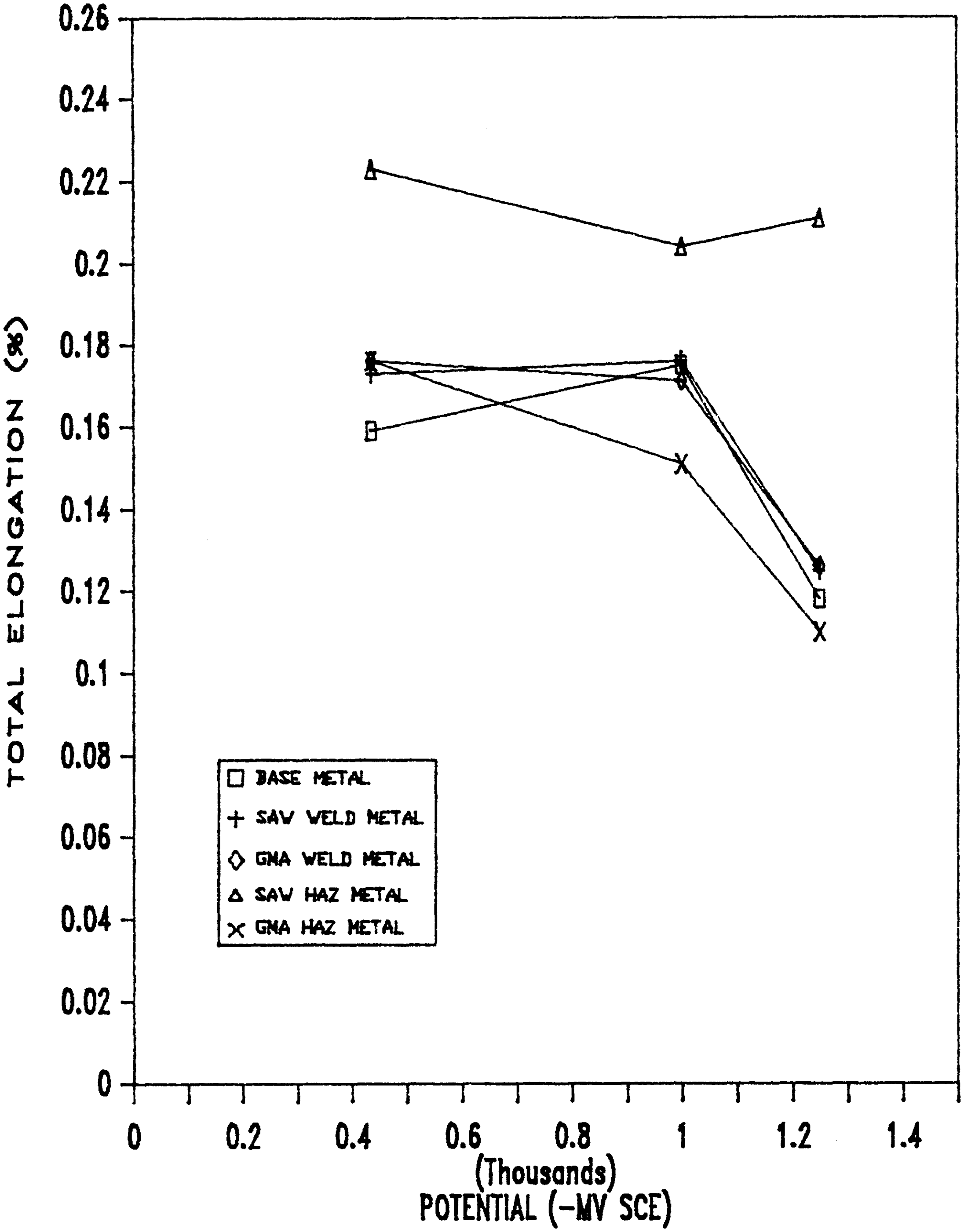

FIGURE 42 - Total Elongation Versus Potential (Strain Rate .0000667/sec)

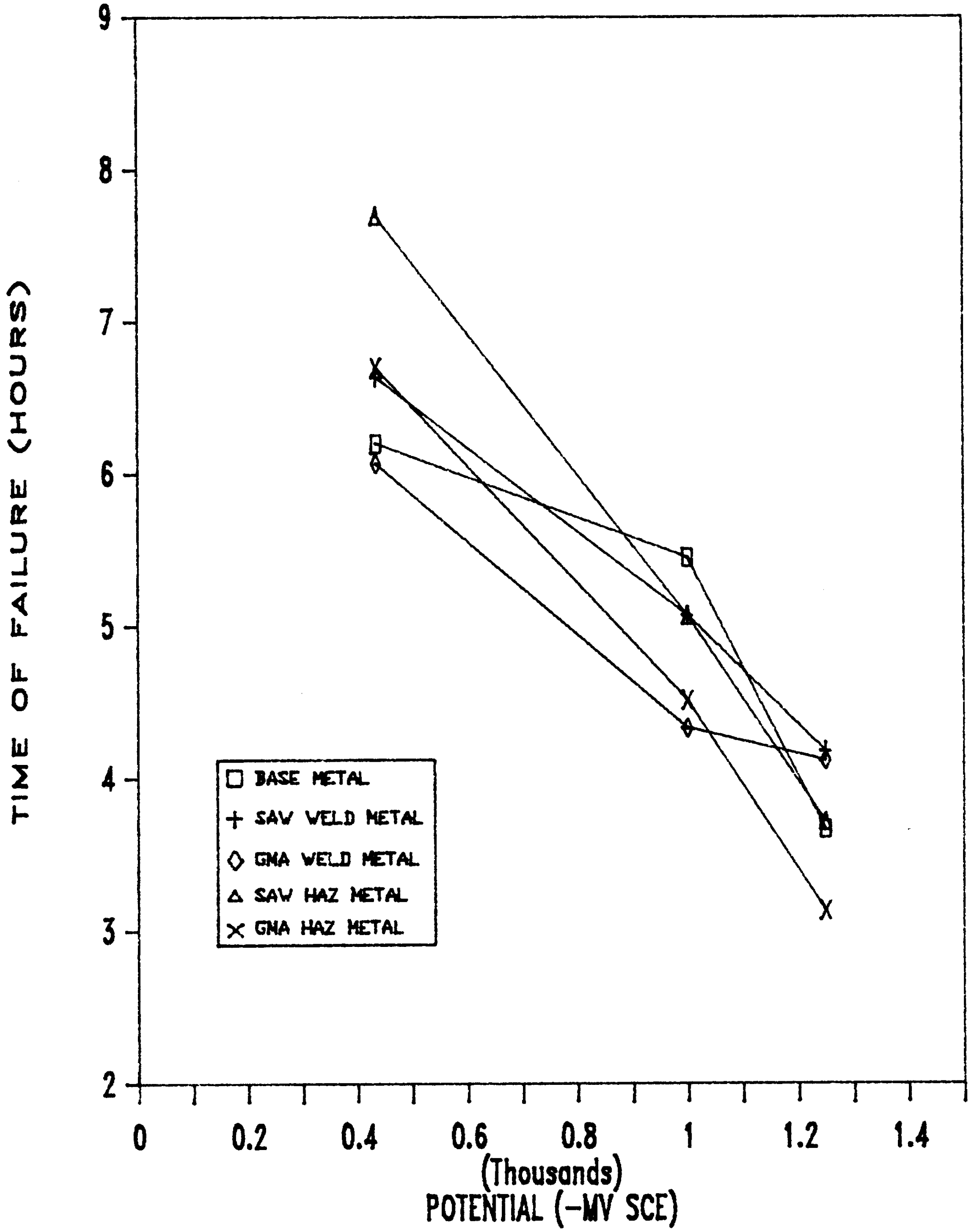

FIGURE 43 - Time of Failure Versus Potential (Strain Rate .00000833/sec)

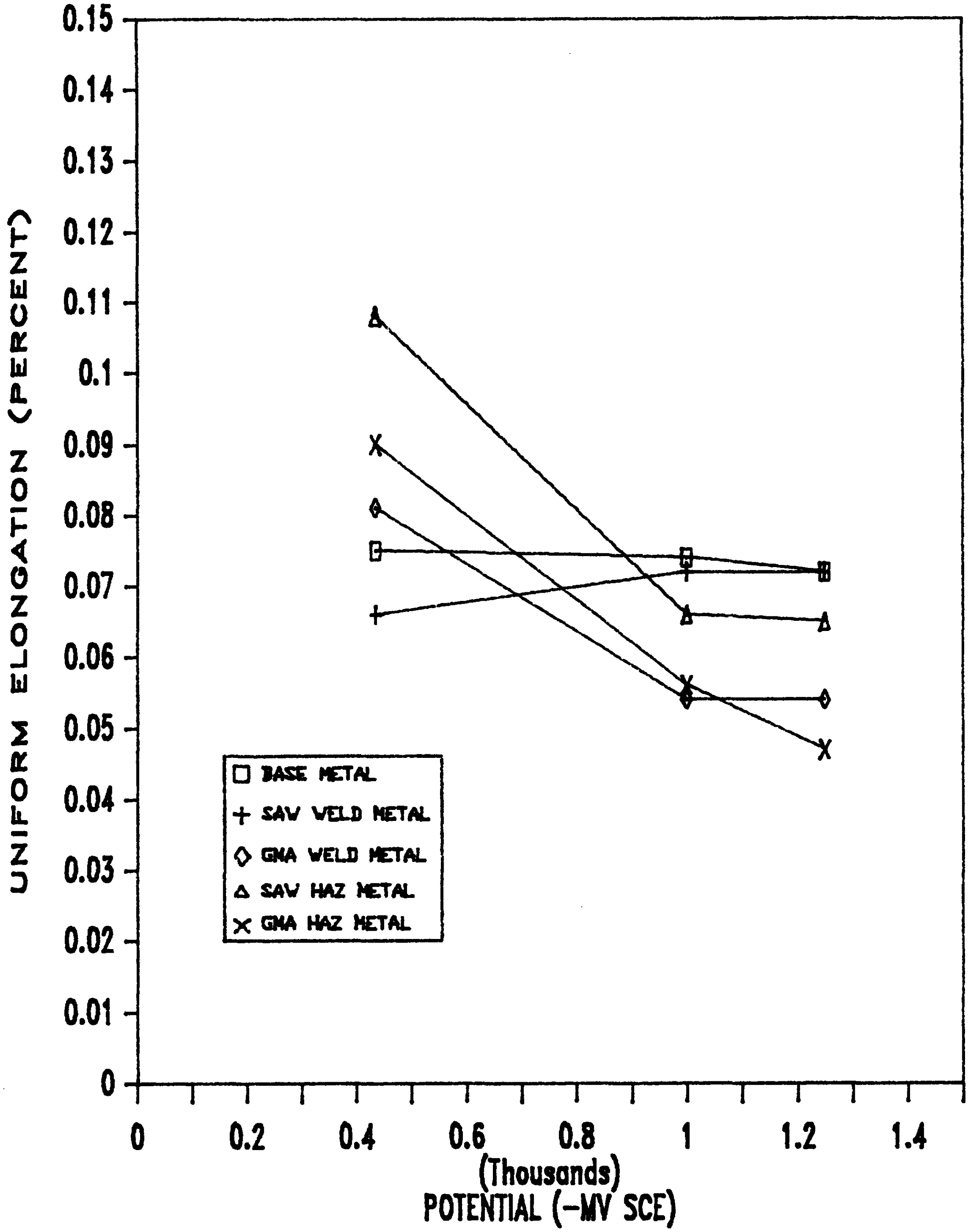

FIGURE 44 - Uniform Elongation Versus Potential (Strain Rate .00000833/sec)

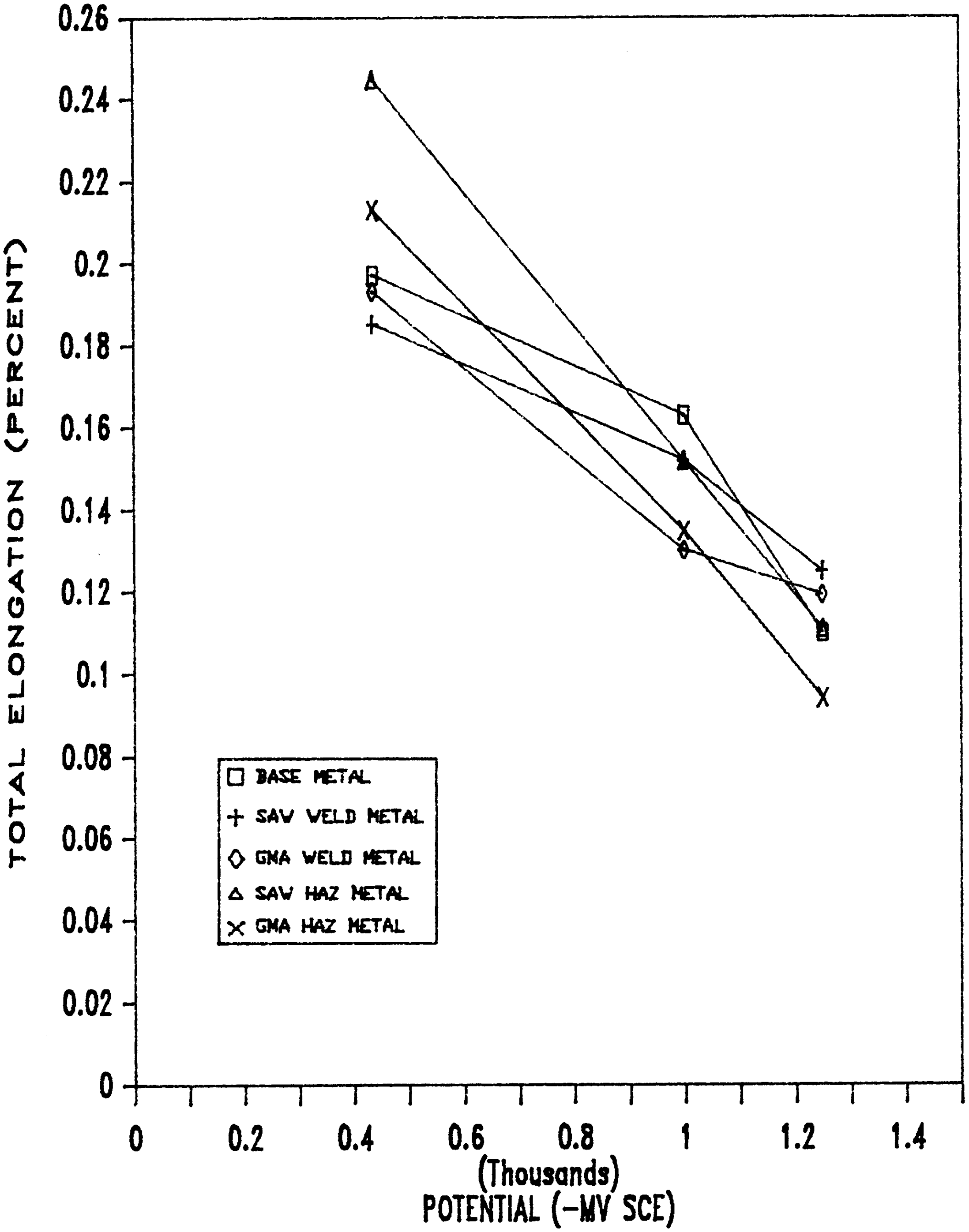

FIGURE 45 - Total Elongation Versus Potential (Strain Rate .00000833/sec)

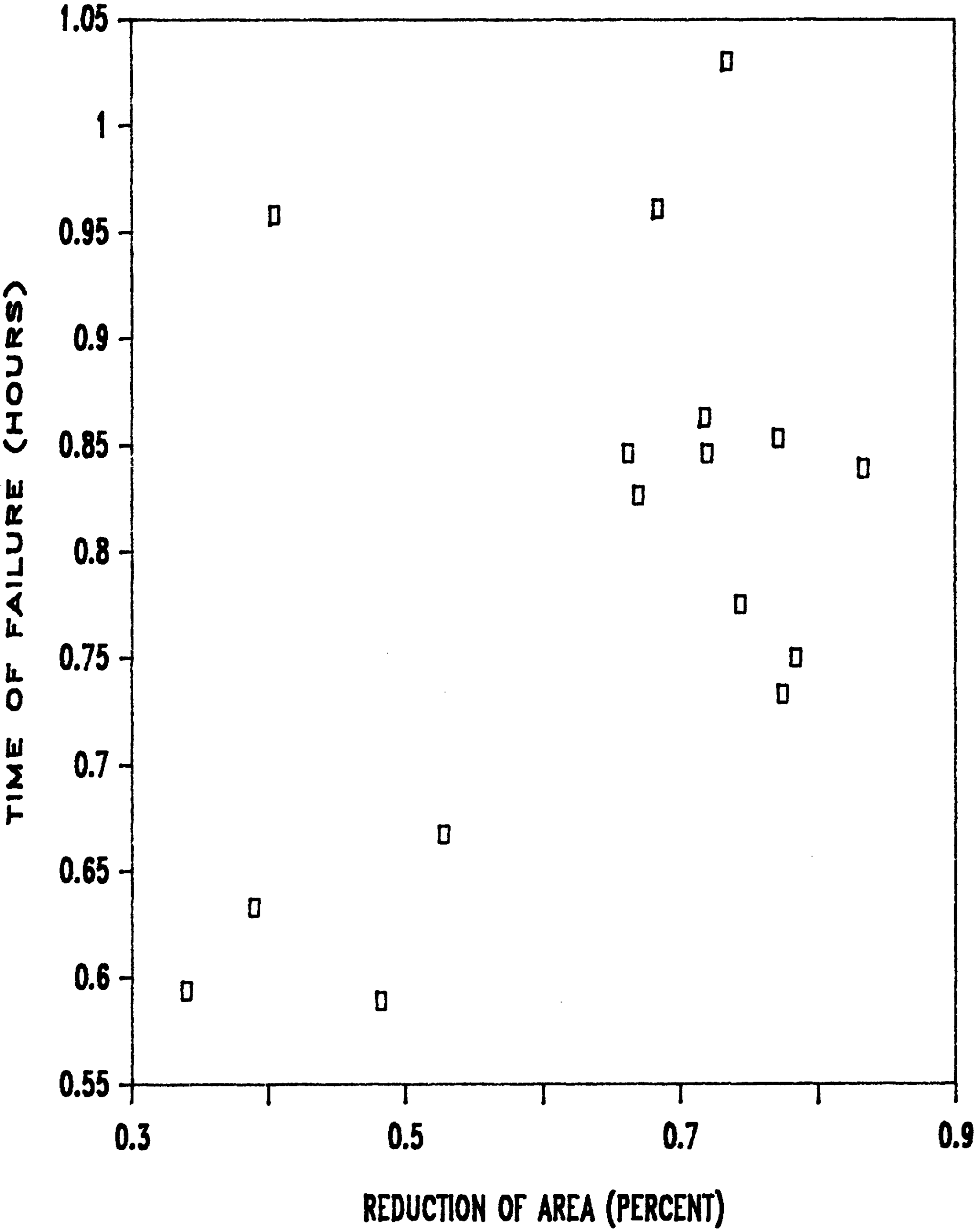

FIGURE 46 - Time of Failure Versus Reduction of Area (Strain Rate .0000667/sec)

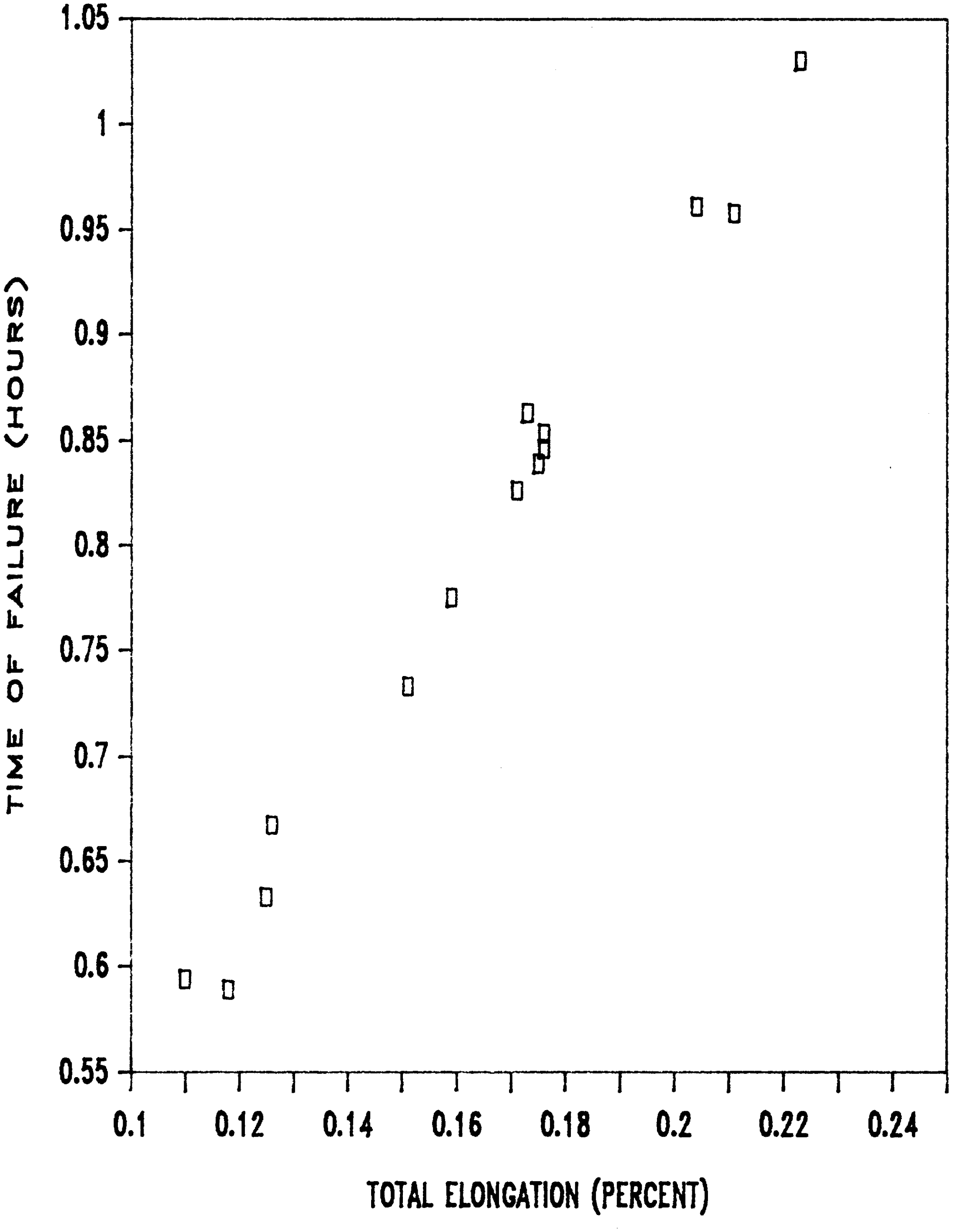

FIGURE 47 - Time of Failure Versus Total Elongation (Strain Rate .0000667/sec)

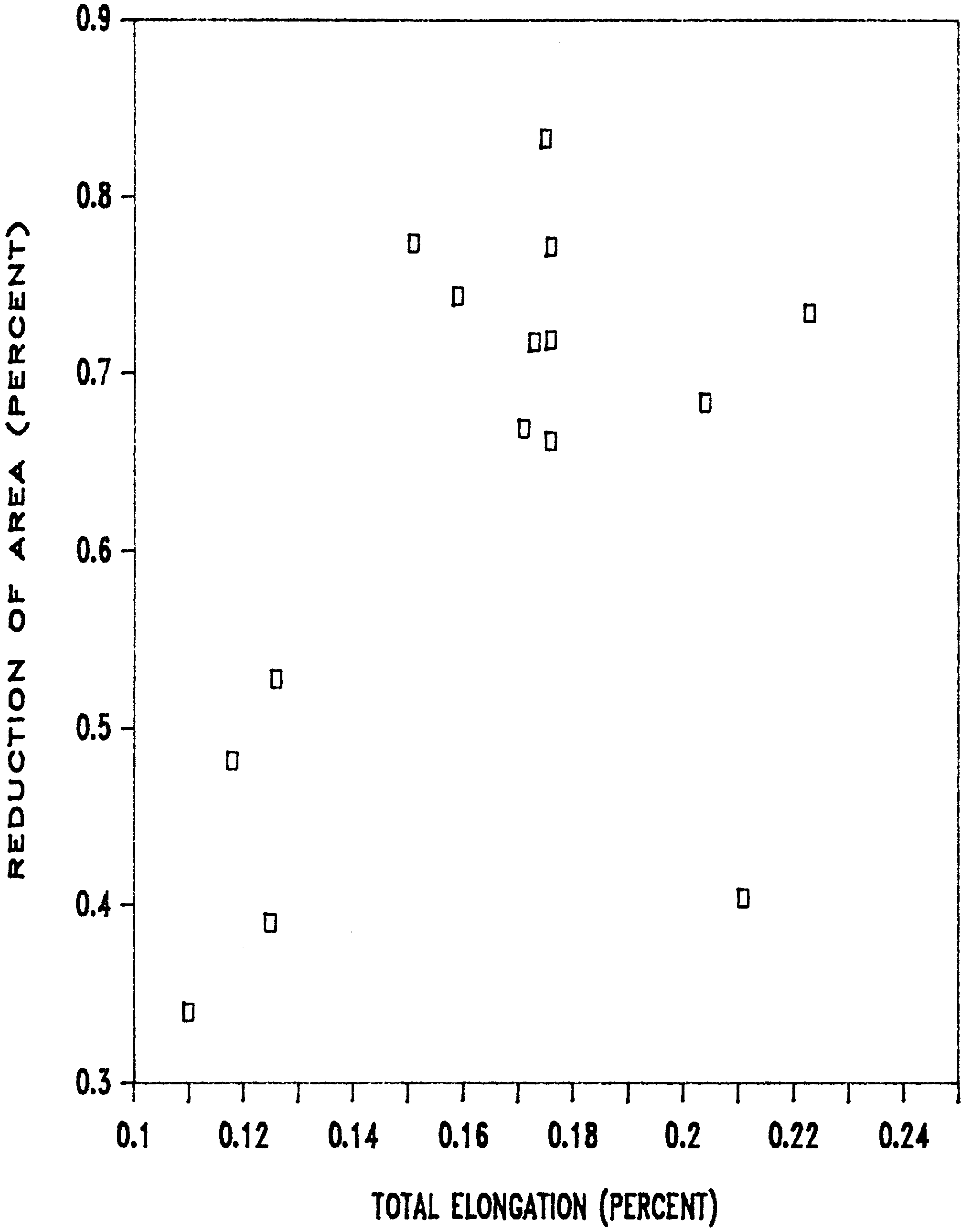

FIGURE 48 – Reduction of Area Versus Total Elongation (Strain Rate .0000667/sec)

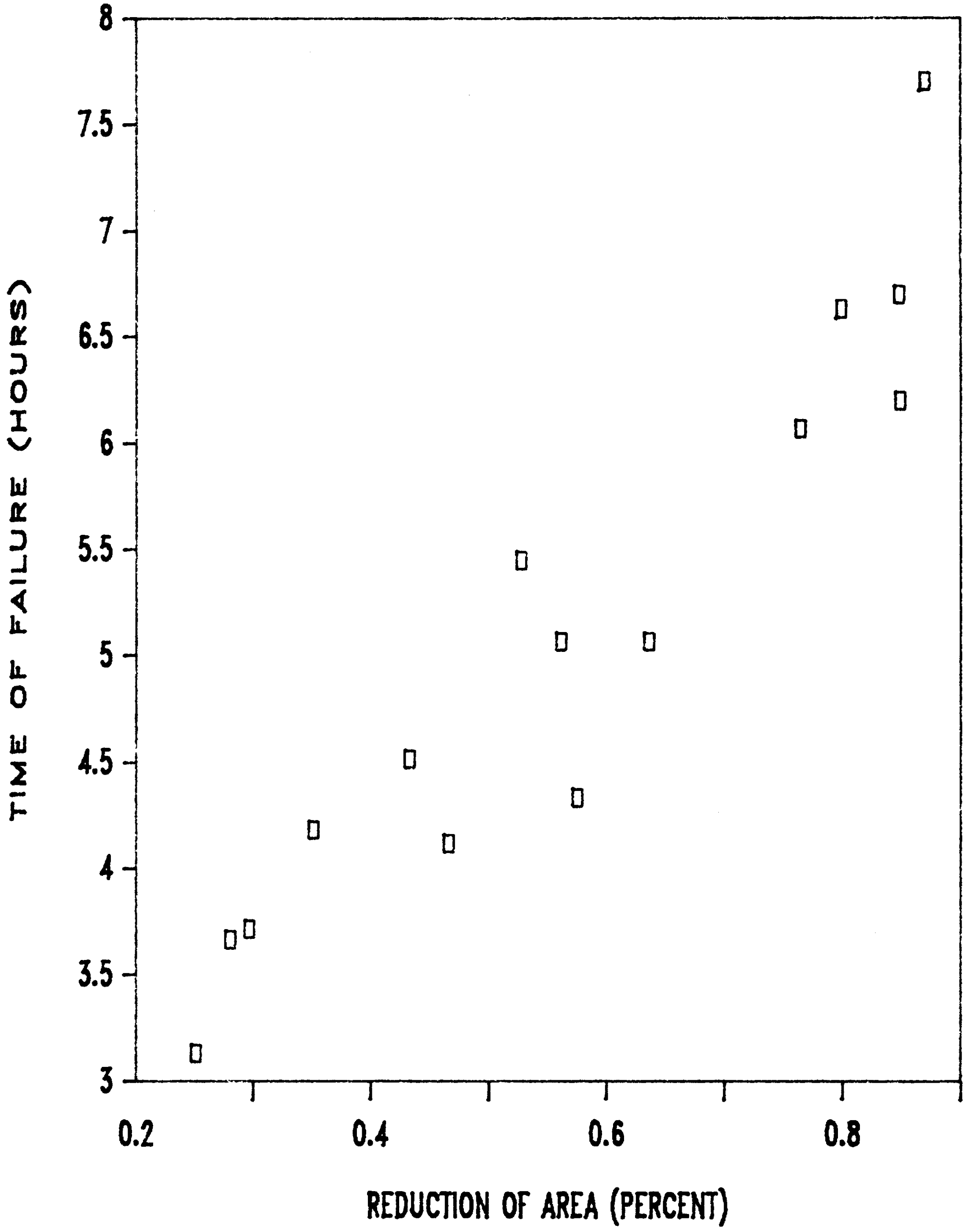

FIGURE 49- Time of Failure Versus Reduction of Area (Strain Rate .00000833/sec)

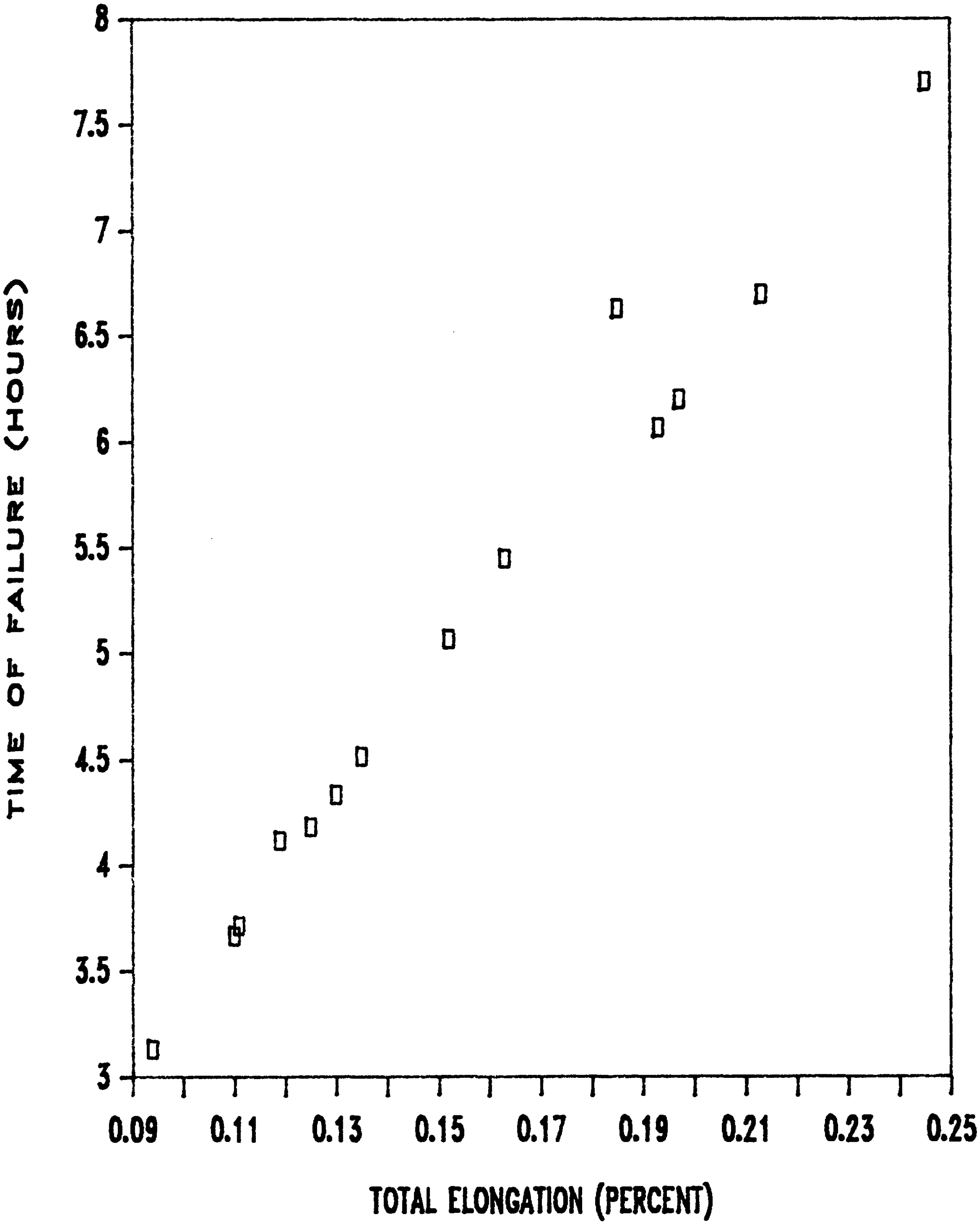

FIGURE 50 - Time of Failure Versus Total Elongation (Strain Rate .00000833/sec)

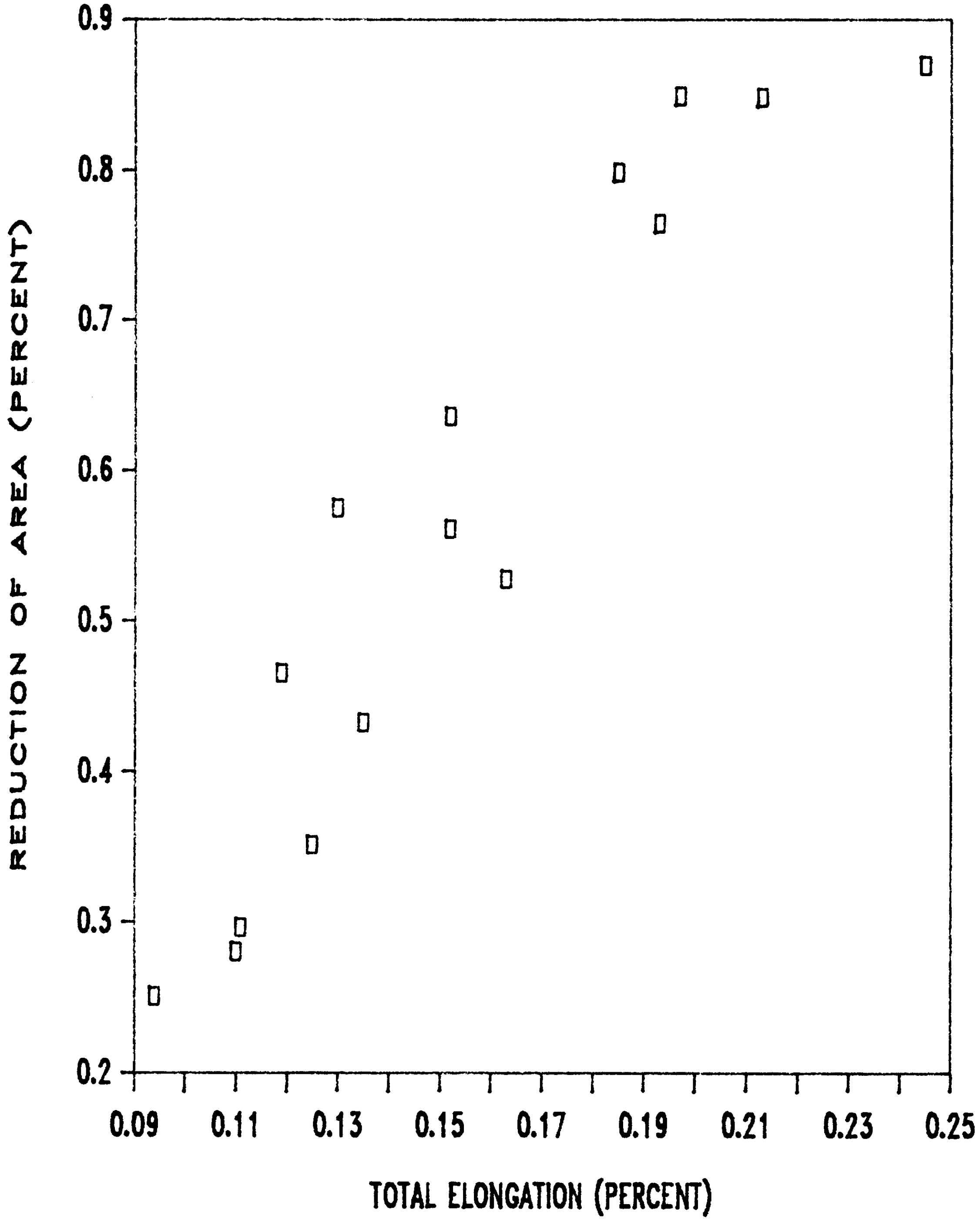

FIGURE 51 – Reduction of Area Versus Total Elongation (Strain Rate .00000833/sec)

TABLE 6.7

STRAIN RATE DEPENDENCE

FREE CORROSION (-435 MV SCE)

SPECIMEN	STRAIN RATE (1/SEC)	ROA (%)	TOF (HR)	UNIFORM ELONG. (%)	TOTAL ELONG. (%)
SH-1	8.33E-06	0.869	7.700	0.108	0.245
SH-16	6.67E-05	0.734	0.850	0.105	0.223
SH-15	1.67E-04	0.772	0.330	0.075	0.201

CATHODICALLY PROTECTED (-1000 MV SCE)

SPECIMEN	STRAIN RATE (1/SEC)	ROA (%)	TOF (HR)	UNIFORM ELONG. (%)	TOTAL ELONG. (%)
SH-5	8.33E-07	0.490	57.000	0.090	0.171
SH-2	8.33E-06	0.636	5.067	0.066	0.152
SH-14	6.67E-05	0.684	0.961	0.082	0.204

HYDROGEN GENERATING (-1250 MV SCE)

SPECIMEN	STRAIN RATE (1/SEC)	ROA (%)	TOF (HR)	UNIFORM ELONG. (%)	TOTAL ELONG. (%)
SH-4	8.33E-07	0.205	42.200	0.104	0.126
SH-3	8.33E-06	0.297	3.720	0.065	0.111
SH-13	6.67E-05	0.404	0.958	0.113	0.211

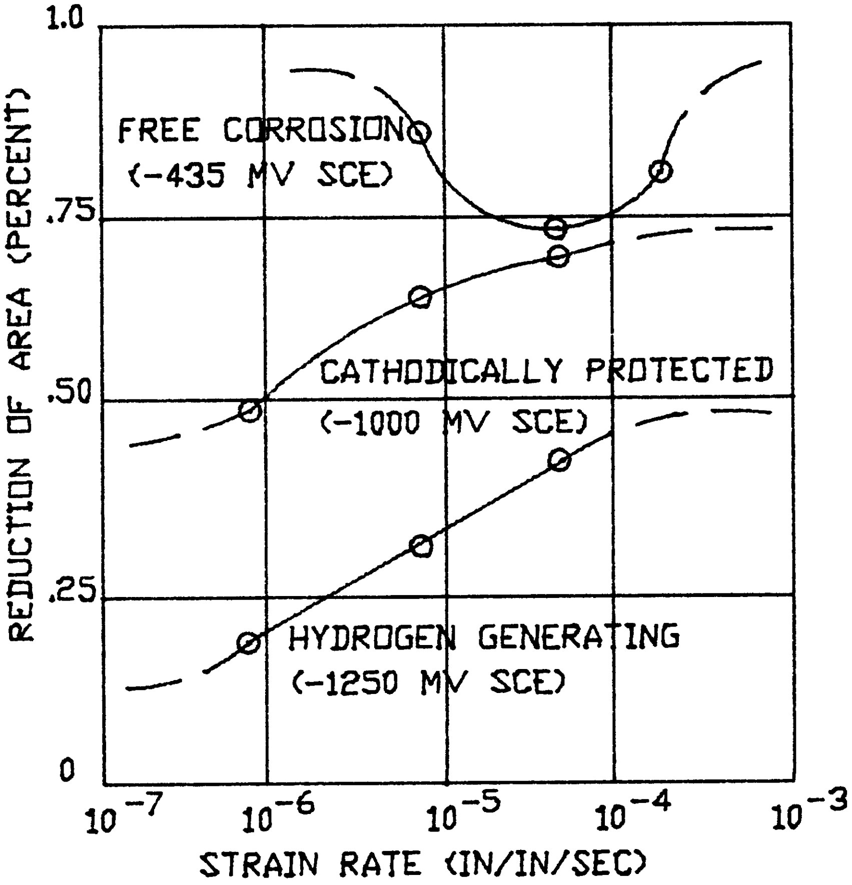

FIGURE 52 - Strain Rate Effects on Reduction of Area.

TABLE 6.8

SLOW STRAIN RATE TESTING
MATERIAL STRENGTH DATA
(STRAIN RATE .0000667/SEC)

SAMPLE	CORROSION POTENTIAL (MV SCE)	YIELD STRENGTH KSI (MPa)	ULTIMATE STRENGTH KSI (MPa)	FRACTURE STRENGTH KSI (MPa)
NSL-1	- 435	85.6	97.2	54.3
		(590)	(670)	(374)
NLT-2	- 1000	88.6	99.9	48.8
		(611)	(689)	(336)
NSL-2	- 1250	97.1	109.3	47.9
		(669)	(754)	(330)
SW-15	- 435	105.4	111.8	63.9
		(727)	(771)	(441)
SW-14	- 1000	93.7	96.5	52.3
		(646)	(665)	(361)
SW-16	- 1250	92.5	102.5	50.1
		(638)	(707)	(345)
GW-16	- 435	90.7	100.4	55.1
		(625)	(692)	(380)
GW-14	- 1000	97.5	103.8	59.7
		(672)	(716)	(412)
GW-15	- 1250	109.3	115.4	58.9
		(754)	(796)	(406)
SH-16	- 435	75.1	97.1	54.4
		(518)	(669)	(375)
SH-14	- 1000	86.9	95.3	43.8
		(599)	(657)	(302)
SH-13	- 1250	68.8	90.6	40.1
		(474)	(624)	(276)
GH-15	- 435	103.7	110.8	62.9
		(715)	(764)	(434)
GH-14	- 1000	113.4	119.2	58.7
		(782)	(822)	(405)
GH-13	- 1250	102.1	114.4	73.0
		(704)	(789)	(503)

TABLE 6.9

SLOW STRAIN RATE TESTING
MATERIAL STRENGTH DATA
(STRAIN RATE .00000833/SEC)

SAMPLE		CORROSION POTENTIAL (MV SCE)	YIELD STRENGTH KSI (MPa)	ULTIMATE STRENGTH KSI (MPa)	FRACTURE STRENGTH KSI (MPa)
N-1	-	435	91.6 (631)	105.4 (727)	56.6 (390)
N-2	-	1000	89.2 (615)	103.8 (716)	55.5 (383)
N-3	-	1250	86.1 (594)	100.2 (691)	81.6 (563)
SW-1	-	435	93.3 (643)	105.1 (725)	59.6 (411)
SW-2	-	1000	103.6 (714)	105.7 (729)	75.5 (520)
SW-3	-	1250	93.9 (647)	101.1 (697)	74.0 (510)
GW-1	-	435	86.4 (596)	105.6 (728)	64.1 (442)
GW-2	-	1000	103.2 (711)	108.5 (748)	70.0 (483)
GW-3	-	1250	94.2 (649)	100.7 (694)	69.1 (476)
SH-1	-	435	80.6 (556)	93.7 (646)	46.6 (321)
SH-2	-	1000	96.2 (663)	105.0 (724)	57.8 (398)
SH-3	-	1250	102.8 (709)	109.8 (757)	65.7 (453)
GH-1	-	435	79.2 (546)	99.2 (684)	62.9 (434)
GH-8	-	1000	89.1 (614)	105.8 (729)	58.7 (405)
GH-3	-	1250	110.1 (758)	115.9 (799)	73.0 (503)

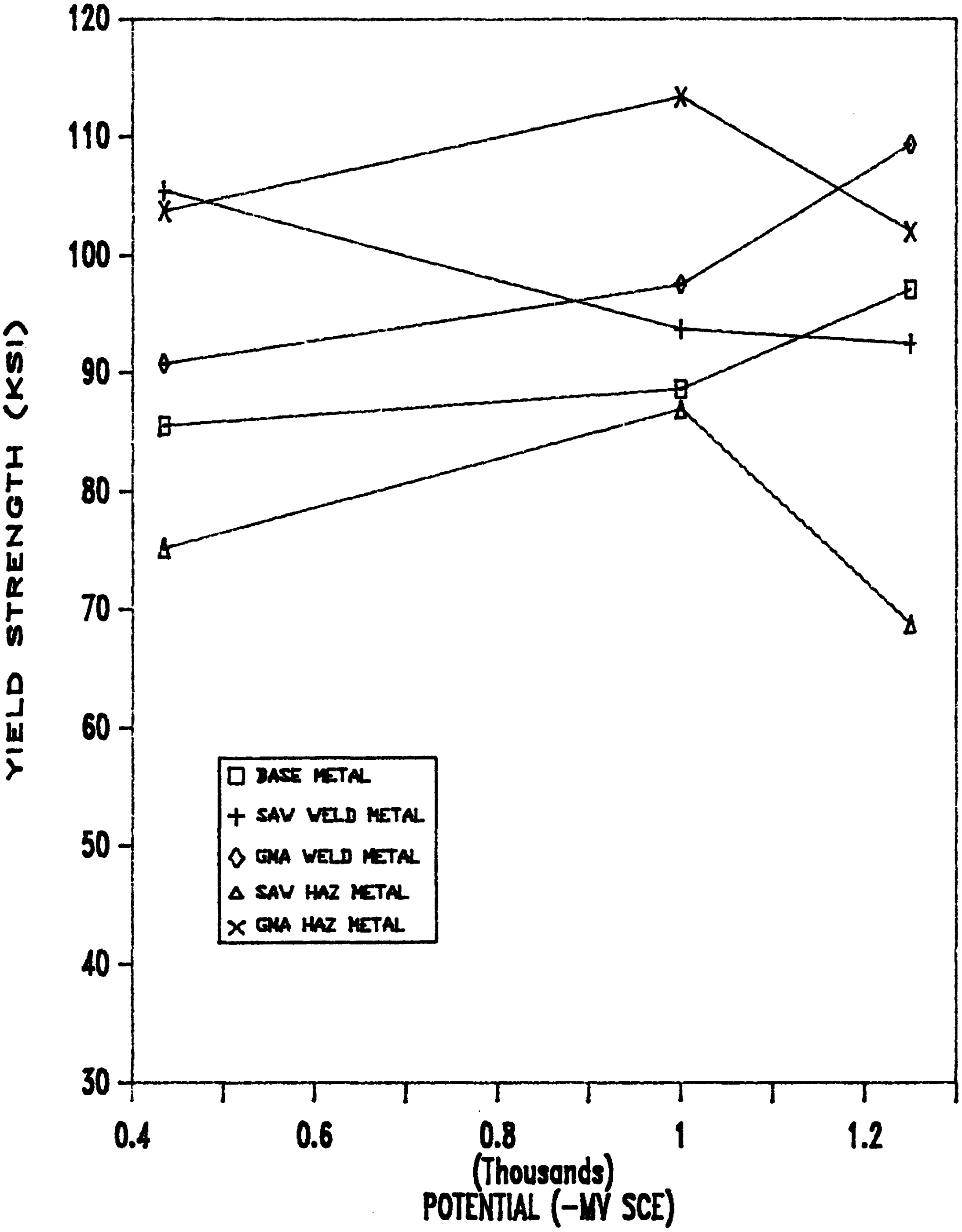

FIGURE 53 - Yield Strength Versus
Potential (Strain Rate .0000667/sec)

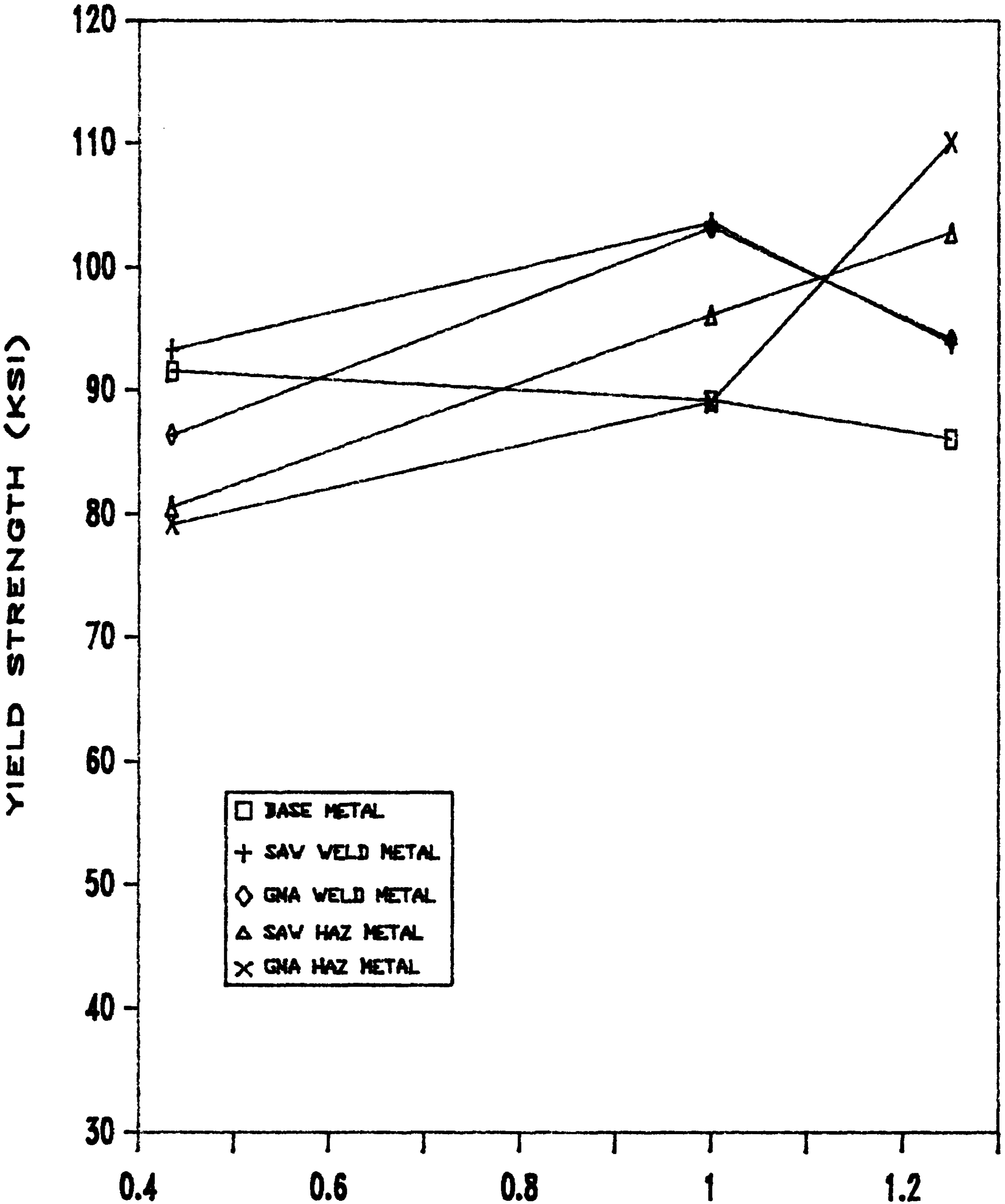

FIGURE 54 - Yield Strength Versus Potential (Strain Rate .00000833/sec)

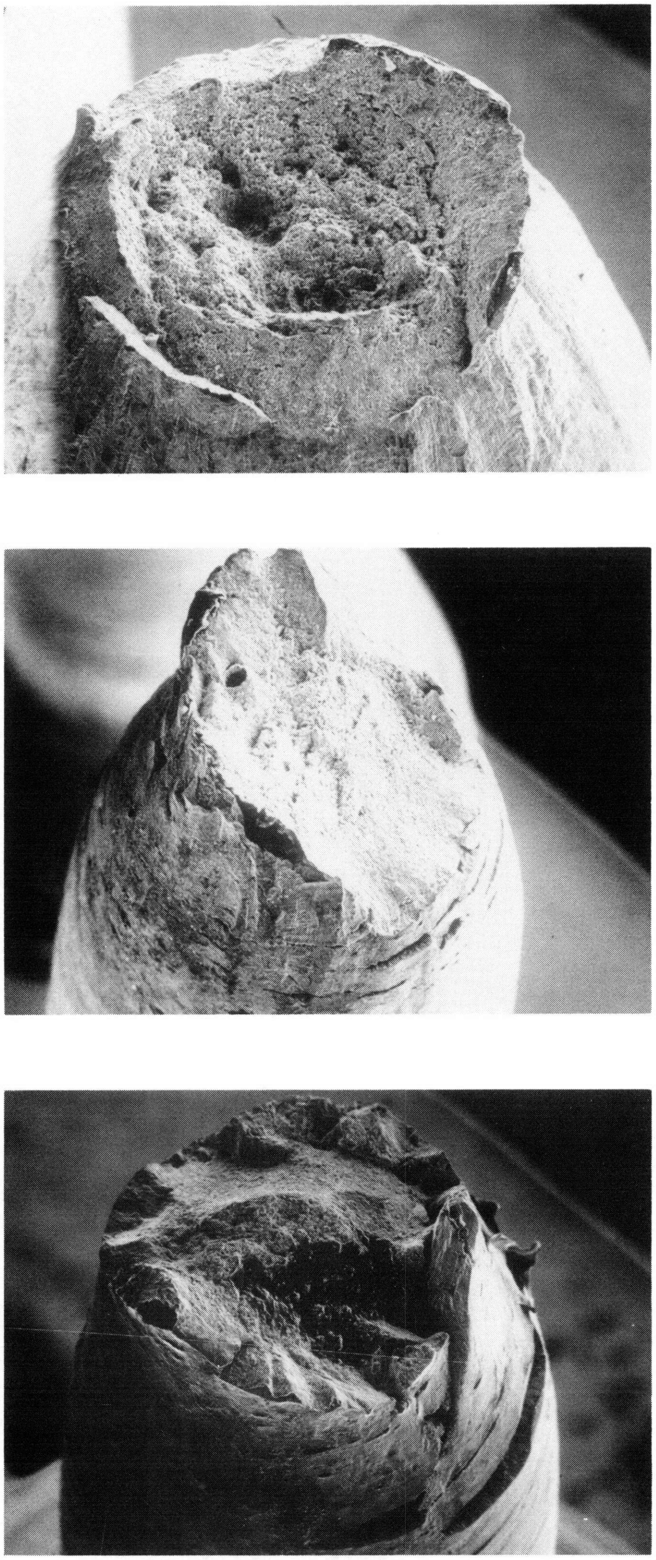

FIGURE 55 – Photomicrographs of Fracture Surfaces of GMA Weld Specimens for Free Corrosion (top, 80 X), Cathodically Protected (middle, 50 X) and Hydrogen Generating (bottom, 50 X) Showing Effects of Applied Potential (Strain Rate .0000667/sec).

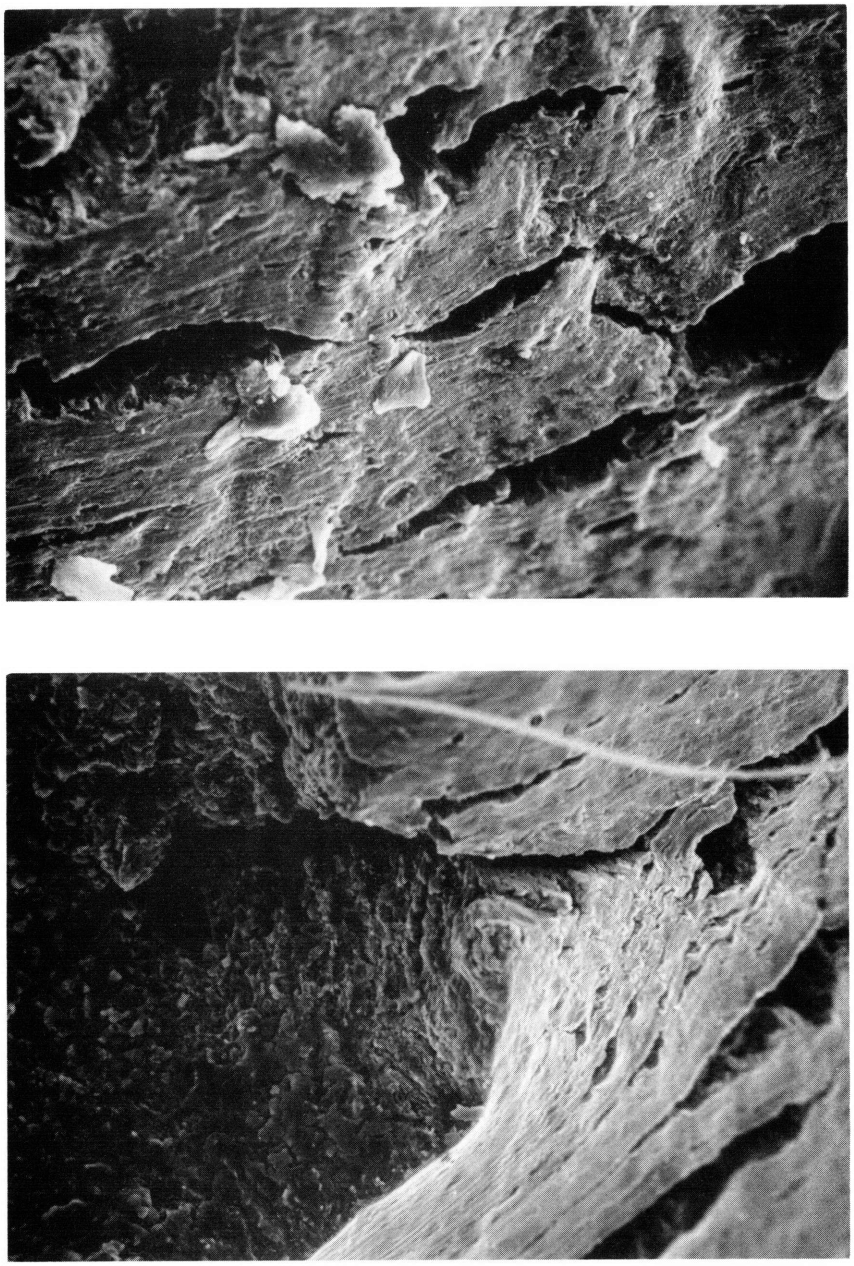

FIGURE 56 - Photomicrographs of Secondary Cracks along Gage Length (500 X).

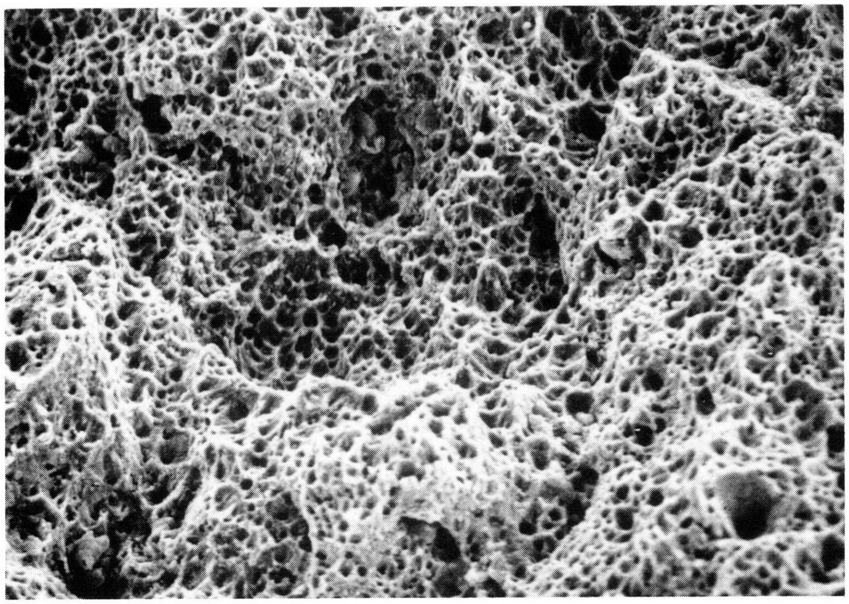

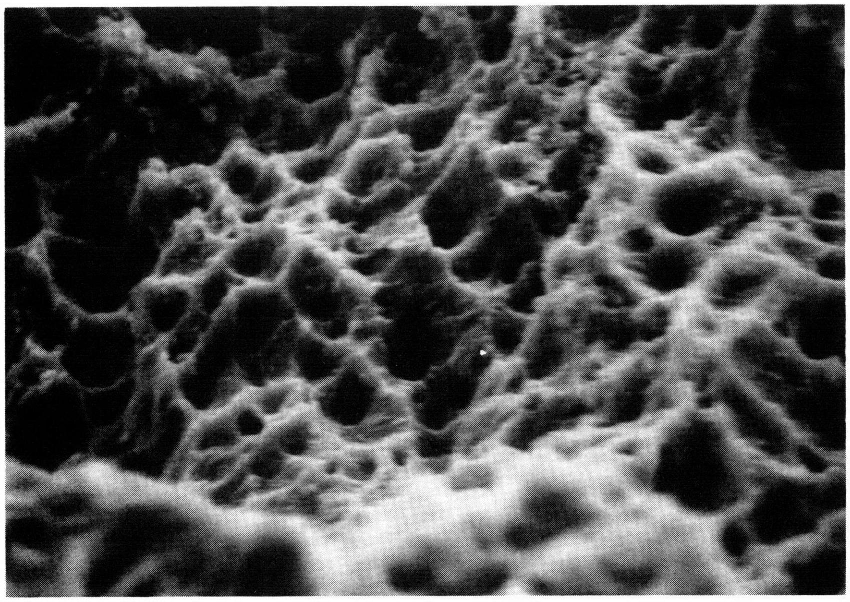

FIGURE 57 - Photomicrographs of Dutile Failure Region of Fracture Surfaces (top, 880 X; bottom, 3500 X).

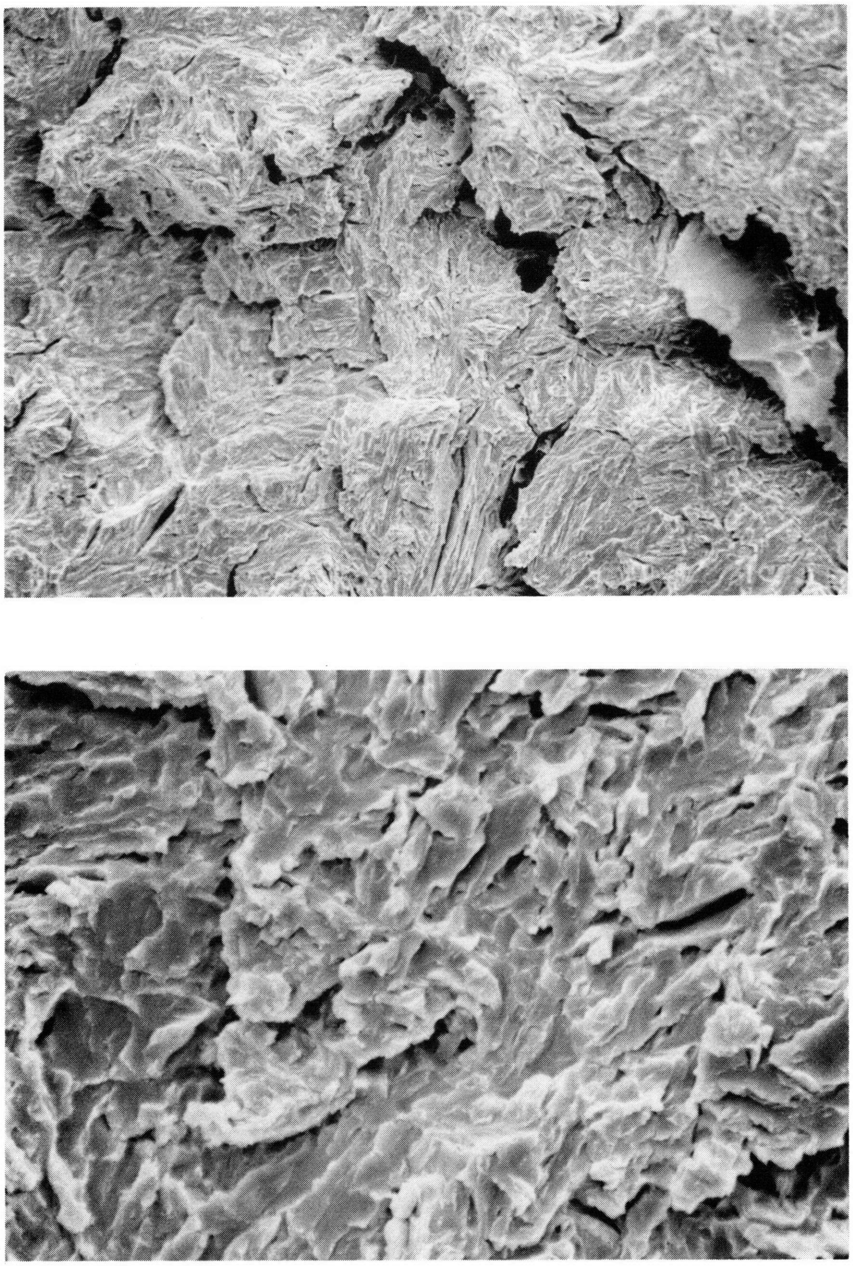

FIGURE 58 - Photomicrographs of Quasi-Cleavage Regions of Fracture Surfaces (top, 380 X; bottom 2000 X).

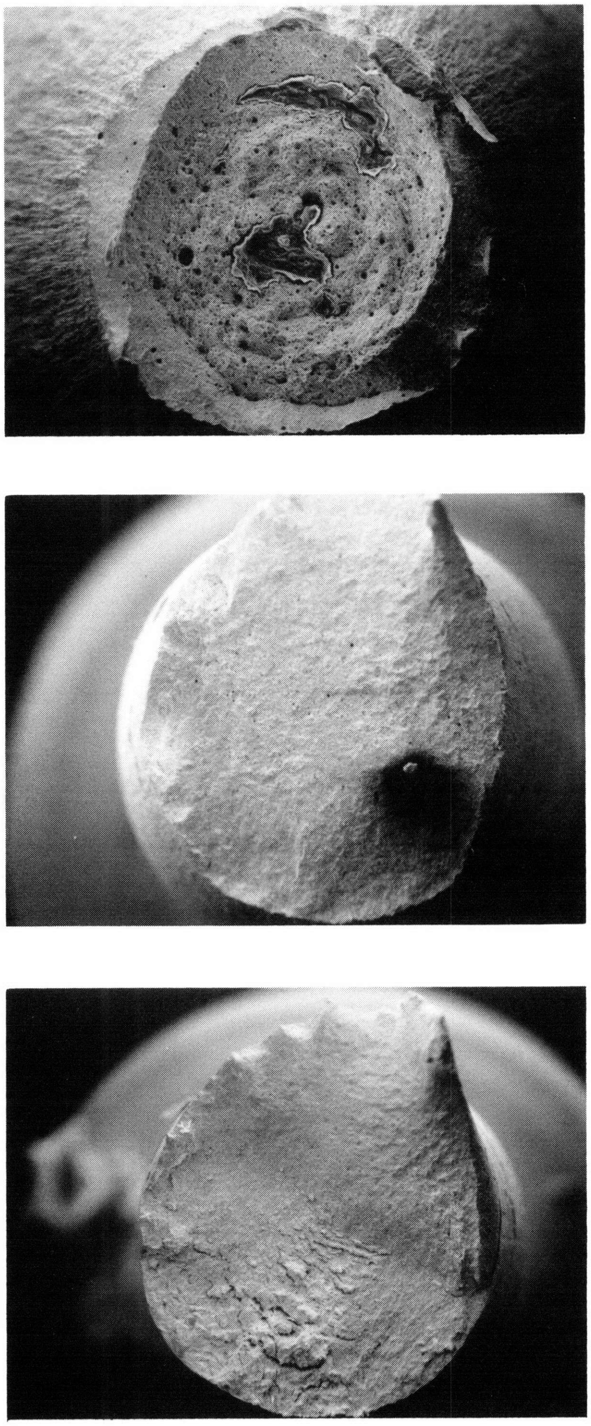

FIGURE 59 - Photomicrographs of Fracture Surfaces of GMA HAZ Specimens for Free Corrosion (top, 86 X), Cathodically Protected (middle, 45 X) and Hydrogen Generating (bottom, 36 X) Showing Effect of Strain Rate (Strain Rate .00000833/sec).

FIGURE 60 – Photomicrographs of Fracture Surfaces of Base Metal (top), GMA Weld Metal (middle left), GMA HAZ (middle right), SAW Weld Metal (bottom left) and SAW HAZ (bottom right) Showing Effect of Material (25 X). Strain Rate .0000667/sec, Applied Potential -1250 mv SCE.

7. DISCUSSION OF RESULTS

7.1 WEDGE-OPENING LOAD TEST RESULTS

The absence of any observable crack propogation in the Wedge-Opening Load specimens indicates that, for the stress intensities actually employed (i.e. those determined at the conclusion of testing by measuring the arrest load P), no stress corrosion cracking or hydrogen assisted cracking occurred. The absence of crack growth may be ascertained from the data of Table 6.1 where the average crack length measured at the conclusion of testing is tabulated along with the measured crack length after initial torquing prior to seawater immersion. It must be recalled in reviewing this data that initial crack length measurement was based on the average of the crack lengths on the two exposed faces of the specimen (the left side and the right side of Table 6.1), as the crack length at the center of the specimen was not accessible. If this average is employed as a measure of final crack length (as opposed to the weighted numerical average of Novak and Rolfe [82] used in Table 6.1 and discussed in Section 6.1) it may be seen that, of the 42 specimens tested, only 13 indicated growth. The remaining 29 indicated zero growth or negative growth which is not physically possible and reflects the limitations on the accuracy of the crack length measurement technique employed.

Further investigation of those specimens which indicated crack growth based on physical measurements with a travelling stage microscope revealed that no crack growth had actually occurred. The fracture surfaces of selected specimens were chemically stripped of oxide and observed with a stereoscopic microscope as discussed in Section 6.1. No evidence of cracking subsequent to that generated during the pretest fatigue precracking was discernible. In all of the specimens evaluated, a clear line of demarcation between the cyclic precrack fracture surface and the liquid nitrogen induced brittle fracture surface was observed with no indication of environmentally induced secondary cracking. Based on this evidence, one must conclude that apparent crack growth was also a reflection of the inherent inaccuracy of the crack length measurement technique. This conclusion is further supported by the fact that the maximum measured crack growth was only .04 inches (1.03 mm) and that most of the measured crack growths were on the order of .001 inches (.02 mm). In addition, those specimens indicating crack growth were randomly distributed among the materials, potentials and stress intensities employed in the experimental program. One would expect that, as a minimum, those specimens subjected to higher stress intensities would crack before those at lower stress intensities. The overall assessment is therefore that none of the specimens tested underwent environmentally induced cracking.

For the Wedge-Opening Load portion of the experimental program, one may then only conclude that the stress intensities actually employed for the specific material/environment combinations are lower bounds of K_{ISCC}.

In other words, since no cracking was observed at the stress intensity applied to each induvidual specimen, that required to induce cracking must be of higher magnitude. This assumes that a threshold stress intensity for stress corrosion cracking does in fact exist. As this has been reported by previous research [49] as discussed in Section 3.2.4, the existence of the K_{ISCC} material property for HSLA 80 must be assumed to be valid. Since each material/potential combination was evaluated with either two or three specimens, the maximum stress intensity achieved for the specific combination may be taken as the lower bound for the group. Further, since the applied potential appears to have no appreciable effect, these lower bounds may be grouped according to material type as follows:

(1) SAW Weld Metal	96-97 ksi$\sqrt{in}$ (106-107 MPa$\sqrt{m}$)
(2) GMA Weld Metal	95-98 ksi$\sqrt{in}$ (104-108 MPa$\sqrt{m}$)
(3) SAW HAZ Metal	93-96 ksi$\sqrt{in}$ (102-106 MPa$\sqrt{m}$)
(4) GMA HAZ Metal	91-94 ksi$\sqrt{in}$ (100-103 MPa$\sqrt{m}$)
(5) Base Metal	83-89 ksi$\sqrt{in}$ (91-98 MPa$\sqrt{m}$)

These results compare favorably with the lower bounds established by previous experimentation [49], repeated here for comparison purposes:

(1) Base Metal	93 ksi$\sqrt{in}$ (102 MPa$\sqrt{m}$)
(2) Weld Metal	93 ksi$\sqrt{in}$ (102 MPa$\sqrt{m}$)
(3) HAZ Metal	95 ksi$\sqrt{in}$ (104 MPa$\sqrt{m}$)

Although these results are for cathodically protected specimens (-1000 mv SCE), it has been demonstrated that the applied potential has a negligible effect on the K_{ISCC} material property.

The disparity between the experimental program matrix stress intensity values of Table 5.1 and those stress intensity values measured at the conclusion of testing (Table 6.2) may be attributed to two factors. The predominant cause for the disparity was that the estimate of crack length used in calculating the COD needed to apply the experimental program stress intensity was based on the arithmetic average of the crack lengths on the two faces of the specimen. Subsequent fracture of the specimen at the conclusion of testing revealed that the crack fronts were bowed such that the crack length at the center of the specimen was in almost all cases substantially larger than that of either of the two faces. Reference to Table 6.1 indicates that this disparity was on the order of .1 inch (2.6 mm). The actual crack lengths were therefore longer than those calculated by the arithmetic average. The result of this disparity was that the computation of the COD needed to give the desired program matrix stress intensity (Equation 1 of Section 5.3.1) was underestimated. Consequently, when specimens were torqued to the indicated COD, the stress intensity actually applied to the crack tip was less than that specified for testing.

The second reason for the stress intensity difference may be attributed to the method of calculation. Prior to environmental testing, the specimens were torqued based on two empirical compliance formulas (C_3 (a/W) and C_6 (a/W)) since no load data was available. Subsequent to testing, the arrest load was physically measured during the unloading process as discussed in Section 6.1. In using this load to calculate the final stress intensity (Equation 3 of Section 5.3.1), only one empirical compliance formula was required (C_3 (a/W). The final calculation was thus more accurate than the initial calculation as it was based on the actual loading of the specimen.

As a final note on WOL testing, the nature of the environmental test facility deserves some comment. The facility as originally constructed was intended to simulate flowing seawater by continuously circulating the electrolyte with an electric pump. In spite of periodic replenishments with freshly prepared synthetic seawater and one changeout of the entire electrolyte bath, the corrosion products generated by the specimens eventually clogged the circulation path, reducing flow to near stagnant conditions. Following this disruption of flow, the two seawater baths were mechanically stirred twice daily to ensure homogeneity. Since previous research has demonstrated that flowing and stagnant seawater produce essentially identical results [3], the use of both conditions for this research does not alter the experimental result.

7.1 SLOW STRAIN RATE TEST RESULTS

The results of slow strain rate testing are much more revealing in the assessment of environmental effects of seawater on HSLA than the WOL testing. The fundamental difference between the two tests is that slow strain rate testing is dynamic in that the mateial is being continuously deformed during the course of the experiment in contrast to the static loading of the WOL experiment. The absence of a preexisting crack in the slow strain rate experiments is an additional major distinction, but of less significance since the slow straining deformation process serves as a crack initiator in addition to providing the crack propogation motive force. In the absence of an artificially induce crack, preexisting flaws on the surface of the material serve as initiation sites under the application of applied stress. These preexisting flaws are then in essence precracks even though their location and specific nature (i.e. grain boundaries, inclusions and/or machine scratches) remain unknown. The fact that they lie within the bounds of the gage length of the specimen is sufficient to start the failure process.

The effect of the applied cathodic potential on the ductility of HSLA specimens is of prime importance in that low ductility increases the possibility of catastrophic brittle failure which is not acceptable for a ship hull steel. The primary indices used to assess material ductility in the slow strain rate experiment are reduction of area (ROA), time of failure (TOF) and total elongation. Zero gage length elongation (e) is a secondary index as it is derived directly from reduction of area and is hence more a normalized measure of ROA than an independent parameter. Uniform elongation is that portion of total elongation up to the point of necking and is hence a less complete measure of overall ductility than is the latter. In addition, uniform elongation is much more susceptible to variance in the specimen machining process since a specimen that is machined with a slightly reduced cross sectional area along a portion of the gage length will neck much more readily than one that is of uniform cross sectional area.

The data overwhelmingly support the thesis that increasing the cathodic potential reduces the ductility of HSLA base metal and weldments. This reduction of ductility or increase in brittleness is most clearly evident in Figure 38, where reduction of area is plotted versus potential for the slower strain rate of 8.33×10^{-6}/sec. All five of the materials tested showed a nearly linear drop as potential was cathodically applied from the free corrosion state of -435 mv SCE to the hydrogen generating potential of -1250 mv SCE. The change in reduction of area is substantial, amounting to about a sixty percent drop over the .8 volt range for which data were accumulated. The other primary ductility indices indicate the same behavior. Again this is most clearly evident from the data generated during the slower strain rate testing. Figure 43 shows an equally uniform forty percent decrease in time of failure with increasing cathodic potential, while Figure 45 shows a fifty percent decrease in total elongation. Although there are some minor differences among the material types (e.g. the SAW and GMA weld metal specimens are somewhat less affected than heat-affected zone or base metal specimens), the degrading effect of the applied cathodic potential on ductility is a characteristic of the HSLA/seawater system.

Given that increasing the applied cathodic potential embrittles HSLA, the fundamental question centers on the cause of this observed effect. This is the very same fundamental question addressed in the preceding theoretical discussions of stress corrosion cracking (SCC) and hydrogen assisted cracking (HAC). This question is whether the observed loss of ductility is due to the active path corrosion (APC) of SCC or the hydrogen embrittlement (HEM) and subsequent cracking of HAC. If the traditional means of distinction is employed, then the failure mode is clearly HAC since the application of a more cathodic potential reduces ductility as evidenced by the TOF and ROA data. However, since no experiments were conducted with anodically polarized test specimens to determine ductility behavior in the more noble regime, SCC cannot unequivocally be ruled out on this basis alone. In the current series of slow strain rate experiments, hydrogen was intentionally generated by making the specimen the cathode. Under these electrochemical conditions active path corrosion cannot physically occur and hence SCC may be ruled out as a cause for reduced ductility. This electrochemical relationship was demonstrated in Figure 2 (Section 2) where increasing the cathodic potential is shown to favor the formation of hydrogen and discourage metal dissolution. It may therefore be concluded that hydrogen assisted cracking was the operative mechanism for reduced ductility.

The thesis that HSLA base metal and weldments are susceptible to HAC is challenged by the lack of any observable cracking in the WOL specimens subjected to the hydrogen generating cathodic potential of -1250 mv SCE. Hydrogen bubbles were in fact observed to emanate from the surface of the WOL specimens over the course of the experiment. There are several possible explanations for this apparent anomaly. First, the geometry of the precracked WOL specimens was radically different from that of the slow strain rate specimens in that a relatively long and isolated crack front was present in the case of the former. As discussed in Section 2 [9], the constriction in crack geometry can lead to radically different environmental conditions at the crack tip from those imposed on the surface of the specimen. Specifically, when an active potential is imposed on the surface of the specimen, the crack tip is more noble due to the potential drop along the high resistance immobile electrolyte between the crack faces. It is therefore entirely possible that hydrogen was not being generated in the immediate vicinity of the crack tip and that the relatively stagnant conditions of the electrolyte precluded sufficient migration to induce hydrogen assisted cracking.

A second possible explanation for the lack of observable hydrogen assisted cracking in the WOL testing is that the static nature of the applied load did not meet the dynamic plastic deformation requirements for hydrogen/metal interaction. According to the Plastic Deformation Theory of Beachem [42], hydrogen aids in the deformation of the metal matrix (Section 2.3). In the absence of plastic deformation, hydrogen generated by the electrochemical conditions will migrate to the region of highest triaxial stress but will have no appreciable effect on the cracking process. Although this notion is at odds with the Lattice Decohesion Theory of Troiano [40] and the Stress Sorption Theory of Petch and Stables [33], it is well supported experimentally. This research, in identifying HAC in the plastically deforming slow strain rate experiment and its absence in the static WOL experiment supports the Plastic Deformation Theory.

Photomicrographic evaluation of the slow strain rate fracture surfaces lends further support to the hydrogen assisted cracking thesis. It is clear from Figure 55 and 59 that the macroscopic appearance of the fracture surfaces is markedly different as the potential is decreased. In that the three cathodic conditions are direct measures of the availability of hydrogen at the crack front, the increase in potential may be taken as the effect of hydrogen on the fracture behavior. The onset of HAC may be recognized by both macroscopic differences in fracture behavior and by microstructural changes of the fracture surface. From the macroscopic standpoint, the cup and cone appearance of the free corrosion specimen takes on a distinct brittle appearance under the influence of hydrogen. The onset of HAC is also marked by the appearance of secondary circumferential cracking shown at higher magnification in Figure 56. These secondary cracks were evident on all specimens subjected to the hydrogen enriched -1000 mv SCE potential and the hydrogen generating -1250 mv SCE potential whereas they were absent on the free corrosion specimens.

From the microscopic standpoint, HAC was manifested by the onset of the quasi-cleavage mode of failure around the periphery of the fracture surface. The free corrosion specimen fracture surfaces were characterized by the dimpled microstructure of monotonic overload fracture shown in Figure 57. The cathodically protected and hydrogen generating fracture surfaces were characterized by a quasi-cleavage microstructure adjacent to the surface of the specimen (Figure 58) with the dimpled microstructure of Figure 57 in the center. This fracture mode corresponds to medium stress intensity HAC as identified by Beachem [42] and shown in Figure 9. That the dimpled microstructure is due to monotonic overload and not the high stress intensity microvoid coalescence shown in Figure 9 is not entirely certain. Clearly, as the cross sectional area of the specimen is reduced by necking under constant load, a monotonic overload situation will eventually occur as stress increases. The possibility exists that a transition between quasi-cleavage HAC and microvoid coalescence HAC occurs as stress intensity increases with crack length prior to reaching the overload situation. Hence the dimpled microstructure could in fact be partially due to microvoid coalescence HAC and partially due to monotonic overload. However, since the dimpled microstructure of the hydrogen generating and cathodically protected specimens is identical in appearance to that of the free corrosion specimens fractured in the absence of hydrogen, it is more probable that monotonic overload predominates. As a final point, the fact that the quasi-cleavage region in those specimens subjected to a more negative hydrogen generating potential (-1250 mv SCE) was larger than that for those specimens subjected to the cathodically protected potential (-1000 mv SCE) further supports the quasi-cleavage HAC mode.

The effects of hydrogen on fracture behavior may also be seen in comparing the changes in uniform elongation with total elongation over the potential range investigated. Referring to Figure 44 for uniform elongation and Figure 45 for total elongation, it may be noted that there is a substantial decrease in the latter with increasing cathodic potential whereas the former is relatively unchanged. To explain this behavior, it may be recalled from the discussion of hydrogen cracking (Section 2.3) that it is universally accepted [40,33,42] that hydrogen migrates to regions of high triaxial stress. Uniform elongation is measured only up to the point of necking and hence involves limited if any triaxial stress. Under these monotonic stress conditions, hydrogen migration is limited and hence no hydrogen effect is evident. Total elongation, on the other hand, includes the triaxial stress conditions following necking. As the hydrogen is drawn to the stressed region, it aids in the deformation process so as to cause cracking and premature failure. Thus, total elongation is less for the hydrogen generating potentials due to HAC>

Strain rate effects were investigated by conducting several experiments at strain rates other than the two primary tests at 6.67 X 10^{-5} /sec and 8.33 X 10^{-6} /sec which were conducted on all specimen types. On a macroscopic qualitative basis, comparison of the fracture surfaces in Figures 55 and 59 (which are for the two full strain rate tests) reveals that the slower strain rate presents a much more homogeneous appearance than does the faster strain rate. At 6.67 X 10^{-5} /sec there is a great deal of macroscopic tearing whereas at 8.33 X 10^{-6} no such tearing exists. The data extracted from final specimen geometry and from the load-deflection curves for the two strain rates also reflect this homogeneity for the slower strain rate. Comparison of Figures 36, 40, 41 and 42 (6.67 X 10^{-5} /sec) with Figures 38, 43, 44 and 45 (8.33 X 10^{-6} /sec) makes this point graphically clear. Cross plots of the key ductility parameters (ROA, TOF and total elongation) for the two primary strain rates in Figures 46 through 51 provide an additional graphical indication. For the slower strain rate (Figures 49 through 51) there is a nearly linear relationship between parameters whereas for the faster strain rate (Figures 46 through 48) there is a considerable degree of data scatter.

The overwhelming evidence of increased homogeneity at the lower strain rate is evidence of a single operative failure mode, the faster strain rate indicating a combined failure mode. Based on the thesis of quasi-cleavage HAC as the failure mode, it is proposed that the slower strain rate provided adequate time during the deformation process for hydrogen migration and lattice interaction so that the single HAC failure mode was observed. The faster strain rate, on the other hand, did not provide adequate time for migration and interaction and hence the failure mode was a combination of HAC and monotonic overload. This notion is supported by photomicrographic evidence in that the slower strain rate fracture surfaces were observed to have more extensive regions of quasi-cleavage than those at the faster strain rate. In that the tests conducted at even slower strain rates of 8.33×10^{-7} /sec did not indicate any marked change from data at 8.33×10^{-6} /sec, one may conclude that strain rates on the order of 10^{-6} /sec provide the most severe conditions for environmental cracking, which is consistent with the findings of previous research [87].

The effect of strain rate on ductility provides an indication of the operative failure mode [87]. As discussed in Section 5.4.1 and shown in Figure 31, lowering the strain rate does not improve the ductility if the operative failure mode is HAC whereas ductility increases at lower strain rates for SCC failure. Referring to the data of Table 6.7 and the plot of ROA versus strain rate in Figure 52, it is clear that lowering the strain rate for the cathodically protected (-1000 mv SCE) and hydrogen generating (-1250 mv SCE) enviroments did not improve the ductility (in fact, it was degraded somewhat). This observation provides an additional indication that HAC was the operative failure mode at these two applied potentials. In the case of free corrosion, it can be seen (Figure 52) that ductility was much higher and that there is some indication of a minimum ductility at $6.67 \text{ X } 10^{-5}$ /sec. This minimum may be attributed to data scatter, as no evidence of SCC was found in these specimens during photomicrographic evaluation.

Material effects may be evaluated in terms of either composition (i.e. base metal, weld metal or heat-affected zone) or in terms of process (i.e. Gas Metal Arc Weld or Submerged Arc Weld). From the compostional standpoint, it was shown in Section 3.3.1 (Table 3.10) that the heat-affected zone yielded the highest Knoop hardness readings followed by the intermediate hardness of the weld metal and the lower hardness base metal. The strength data of Table 6.9 plotted in Figure 54 support the direct relationship between hardness and strength through most of the potential range. The only major anomaly was the GMA HAZ material which had an abnormally low strength at the lower potentials. From the standpoint of ductility, reference to Figures 38, 43, 44 and 45 indicates that, in general, the heat-affected zone material is more ductile than the weld metal material at the free corrosion potential. As the potential is increased in the cathodic direction, however, this order is reversed such that the weld metal material indicates greater ductility than the heat-affected zone material. The base metal material generally occupies an intermediate position between the two extremes at both the free corrosion and hydrogen generating potentials. It may therefore be concluded that the heat-affected zone material is more susceptible to HAC than the weld metal and that the base metal is of intermediate susceptibility.

As a possible explanation for the enhanced susceptibility of the HAZ to HAC, reference to the photomicrographs of Figures 16, 17 and 18 (Section 3.3.1) shows that the grain size of the HAZ is substantially larger than the grain size of either the weld metal or the base metal. If the failure mode were transgranular, then these larger grains would improve ductility as crack mobility would be impeded. If the failure mode were intergranular, then the larger grains would reduce ductility as crack mobility would be enhanced. These relationships suggest that the failure mode under free corrosion conditions was transgranular since the larger grained HAZ specimens were more ductile and that the failure mode under hydrogen generating HAC conditions was intergranular since the HAZ was less ductile. It should be pointed out that this is an hypothesis and that further photomicrographic evaluation would be required as supportive experimental evidence.

The heat-affected zone data generally displayed a greater degree of variance than either the weld metal data or the base metal data, as evidenced by parametric and photomicrographic evaluation. The parametric variation of the heat-affected zone data is most apparent in the faster strain rate test results (6.67×10^{-5} /sec), since the combined failure mode operative at this strain rate produced significant data scatter as discussed above. Reference to Figures 40, 41 and 42 reveals that the SAW HAZ data differ markedly from that of the weld metal or base metal while the GMA HAZ data differ to a somewhat lesser degree. Photomicrographic evidence is presented in Figure 60, where fracture surfaces of all five material types are shown for the faster strain rate at the hydrogen generating potential of -1250 mv SCE. The heat-affected zone fracture surfaces exhibit considerable shearing when compared to the relatively flat weld metal surfaces.

The variance in the heat-affected zone data is most probably attributable to the heterogeneity inherent to the HAZ region of the welded joint. Contrary to the relatively homogeneous unmelted base metal region and the totally melted weld metal region, the partially melted HAZ region is by definition a transition between the two. Its composition is thus somewhat uncertain, depending in large measure on the degree of weld process control. A second potential source of variance in heat-affected zone data stems from the machining of experimental specimens. In that the heat-affected zone is very narrow and difficult to identify, it is probable that at least some of the specimens were partially composed of weld metal and/or base metal. Although specimen preparation procedures attempted to minimize this effect through the use of the "K" weld geometry and through macroetching the ends of the specimen blanks (Sections 5.3.2 and 5.4.2), some sample heterogeneity was probably unavoidable.

From the process control standpoint, there was no substantial distinction between the data for the submerged arc weld specimens and the data for the gas metal arc weld specimens. Since the two welds were made from two sections of the same base plate with identical heat inputs and the same filler material under relatively rigorous laboratory control conditions, this result was expected. Therefore, all of the above results may be applied to the SAW and GMA processes interchangeably.

8. CONCLUSIONS

Based on the results of the experimental portion of the thesis research program, it may be concluded that:

(1) The lower bounds of K_{ISCC} for HSLA 80 base plate and weldments in a seawater environment are:

Base Metal: 83-89 ksi$\sqrt{in}$ (91-98 MPa$\sqrt{m}$)

Weld Metal: 95-98 ksi$\sqrt{in}$ (104-108 MPa$\sqrt{m}$)

HAZ Metal: 91-96 ksi$\sqrt{in}$ (100-106 MPa$\sqrt{m}$)

(2) There is no evidence of a separate critical stress intensity for hydrogen embrittlement (K_{IHEM}) based on WOL testing of HSLA 80 in a seawater environment.

(3) HSLA 80 is susceptible to hydrogen assisted cracking in a seawater environment.

(4) HSLA 80 is not susceptible to stress corrosion cracking in a seawater environment over the potential range of free corrosion (-435 mv SCE) to -1250 mv SCE.

(5) The hydrogen assisted cracking of HSLA 80 in a seawater environment occurs under conditions of continuous plastic deformation and triaxial stress in the presence of hydrogen.

(6) The failure mode for HSLA 80 in seawater under hydrogen assisted cracking conditions of (5) above is quasi-cleavage.

(7) Hydrogen assisted cracking of HSLA 80 in seawater is most severe at strain rates below 10^{-6} /sec.

(8) The heat-affected zone of HSLA 80 weldments exposed to seawater is more susceptible to hydrogen assisted cracking than the weld metal or the base metal regions.

(9) Weldments made by submerged arc welding and gas metal arc welding of HSLA 80 have essentially identical corrosion performance in a seawater environment.

(10) HSLA 80 is exceedingly tough and resistant to environmentally induced corrosion (i.e. SCC and HAC) for manufactured plate thicknesses up to and including 2 inches (50 mm). It is recommended for marine structural applications in seawater environments. However, some caution should be exercised in design applications where the potential exists for plastic deformation in the presence of hydrogen as these conditions have been found to promote HAC. This caveat is not unduly restrictive as ship structural calculations generally employ factors of safety incorporated to prevent reaching material yield strength.

9. FUTURE WORK

Further research in characterizing the corrosion performance of a given alloy in a given environment is only limited by time, money and practicality since the multidisciplined field of Corrosion Engineering can lead to a virtually endless series of experiments and theoretical postulations. Within the limited scope of this specific research project, however, several succeeding investigations are immediately suggested which directly extend the experimental conclusions:

(1) Full characterization of the susceptibility of the HSLA 80/seawater system to stress corrosion cracking requires a quantitative upper bound to K_{ISCC}. A Wedge-Opening Load test program with initial stress intensities in the range of 110 to 130 ksi/in (120 to 143 MPa/m) would provide this data.

(2) Although previous experiments with HY 130 [3] showed that flowing and stagnant seawater were essentially equivalent test environments, there is no absolute guarantee that this is the case with HSLA 80. A test program with flowing seawater would clarify this point for the HSLA 80/seawater system.

(3) No stress corrosion cracking was detected over the potential range investigated in the slow strain rate experiments conducted. Full characterization of this

susceptibilty would require a series of slow strain rate tests under conditions of anodic applied potentials.

(4) Strain rate effects were evaluated based on testing at two strain rates for all materials and selected tests at a lower strain rate. Full characterization of strain rate effects would require testing at the lower strain rate for all materials. This testing could be coupled with the anodic testing of (3) above to identify the bounds of HAC and SCC effects (if any).

(5) This research postulated a transgranular crack path under free corrosion potential conditions and an intergranular crack path under cathodic potential conditions based on heat-affected zone ductility. Further photomicrographic evaluation would be required to clarify this point.

(6) Charpy impact testing conducted to verify manufacturer's data in this research identified abnormally low toughness in the middle section of the two inch thick plate. A full series of Charpy and Dynamic Tear experiments would fully characterize through thickness toughness variations.

10. REFERENCES

1. Staehle, R. W., "Evaluation of Current State of the Stress Corrosion Cracking" *Proceedings of Conference on Fundamental Aspects of Stress Corrosion Cracking*, National Association of Corrosion Engineers, Houston, Texas, pp. 1-14 ,1969.

2. Brown, B. F., *Stress Corosion Cracking Control Measures*, National Bureau of Standards Monograph Number 156, U. S. Government Printing Office, Washington, D. C. ,1977.

3. Holsberg, P. W., Gudas, J. P. and Cox, T. B., "Stress Corrosion and Hydrogen Stress Cracking Behavior of HY-130 Steel Plate Weldments and Product Forms", DTNSRDC Report 76-0083, February, 1977.

4. Gudas, J. P., "FY 84 Program Plan; High Strength Low Alloy (HSLA) Steels for Naval Construction", Letter prepared by DTNSRDC Code 2814 for Naval Sea Systems Command, 1 October, 1983.

5. Latanision, R. M., Gastine, D. H., and Compeau, C. R., "Stress Corrosion Cracking and Hydrogen Embrittlement. Differences and Similarities", *Environment-Sensitive Fracture of Engineering Materials*, Z. A. Foroulis, ed., Proceedings of AIME Symposium, Chicago, Illinois, October 24-26, 1977.

6. Uhlig, H. H., "An Evaluation of Stress Corrosion Cracking Mechanisms", *Proceedings of Conference on Fundamental Aspects of Stress Corrosion Cracking*, National Association of Corrosion Engineers, Houston, Texas, 1969.

7. Bhatt, H. J. and Phelps, E. H., "Effect of Solution PH on the Mechanism of Stress Corrosion Cracking of a Martensitic Stainless Steel", *Corrosion*, Volume 17, pp. 430t-434t, 1961.

8. Brown, B. F., Fujii, C. T. and Dahlberg, E. P., "Methods for Studying the Solution Chemistry within Stress Corrosion Cracks", *Journal of the Electrochemical Society*, Volume 116, pp. 218-219, 1969.

9. Ateya, B. G. and Pickering, H. W., "On the Nature of Electrochemical Reactions at a Crack Tip during Hydrogen Charging of a Metal", *Journal of the Electrochemical Society*, Volume 122, pp. 1018-1025, 1975.

10. Brown, B. F. "Concept of the Occluded Corrosion Cell" *Corrosion*, Volume 26, pp. 249-250, 1970.

11. Scully, J. C., "Stress Corrosion Cracking; Introductory Remarks", *The Theory of Stress Corrosion Cracking in Alloys*, J. C. Scully, ed., NADCO, Brussels, Belgium, pp.1-17, 1971.

12. Fontana, M. G. and Greene, N. D., Corrosion Engineering, McGraw-Hill Book Company, New York, 1967.

13. Brown, B. F., "A Preface to the Problem of Stress Corrosion Cracking", Stress Corrosion Cracking of Metals-A State of the Art, ASTM STP 518, pp. 3-15, 1971.

14. Pourbaix, M., "Electrochemical Aspects of Stress Corrosion Cracking", The Theory of Stress Corrosion Cracking in Alloys, J. C. Scully, ed., NADCO, Brussels, Belgium, pp. 17-63, 1971.

15. Parkins, R. N., "Stress Corrosion Cracking of Mild Steels", Stress Corrosion Cracking and Embrittlement, W. D. Robertson, ed., Symposium of the Electrochemical Society, Boston, 1954, John Wiley and Sons, New York, 1956.

16. Graf, L., "Stress Corrosion Cracking in Homogeneous Alloys", Stress Corrosion Cracking and Embrittlement, W. D. Robertson, ed., Symposium of the Electrochemical Society, Boston, 1954, John Wiley and Sons, New York, pp. 48-60, 1956.

17. Parkins, R. N., "Stress Corrosion Cracking of Low Strength Ferritic Steels", The Theory of Stress Corrosion Cracking in Alloys, J. C. Scully, ed., NADCO, Brussels, Belgium, pp. 167-185, 1971.

18. Robertson, W. D. and Bakish, R., "Structural Factors Associated with Stress Corrosion Cracking of Homogeneous Alloys", Stress Corrosion Cracking and Embrittlement, W. D. Robertson, ed., John Wiley and Sons, New York, pp. 32-47, 1954.

19. Swann, P. R., "Morphological Aspects of Stress Corrosion Failure", The Theory of Stress Corrosion Cracking in Alloys, J. C. Scully, ed., NADCO, Brussels, Belgium, pp. 113-126, 1971.

20. Parkins, R. N., "Stress Corrosion Cracking of Low Carbon Steels" Proceedings of Conference on Fundamental Aspects of Stress Corrosion Cracking, National Association of Corrosion Engineers, Houston, Texas, pp. 361-373, 1969.

21. Wei, R. P., "Application of Fracture Mechanics to Stress Corrosion Cracking Studies", Proceedings of Conference on Fundamental Aspects of Stress Corrosion Cracking, National Association of Corrosion Engineers, Houston, Texas, pp. 104-112, 1969.

22. Weiss, V. and Yukawa, "Critical Appraisal of Fracture Mechanics", Fracture Toughness Testing and its Application, ASTM STP 381, pp. 1-29, 1964.

23. Broek, D., Elementary Engineering Fracture Mechanics, Third Revised Edition, Martinus Nijhoff Publishers, Boston, 1982.

24. ASTM E399-78a, "Standard Method of Test for Plane Strain Fracture Toughness of Metallic Materials", Annual Book of ASTM Standards, Part 10, 1978.

25. Mears, R. B., Brown, R. H. and Dix, E. H. Symposium on Stress Corrosion Corrosion Cracking of Metals, ASTM, AIME, Philadelphia, Pennsylvania, p. 323, 1945.

26. Harwood, J. J., "The Phenomena and Mechanisms of Stress Corrosion Cracking", Stress Corrosion Cracking and Embrittlement, W. D. Robertson, ed., Symposium of the Electrochemical Society, Boston, 1954, John Wiley and Sons, New York, pp.1-20, 1956.

27. Parkins, R. N., "The Stress Corrosion Cracking of Mild Steels in Nitrate Solution", Journal of the Iron and Steel Institute, Volume 172, pp. 149-162, 1952.

28. Hoar, T. P., "Stress Corrosion Cracking", Corrosion, Volume 19, pp. 331t-338t, 1963.

29. Pickering, H. W. and Swann, P. R., "Electron Metallography of Chemical Attack upon some Alloys Susceptible to Stress Corrosion Cracking", Corrosion, Volume 19, pp. 373t-389t, 1963.

30. Logan, H. L., "Film Rupture Mechanism of Stress Corrosion", Journal of Research of the National Bureau of Standards, Volume 48, pp. 99-105, 1952.

31. McEvily, A. J., and Bond, A. P., "On the Initiation and Growth of Stress Corrosion Cracks in Tarnished Brass", Journal of the Electrochemical Society, Volume 112, Number 2, pp. 131-137, 1965.

32. Forty, A. J., "The Initiation and Propogation of Cracks in the Stress Corrosion of Alpha-Brass and Similar Alloys", The Physical Metallurgy of Stress Corrosion Fracture, T. N. Rhodin, ed., Interscience Publishers, New York, 1959.

33. Petch, N. O. and Stables, P., "Delayed Fracture of Metals under Static Loads", Nature, Volume 169, pp. 842-843, 1952.

34. Vermilyea, D. A., "Reaction Films, Metal Dissolution, and Stress Corrosion Cracking", Proceedings of Conference on Fundamental Aspects of Stress Corrosion Cracking, National Association of Corrosion Engineers, Houston, Texas, pp.15-31, 1969.

35. McIntyre, D. R. and Dillon, C. P., Guidelines for Preventing Stress Corrosion Cracking in the Chemical Process Industries, MTI Publication 15, The Materials Technology Institute of the Chemical Process Industries, Incorporated, Columbus, Ohio, 1985.

36. Volkl, J. and Alefeld, G., "Diffusion of Hydrogen in Metals", Hydrogen in Metals I, Basic Properties, G. Alefeld, ed., Springer-Verlag, Berlin, Germany, 1978.

37. Uhlig, H. H., Corrosion and Corrosion Control: An Introduction to Corrosion Science and Engineering, second edition, John Wiley and Sons, New York, 1971.

38. Zapffe, C. and Sims, C., "Hydrogen Embrittlement, Internal Stress and Defects in Steel", Transactions of the American Institute of Metallurgical Engineers, Volume 145, pp. 225-261, 1945.

39. Beck, W., Bockris, J., McBreen, J., and Nanis, J., "Hydrogen Permeation in Metals as a Function of Stress, Temperature and Dissolved Hydrogen Concentration", Proceedings of the Royal Society of London, Volume 290, pp. 220-235, 1966.

40. Troiano, A. R., "The Role of Hydrogen and Other Interstitials in the Mechanical Behavior of Materials", Transactions of the American Society of Metals, Volume 52, Number 1, pp. 54-80, 1960.

41. Williams, D. P. and Nelson, H. G., "Embrittlement of 4130 Steel by Low Pressure Gaseous Hydrogen", Metallurgical Transactions, Volume 1, Number 1, pp. 63-68, 1970.

42. Beachem, C. D., "A New Model for Hydrogen-Assisted Cracking (Hydrogen Embrittlement)", Metallurgical Transactions, Volume 3, Number 2, pp. 437-451, 1972.

43. Clum, J. A., "The Role of Hydrogen Dislocation Generation Generation in Iron Alloys", Scripta Metallurgica, Volume 9, pp. 51-58, 1975.

44. Tien, J. K., Thompson, A. W., Bernstein, I. M. and Richards, R. J., "Hydrogen Transport by Dislocations", Metallurgical Transactions, Volume 7A, pp. 821-829, 1976.

45. Bernstein, I. M. and Thompson, A. W., editors, Hydrogen Effects in Metals, Proceedings of the Third International Conference on the Effect of Hydrogen on the Behavior of Materials, August 26-31, 1980, The Metallurgical Society AIME, Warrendale, Pa., 1981.

46. Masubuchi, K. Analysis of Welded Structures, Pergammon Press, New York, New York, 1980.

47. Coe, F. R., Welding Steels Without Hydrogen Cracking, The Welding Institute, Cambridge, England, 1973.

48. Savage, W. F., Nippes, E. F. and Husa, E. I., "Hydrogen Assisted Cracking in HY 130 Weldments", Welding Journal (Supplement), August, 1982.

49. Montemarano, T. W., Brenna, R. T., Caton, T. E., Davis, D. A., McCaw, R. L., Roberson, L. J., Scoonover, T. M. and Wong, R. J. "Results of the Evaluation of ASTM A710 Grade A Steel Under 'Certification of HSLA Steels for Surface Ship Construction Program'", DTNSRDC Report TM-28-84-17, January, 1984.

50. ASTM A710-79, "Low-Carbon Age-Hardening Nickel-Copper-Chromium-Molybdenum-Columbium and Nickel-Copper-Columbium Alloy Steels", Annual Book of ASTM Standards, Volume 01.04, 1979.

51. Montemarano, T. W., Sack, B. P., Gudas, J. P., Vassilaros, M. G. and Vanderveldt, H. H., "High Strength Low Alloy Steels in Naval Construction", paper presented at the Chesapeake Section of the Society of Naval Architects and Marine Engineers, September, 1984.

52. Bain, E. C. and Paxton, H. W., Alloying Elements in Steel, American Society for Metals, Metals Park, Ohio, 1961.

53. McGammon, H. E., editor, The Making, Shaping and Treating of Steel, U. S. Steel Corporation, 8th edition, 1964.

54. Porter, L. F. and Repas, P. E., "The Evolution of HSLA Steels", Journal of Metals, pp. 14-21, April, 1982.

55. Leslie, W. C., The Physical Metallurgy of Steels, Hemisphere Publishing Company, New York, New York, 1981.

56. Hansen, S. S., Vander Sande, J. B. and Cohen, M., "Niobium Carbonitride Precipitation and Austenitic Recrystalization in Hot-Rolled Microalloyed Steels", Metallurgical Transactions A, pp. 387-402, March, 1980.

57. Irvine, K. J., Pickering, F. B. and Gladman, T. "Grain-Refined C-Mn Steels", Journal of the Iron and Steel Institute, pp. 161-182, February, 1967.

58. Bittence, J. C., "Dual-Phase Steels Promise Higher Strength Plus Formability", Materials Engineering, pp. 39-42, May, 1978.

59. Smith, C. S. and Palma, E. W., "The Precipitation-Hardening of Copper Steels", Transactions AIME, Volume 105, pp. 133-166, 1933.

60. Creswick, W. E., "Commercial Development of a Rimmed Low Alloy Precipitation-Hardening High-Strength Steel", Iron and Steel Institute Publication 104, The Iron and Steel Institute, pp. 86-92, 1967.

61. Hurley, J. L. and Shelton, C. H., "Age-Hardenable Nickel-Copper Steels", Metals Engineering Quarterly, Volume 6 Number 2, American Society for Metals, pp. 25-31, May, 1966.

62. Kelly, R. E., "Optimization of Mechanical Properties of 'IN-787' Nickel-Copper-Columbium Age Hardenable Alloy", Master's Thesis, University of Texas at El Paso, August 28, 1979.

63. Hydrean, P. P., Chard, J. E. and Shelton, C. H., "IN-787: An Age Hardenable Steel for Line Pipe and General Structural Use", International Nickel Company Technical Report 775-T-OP, April 5, 1972.

64. Money, K. L. and Anderson, D. B., "IN-787, A Low Alloy Steel for Offshore Platforms and Ship Hull Plate Applications" Paper OTC 2375 presented at Seventh Annual Offshore Technology Conference, Houston, Texas, May, 1975.

65. Greene, N. D., Experimental Electrode Kinetics, Rensselaer Polytechnical Institute, Troy, New York.

66. ASTM A715-84a, "Steel Sheet and Strip, High-Strength Low Alloy Hot-Rolled, with Improved Formability", Annual Book of ASTM Standards, Volume 01.04, 1984.

67. Commander, David Taylor Naval Ship Research and Development Center letter serial 2814 dated 30 January, 1984.

68. Gibbs and Cox report 19441-6 "Potential Applications of High Strength Low Alloy Steels to Naval Surface Combatants", April, 1983.

69. Hicho, G. E., Smith, L. C., Singhal, S., and Fields, R. J., "Effects of Variations in Heat Treatment on the Mechanical Properties and Microstructure of ASTM A710 Grade A Class 3 Steel", National Bureau of Standards Report NBSIR 83-2685, May, 1983.

70. McCaw, R. L. and Wong, R. J., "Welding of HSLA-80 Steel-Certification of HSLA Steels for Surface Ship Construction" David Taylor Naval Ship Research and Development Center Report SME-85/32, June, 1985.

71. Military Standard 1688(SH), "Fabrication, Welding and Inspection of HY-80/100 Submarine Applications", February, 1981.

72. Caton, T. E., "Status of Corrosion Testing of High Strength Low Alloy Steels: 1984 Review", David Taylor Naval Research and Development Center Report SME-84-99, April, 1985.

73. Brick, R. M., Pense, A. W. and Gordon, R. B., Structure and Properties of Engineering Materials, McGraw-Hill Book Company, New York, New York, 1977.

74. McClintock, F. A. and Argon, A. S., Mechanical Behavior of Materials, Addison-Wesley Publishing Company, Reading, Massachusetts, 1966.

75. Meyers, M. A., and Chawla, K. K., Mechanical Metallurgy: Principles and Applications, Prentice-Hall, Englewood Cliffs, New Jersey, 1984.

76. Caton, T. E. and Tipton, D. G., "Preliminary Results on SCC Test Methodology Study", David Taylor Naval Ship Research and Development Center Report SME-83-106, April, 1984.

77. Boyd, W. K. and Fink, F. W., Corrosion of Metals in Marine Environments, Metals and Ceramics Information Center Publication MCIC-78-37, Battelle Laboratories, Columbus, Ohio, 1978.

78. Course Notes from "Corrosion", Course Number 3.54 at the Massachusetts Institute of Technology, Professor R. M. Latanision, Spring, 1985.

79. Holsberg, P. and Blackburn, J., Private meeting held 24 August, 1984 at David Taylor Naval Ship Research and Development Center, Annapolis, Maryland.

80. Kihara, H., Suzuki, H. and Tamura, H., "Researches on Weldable High-Strength Steels", The Society of Naval Architects of Japan, Sixtieth Anniversary Series, Volume 1, 1957.

81. Phillips, A. L., editor, Current Welding Processes, American Welding Society, United Engineering Center, New York, New York, 1964.

82. Novak, S. R. and Rolfe, S. T. "Modified WOL Specimen for KISCC Environmental Testing", Journal of Materials, JMLSA, Volume 4 Number 3, pp. 701-728, September, 1969.

83. Manjoine, M. J., "Plane Strain Crack Toughness Testing of High Strength Metallic Materials", ASTM STP 410, American Society of Testing and Materials, Philadelphia, pp. 66-70, December, 1967.

84. Brown, B. F. and Beachem, C. D., " A Study of the Stress Factor in Corrosion Cracking by Use of the Precracked Cantilever Beam Specimen", Corrosion Science, Volume 5, pp. 745-750, 1965.

85. Smith, J. H. and Rolfe, S. T., "Effect of Notch Orientation on KISCC of Weld Metal" United States Steel Research Report Number 39.018-016(S), 1967.

86. Parkins, R. N., "Development of Strain-Rate Testing and Its Implications", Stress Corrosion Cracking-The Slow Strain Rate Technique, ASTM STP 665, G. M. Ugiansky and J. H. Payer, editors, American Society of Testing and Materials, pp. 5-25, 1979.

87. Kim, C. D. and Wilde, B. E., "A Review of Constant Strain Rate Stress Corrosion Cracking Test", Stress Corrosion Cracking-The Slow Strain Rate Technique, ASTM STP 665, G. M. Ugiansky and J. H. Payer, editors, American Society of Testing and Materials, pp. 97-112, 1979.

88. Diegle, R. B. and Boyd, W. K., "The Role of Film Rupture During Slow Strain Rate Stress Corrosion Cracking Testing", Stress Corrosion Cracking-The Slow Strain Rate Technique, ASTM STP 665, G. M. Ugiansky and J. H. Payer, editors, American Society of Testing and Materials, pp. 26-46, 1979.

89. Hoar, T. P. and Hines, J. G. "The Corrosion Potential of Stainless Steels during Stress Corrosion", Journal of the Iron and Steel Institute, Volume 177, p.248, 1954.

90. Payer, J. H., Berry, W. E. and Boyd, W. K., "Evaluation of Slow Strain Rate Stress Corrosion Test Results", Stress Corrosion Cracking-The Slow Strain Rate Technique, ASTM STP 665, G. M. Ugiansky and J. H. Payer, editors, American Society of Testing and Materials, pp. 61-77, 1979.

91. Dieter, G. E., Mechanical Metallurgy, second edition, McGraw Hill Book Company, 1976.

92. Dahlberg, E. P., "Techniques for Cleaning Service Failures in Preparation for Scanning Electron Microscope and Microprobe Analysis", Scanning Electron Microscope (Part IV), Proceedings of the Workshop on Failure Analysis and the SEM, IIT Research Institute, Chicago, Illinois, pp. 911-915, 1974.